APPLICATIONS OF LIGHT FOR BIOMATERIALS AND SAFETY

A Dissertation

by

DAWSON THOMAS NODURFT

Submitted to the Office of Graduate and Professional Studies of
Texas A&M University
in partial fulfillment of the requirements for the degree of

DOCTOR OF PHILOSOPHY

Chair of Committee,	Vladislav Yakovlev
Committee Members,	Alexei Sokolov
	George Welch
	Alexey Belyanin
	Pao Tai Lin
Head of Department,	Grigory Rogachev

May 2019

Major Subject: Physics

ABSTRACT

The interaction of light with biological media represents an increasingly important area of research. Recent expansion of ultrafast laser sources in the mid-infrared (MIR) regime is driving research in previously unexplored areas. In particular, the applications of these systems to biological materials is significant due to biological materials response to MIR wavelengths. The first two works presented here are motivated by gaps in the American National Standard for Safe Use of Lasers (ANSI) Z136.1 for eye safety. While we are ultimately interested in the nonlinear effects of MIR laser sources and the potential for retinal damage, we began by studying nonlinear behavior in Zinc Selenide (ZnSe) and air. The nonlinear processes examined were that of harmonic and continuum generation. The filament that was generated by the laser pulse in atmospheric air produced enough visible light at several wavelengths that were determined to be hazardous to the retina. Further work is required by the study in ZnSe to determine if maximum permissible exposure limits for retinal tissue was exceeded, despite significant visible light generation having been observed in spectral analysis.

Laser light is not only a threat to safety, but a tool for use in diagnosing and understanding complicated biological structures. Raman spectroscopy allows for precise chemical and molecular analysis. The information Raman spectroscopy provides can identify the composition of unknown materials along with quantification of molecular concentration. Analysis of a commercial Raman spectrometer provided information about the most effective operation parameters for signal-to-noise enhancement.

Thereafter, the spectrometer was used in determining the effectiveness of a microfluidic device as a cultivation tool for microalgae produced lipids. The results showed that Raman spectroscopy worked as effectively at measuring lipid production for time-course analysis as conventional methods without causing the damage to the algae cell typical of those conventional methods. Finally, a random Raman laser was investigated as a tool for imaging phenomena with lifetimes on the order of nanoseconds. The work determined the random Raman laser to be a more effective imaging tool when compared to two other conventional strobe methods.

DEDICATION

To my wife and family, whose love and support throughout the years will forever humble and amaze me.

ACKNOWLEDGEMENTS

I would like to begin by thanking my committee chair and graduate advisor, Dr. Vladislav Yakovlev, for agreeing to support me in my graduate student career. Thank you for your patience with me and willingness to see my degree through to the end as a progressed through graduate school. Furthermore, I would like to thank the rest of my dissertation committee members, Dr. Alexei Sokolov, Dr. Alexei Belyanin, Dr. George Welch, and Dr. Pao Tai Lin for agreeing to be part of my committee and seeing me through the stressful process. I want to thank Dr. Sokolov in particular for his invitations to his office and willingness to assist me when I needed it most. I would also like to state my gratitude to Dr. Adam Boretsky and Gary Noojin of Engility Corporation at the Air Force Research Lab at Ft. Sam Houston. Their knowledge and expertise were invaluable in completing a significant portion of the work contained within this dissertation. I would also like to thank Dr. Tatiana Erukhimova for all the support and mentorship she has given me over the years. Working with her on the many outreach programs she runs has been one of the singular greatest joys and honors of my time at graduate school.

Thank you to all of my friends, graduated or still working away at Texas A&M University, for all of your help over the years. I would never made it through without all of your support from day one. The friends I would like to make special mention of are Charles Ballmann, Joe Becker, Sean Blakley, Ellie Broiles, Han Cai, Michael Cone, Frank Echeverria, Jacob Gayles, Brett Hokr, James Gerity, Heshani Jayatissa, Christopher Marble, John Mason, Ryan Mueller, Matthew Morrison, Tyler Morrison,

Sean O'Connor, Jonathan Perry, Junchen Rong, Matthew Springer, Jonathan Thompson, Andrew Traverso, Sriteja Upadhyayula, Sean Wu, Sean Yeager, and Sasha Zhdanova. I would like to especially thank Andrew Traverso for mentoring me in the lab, I learned a lot from his wealth of knowledge and appreciate his never-ending willingness to lend a hand.

I would never have made it through graduate school without the constant support of my family. To my Mom, thank you for always pushing me to do my best and providing a friendly ear when I needed to vent off steam. More than that, you were a constant guiding hand in my youth and helped me find the way when I seemed lost. Mom, you constantly inspire me with your diligence and hard work. To my Dad, thank you for teaching me to stand my ground and speak up for what I believe. Thank you for always offering words of wisdom when I needed perspective. To Grandma, I will forever be grateful for your kindness in offering Grandpa's ring to me. I will treasure it forever, and it is great to have something of him I can carry with me every day.

Justin, Ian and Trevor thank you for being the best brothers and friends. I look forward to getting back into the world and spending some time catching up with you all. Trevor, I really enjoyed spending that time with you streaming online and just getting to goof off and chat. I hope to do so again soon. Ian, thank you for being the person I can count on for a good laugh when I need it. You have probably one of the greatest dry wits I've ever had the pleasure to observe. Justin, reconnecting with you the past few years has been one of the best parts of my time in graduate school. You continually go out of

your way to help me by making my life a little brighter with your thoughtful gifts and actions. Most importantly thank you for gifting me your friendship, nothing means more.

To my new family, the Ellisors, thank you all for welcoming me in with open arms. It has been a distinct honor and privilege to get to know each of you. Mr. Ellisor, thanks for making me feel not so alone during the numerous times I have inevitably put my foot in my mouth. I love how you are always ready for a good joke or fun way to goof around. Julie, you always amaze me with how open you are with your home and your heart. You made me feel like part of the family well before I ever was. To Meggie, the sister I never had, thank you for always running with my silly gags. I never get bored of the shenanigans we get into. Ryan, if there is ever anyone I can count on to be down for whatever game or plan I have concocted, it is you. You are the fourth brother I now have, and I wouldn't want it to be anyone else. To the extended family, in particular Papaw, Mamaw, and Granny. The welcoming love, laughter, and support you all have provided is proved invaluable.

Finally, I want to thank my loving and amazing wife, Hayley. Words cannot express how much I am indebted to you for all of the help you showered on me during this stressful time. You have been my rock, best friend, and supporter all throughout this journey.

CONTRIBUTORS AND FUNDING SOURCES

Contributors

This work was supported by a dissertation committee consisting of Professors Vladislav Yakovlev [advisor], Alexei Sokolov, Alexey Belyanin, and George Welch of the Department of Physics and Astronomy and Professor Pao Tai Lin of the Department of Electrical Engineering.

The data collected and analyzed for Chapter II was completed independently by the student at the Air Force Research Lab at Ft. Sam Houston. Discussions and collaboration were provided by Sean O'Connor, Christopher Marble and Vladislav Yakovlev of the Department of Physics as well as Gary Noojin, Joseph Clary, and Adam Boretsky from the Engility Corporation at AFRL at Ft. Sam Houston.

The data collected and analyzed for Chapter III was done in collaboration with Sean O'Connor, Christopher Marble, and Vladislav Yakovlev at AFRL, Ft. Sam Houston. Discussions and technical assistance were provided by Gary Noojin and Adam Boretsky from Engility Corporation along with Andrew Wharmby of the 711th Human Perfromance Wing at AFRL, Ft. Sam Houston.

All work for Chapter IV was completed independently by the student in collaboration with Vladislav Yakovlev at Texas A&M University.

The student collected the Raman spectral data for Chapter V in collaboration with Sergio Waqued of the Department of Biomedical Engineering. Analysis of the Raman data and other fluorescence data taken were performed by Sergio Waqued. The

published document was completed by Hyun Kim of the Department of Electrical and Computer Engineering and released in March of 2017 from the journal Analyst by the Royal Society of Chemistry. The completed work was assisted by Timothy Devarenne of the Department of Biochemistry and Biophysics, Vladislav Yakovlev of the Department of Physis and Astronomy, and Arum Han of the Department of Electrical and Computer Engineering.

The student contributed to the work in Chapter VI by assisting Brett Hokr in the collection of data and images of laser induced breakdown of water from by the random Raman lasing, fluorescence, and laser pulse strobe mechanisms at the AFRL at Ft. Sam Houston. The work was published in March of 2017 in Nature Scientific Reports. Brett Hokr completed analysis of the data and wrote the published article. Other significant contributions were provided by Jonathan Thompson, Marlan Scully, and Vladislav Yakovlev of the Department of Physics and Astronomy; Joel Bixler, Robert Thomas, and Benjamin Rockwell of the 711th Human Perfomance Wing at AFRL, Ft. Sam Houston; Brandon Redding and Hui Cao of Yale University; and Gary Noojin from Engility Corporation at AFRL, Ft. Sam Houston.

All other work for the dissertation was completed by the student.

Funding Sources

This research was in part supported by the National Science Foundation (NSF) (DBI-1455671, DBI-1532188, ECCS-1509268, CMMI-1826078), the Air Force Office of Scientific Research (AFOSR) (FA9550-15-1-0517, FA9550-18-1-0141), the Defense

Advanced Research Projects Agency (DARPA) (FA8650-13-D-6368/0006), the Office of Naval Research (ONR) (N00014-16-1-2578), the National Institutes of Health (NIH) (1R01GM127696-01).

TABLE OF CONTENTS

Page

ABSTRACT ii

DEDICATION iv

ACKNOWLEDGEMENTS v

CONTRIBUTORS AND FUNDING SOURCES viii

TABLE OF CONTENTS xi

LIST OF FIGURES xiii

LIST OF TABLES xix

CHAPTER I INTRODUCTION 1

1.1 Motivation 1
1.2 ANSI Standards 2
1.3 Harmonic and Supercontinuum Generation 4
1.4 Filamentation 11
1.5 Raman Spectroscopy 19

CHAPTER II SUPERCONTINUUM GENERATION IN ZINC SELENIDE FROM MIR LASER PULSES 22

2.1 Background and Motivation 22
2.2 Materials and Methods 23
2.3 Results and Discussion 25
2.4 Conclusions 28

CHAPTER III FILAMENTATION IN ATMOSPHERIC AIR FROM TUNABLE NIR PULSES 29

3.1 Background and Motivation 29
3.2 Materials and Methods 30
3.3 Results and Discussion 33
3.4 Conclusions and Further Work 39

CHAPTER IV NSR RAMAN SPECTROSCOPY 40

4.1 Background and Motivation 40
4.1.1 Introduction to the Allan Variance 42
4.2 Materials and Methods 44
4.3 Results and Discussion 45
4.3.1 NSR Calculation 45
4.3.2 Allan Variance Calculation 49
4.4 Conclusion 60

CHAPTER V RAMAN SPECTROSCOPY COMPATIBLE PDMS DROPLET MICROFLUIDIC CULTURE AND ANALYSIS PLATFORM TOWARDS ON-CHIP LIPIDOMICS 61

5.1 Background and Motivation 61
5.2 Materials and Methods 64
5.2.1 Raman Spectroscopy 64
5.2.2 Microfluidic Device 66
5.2.3 Microalgae Preparation 68
5.2.4 Tracking Lipid Production 68
5.3 Results and Discussion 69
5.3.1 Background Reduction of Raman Spectra 69
5.3.2 Droplet Microfluidics vs. Free-Floating Microfluidics 75
5.3.3 Lipid Production Over Time In 8 Different Culture Conditions 78
5.4 Conclusion 80

CHAPTER VI ENABLING TIME RESOLVED MICROSCOPY WITH RANDOM RAMAN LASING 82

6.1 Background and Motivation 82
6.2 Materials and Methods 86
6.2.1 Characterization of Speckle 86
6.2.2 Imaging of Laser Induced Breakdown of Water 88
6.3 Results and Discussion 89
6.3.1 Analysis of Speckle Contrast 89
6.3.2 Analysis and Comparison of Imaging of Laser Induced Breakdown of Water 90
6.4 Conclusion 96

CHAPTER VII CONCLUSION 97

REFERENCES 98

LIST OF FIGURES

Page

Figure I.1: a) Second harmonic generation and b) Nth harmonic generation. Second harmonic generation occurs when two photons of the same frequency ν collectively excite the molecule into a virtual state. The resulting drop back to the ground state emits a photon with twice the energy and therefore frequency of one of the incident photons. The Nth harmonic is an extrapolation of the second harmonic case. 5

Figure I.2: Time dependent intensity of a Gaussian laser pulse. The pulse has a maximum amplitude of $\boldsymbol{I0}$ at time zero. As time increases, the pulse propagates into and through the medium. Therefore, the side of the pulse that first interacts with the medium is at times $\boldsymbol{t < 0}$, also known as the leading edge. 9

Figure I.3: The instantaneous frequency demonstrates how the pulse is spectrally broadened as it passes through the medium. Before the pulse arrives at the medium, it has a frequency of $\boldsymbol{\omega 0}$. As the leading edge interacts with the medium, the change in the nonlinear phase shift induces a red shift in the frequency. The center of the pulse, with the highest intensity, experiences no shift. The trailing edge has a blue shift in its frequency. 11

Figure I.4: Filamentation. The black dotted outer lines demonstrates the standard diffraction limit of a focused laser beam. The red inner lines demonstrate a filament beating the diffraction limit while balancing the effects of self-focusing and plasma defocusing. Adapted from Couairon, et al. "Femtosecond filamentation in transparent media" [28]. 12

Figure I.5: Self-focusing. A collimated laser beam with a beam waist radius of $\boldsymbol{w0}$ is incident upon a nonlinear medium. The intensity profile of the beam is such that the on-axis intensity is larger than that of the edges. The result is a spatially varying refractive index, where the refractive index decreases until it becomes just the linear refractive index as one moves away from the beam axis. The self-focusing distance ($\boldsymbol{zsf}$) and angle ($\boldsymbol{\theta sf}$), where $\boldsymbol{zsf}$ can be found by application of Fermat's principle. Adapted from Robert Boyd's "Nonlinear Optics" [24]. 13

Figure I.6: Optical wavefront deformation by a lens. The collimated laser beam has a flat wavefront before interacting with the positive lens. After passing through the lens, the wavefront becomes curved and converges on the focal point. 15

Figure I.7: Self-steepening. a) A Gaussian laser pulse begins propagating through a nonlinear medium. b) As the pulse interacts with the medium, the more intense portions of the pulse are slowed by interaction with a higher refractive index. The trailing edge of the pulse then begins to accrue a steeper slope as the peak of the pulse is slowed and the trailing edge catches up, which is known as self-steepening. Adapted from Robert Boyd's "Nonlinear Optics" [24]. 18

Figure I.8: a) Rayleigh Scattering, b) Stokes Raman Scattering, and c) Anti-Stokes Raman Scattering. Note about "vibrational levels": figures' vibrational states are just to represent the multiple states of a molecule, distance of separation in figure is not representative of real vibrational states. 20

Figure II.1: Experimental setup to observe supercontinuum generation in ZnSe 25

Figure II.2: Supercontinuum generation in ZnSe from an input beam wavelength of a) 4 μm, b) 10 μm, c) 12 μm, and d) 20 μm. The black spectra were collected from an Ocean Optics visible spectrometer and the red from an Ocean Optics NIR spectrometer. The spectra all have a common feature of a dip in the continuum from ~600 to 1000 nm which are due to the transmittance/reflectance of the cold mirror. The small "peaks" in this region are due to the variations in the reflectance curve of the cold mirror. Of note are the harmonic peaks generated by the 10 and 12 μm beams at 475 and 478 nm respectively. Those correspond to the 21^{st} and 25^{th} harmonic, respectively, of the incident 10 and 12 μm beams. 26

Figure III.1: a) Experimental setup to observe harmonic and supercontinuum generation. b) Setup for visible light collection and power measurement after supercontinuum generation. 32

Figure III.2: Images of supercontinuum generation from filamentation imaged on a blank sheet for source wavelength of a) 1300 nm, b) 1400 nm, c) 1500 nm, and d) 1600 nm idler. 34

Figure III.3: Four representative spectra at a) 1200 nm, b) 1300 nm, c) 1400 nm, and d) 1700 nm. The visual spectra are shown in black and red while the IR is in blue. The left axis (black) corresponds to visual spectra and the right axis (blue) to NIR spectra. Black and blue data represents spectra take from the center and red from the fringe. The visual fringe and IR center demonstrate spectral broadening and continuum generation. The visual center showcases both continuum generation and harmonic generation. 35

Figure III.4: Pulse energies of visible light (sub 1000 nm) from filament after filtering out infrared as collected by a power meter. The energies measured are collected using the maximum input pulse energies recorded in Table 3.1.

The MPE exposure thresholds for visible light on the retina were surpassed by both lenses for 1300 and 1400 nm light. For 1500 and 1600 nm light, the MPE threshold was surpassed for one lens but not both. 38

Figure IV.1: a) Raman spectrum of mineral oil collected a) with a Raman microscope (LabRAM, Horiba, Inc.) and b) with ASEQ spectrometer (data scaled by factor of 10 for viewing purposes). Both spectra were collected with 10s integration times. 46

Figure IV.2: Noise-to-Signal Ratios for both the Raman microscope (LabRAM, Horiba, Inc.) and the home-build Raman microscope based on the ASEQ spectrometer. a) The peak intensity of the 2873 cm^{-1} Raman line collected with the home-built Raman spectrometer. b), c), and d) The peak intensities of the 1303, 1445, and 2873 cm^{-1} Raman lines collected with the Raman microscope (Labram, Horiba, Inc.).....47

Figure IV.3: Allan variance for the 2873 cm^{-1} Raman peak with the ASEQ spectrometer. An initial minimum in the Allan variance is seen at ~2400-s. The minima observed after 10000-s are found to be caused by fluctuations in the temperature of the spectrometer. 49

Figure IV.4: Allan variance of peak-to-peak noise for the ASEQ spectrometer. The low frequency fluctuations past 10000-s imply the cause is thermal fluctuations in the spectrometer. The peak-to-peak noise is primarily dependent upon the dark current of the spectrometer and therefore the temperature of the spectrometer. 50

Figure IV.5: Allan Variance for the a) 2873 cm^{-1}, b) 1445 cm^{-1}, and c) 1303 cm^{-1} Raman peaks with the Horiba spectrometer. An Allan variance minimum is seen at ~900-s. A low frequency oscillation occurs throughout the Allan variance curve. Inspection determined the cause to be shifts in the power output of the 532 nm laser. The decrease in the Allan variance past 10000-s is again determined to be caused by temperature shifts in the spectrometer. ...52

Figure IV.6: Allan variance of peak-to-peak noise for the Horiba spectrometer. An Allan variance minima is reached around 1600-s. The low frequency oscillation is due to temperature changes in the CCD. 54

Figure IV.7: 2873 cm^{-1} peak values for Horiba spectrometer. Each data point is an individual 10-s integration time spectra and the time indicates how long after the start of the experiment the data was collected. The data indicates the laser was mode hoping, thereby causing large variations in the power output of the beam. The power output variation caused a variation in the spectral peak intensity.....56

Figure IV.8: 2873 cm^{-1} peak values for ASEQ spectrometer. Each data point is an individual 10-s integration time spectra and the time indicates how long after the start of the experiment the data was collected. When compared to the peak values of the Horiba spectrometer, we find that the laser was far more stable. 57

Figure IV.9: Running average of peak-to-peak noise for the ASEQ spectrometer. By inspection, we can determine that after ~2000-s, additional averaging was not decreasing the peak-to-peak noise and therefore not decreasing NSR. 59

Figure V.1: PDMS microfluidic droplet device. The cell solution enters a T-junction with the carrier oil that sections the cell solution into individual droplets. The droplets are stored in different cell chambers. Each chamber's environmental conditions can be uniquely set to observe changes in lipid production as a result. The cell cultures in the device are then inspected by a confocal Raman microscope. 66

Figure V.2: PDMS background reduction by device orientation. a) Comparison of device in upright and inverted orientations. b) Comparison of Raman shift of *B. braunii* from upright (black) and inverted (red) orientation. c) Rescaled view of Raman shift in inverted orientation in b) showing significant reduction in PDMS Raman peak (black arrows) background while showing lipid peaks (red arrows). 70

Figure V.3: Comparison PDMS background in Raman spectra of *B. braunii* lipids with 4.6 AU confocal pinhole to 0.56 AU confocal pinhole. Lipid peaks are indicated with red arrows, and PDMS peaks with black arrows. 72

Figure V.4: Raman spectra of *B. braunii* lipids from 0.56 AU confocal pinhole (black), on a fused silica substrate (red), and difference between the two (blue). 73

Figure V.5: a) Diagram comparing droplet encapsulated cells vs. free-floating *C. reinhardtii* cells. b) Microscopic images of droplet generation, culture chamber filled with droplets, and enlarged view of cells within droplets. 75

Figure V.6: Spectra of FC-40 carrier oil with (black) and without FluoroSurfactant (red). Two are compared to Raman spectra of *C. reinhardtii* cell. No peaks were observed in the carrier oil Raman spectra that would interfere with the critical lipid peaks. 76

Figure V.7: Comparison of spectra of *C. reinhardtii* cells in droplet and free-floating culture media, both with and without nitrogen deprivation. The nitrogen rich concentrations in both free-floating and encapsulated cells were found to have no lipid production. The similarities for both droplet encapsulated

cells and free-floating cells in a nitrogen depleted environment indicates that the use of microfluidic devices will not hinder its use for the application of Raman spectroscopy. 77

Figure V.8: Time-course Raman spectral analysis of lipid production of *C. reinhardtii* cells in 8 different nitrogen concentrations. As expected, those cells that were cultured in nitrogen depleted chambers produced more lipids than those in a nitrogen rich environment. 78

Figure V.9: Correlation between average Raman peak intensity at 1657 cm^{-1} and average Nile red fluorescent intensity per unit cell volume. The high correlation indicates that Raman spectroscopy is a valid alternative to traditional methods like fluorescence staining. The Raman method is not a single time measurement like fluorescence staining can be, allowing for time-course tracking of the same cell's lipid production. 79

Figure VI.1: Conceptual drawing of random Raman lasing emission (yellow) being stimulated by incident pump laser (green). 84

Figure VI.2: Comparison of brightness of different light sources for imaging. Useful peak power is the peak power achieved in a specified bandwidth at the optimum wavelength for that light source. It is the measure of how much light is absorbed by the sample. This is then multiplied by quantum efficiency of the process to obtain the peak power observed by the camera. 85

Figure VI.3: Raman emission spectrum of random Raman laser for $BaSO_4$. The 985 cm^{-1} shift from 532 nm pump placing the wavelength of the emission at 562 nm with a 0.25 nm spectral width. 86

Figure VI.4: Experimental setup for random Raman laser imaging. 88

Figure VI.5: Comparison of speckle contrast images from HeNe laser, random Raman laser, and halogen light sources. The calculated speckle contrast C indicates that while the random Raman laser has some spatial coherence, it is very low, especially when compared to that of a coherent HeNe laser. 89

Figure VI.6: Images of laser induced breakdown of water at different delay stage times using random Raman laser. As the time passes, the shockwave is observed to propagate through the water. Very fine details of the breakdown can be observed. 91

Figure VI.7: Images of laser induced breakdown of water at different delay stage times using fluorescence from a Rhodamine 590 dye. While the fluorescence provides a strong contrast with the breakdown, the lifetime of the fluorescence decay is on the order of the lifetime of the shockwave (ie.

nanoseconds). The temporal resolution is degraded and shockwave features cannot be made out. 92

Figure VI.8: Images of laser induced breakdown of water at different delay stage times using the 50 ps 532 nm laser pulse. While providing more detail than the fluorescence strobe, the coherence of the beam leads to a large amount of speckle preventing imaging of the small details within the shockwave.....93

Figure VI.9: Sobel filtered images of random Raman laser, 532 nm laser, and fluorescence images at 2 ns delay stage. The Sobel filter is an image processing tool that detects the edge imaged objects by recognizing where contrast between two parts of an image is high. The Sobel filter enhances the difference between different strobe methods, further proving that random Raman lasing is a strong tool for image capture. 94

Figure VI.10: Fast Fourier Transform applied to each imaging strobe at 2 ns delay stage. The FFT of the three images gives important information about each strobe method by determining the number of spatial frequencies in each image. The laser image has a bright and broad background spectral frequency due to speckle. The low temporal resolution for the fluorescence strobe leads to low spatial frequencies. The FFT random Raman lasing balances the other two with a large number of spatial frequencies, and better temporal coherence implying less speckle. 95

LIST OF TABLES

Page

Table II.1: Summary of Supercontinuum and Harmonic Spectral Data for MIR Pump Laser in ZnSe 28

Table III.1: Summary of Supercontinuum and Harmonic Spectral Data for NIR Pump Laser in Atmospheric Air 36

CHAPTER I

INTRODUCTION

1.1 Motivation

Since its invention, the laser has become a tool widely used throughout society [1]. Its many applications from precision measurement to medical technology mean that more people come in contact with these systems each year. As such, it is important to understand how the light generated from laser systems interact with the biological materials with which they come into contact. Certain critical parts of the eye are very susceptible to damage induced by a laser. Parts of the eye like the cornea and lens absorb a significant portion of light outside of the visible spectrum and even if damaged will not prevent sight. Light that passes through these outer eye layers will generally reach the retina. Should the retina be damaged, loss of eyesight can occur. This necessitates having strongly set and defined maximum permissible exposure (MPE) limits based on laser wavelength and time duration.

Lasers have significant applications to the advancement of biological and medical technologies. Raman scattering is an extremely versatile tool due to the molecular chemical information it provides. The chemical information acts essentially as a “fingerprint” for the material being analyzed. Utilizing this tool for analysis of materials over time can impact how we produce goods. Imaging, while possibly one of the oldest uses of light, is still one of the most important. Many medical technologies from magnetic resonance imaging (MRI) to ultrasound, allow doctors to view human

anatomy or observe physiology. Discovering new ways to image within the body in non-invasive manners would be extreme breakthroughs.

1.2 ANSI Standards

The current ANSI eye safety standards (Z136.1) currently do not set MPE limits that account for nonlinear processes that could alter laser frequency in mid-infrared (MIR) wavelengths. The standard for retinal damage is currently based on pulse durations ranging from second to nanosecond. The nonlinear effects of those pulse durations are negligible, however picosecond to femtosecond pulses can have drastic nonlinear responses. Therefore, the laser eye protection (LEP) equipment required for safe operation may not be suitable given current standards when operating in these MIR ultrafast pulse regimes. The cornea, aqueous, and vitreous humors of the eye absorb MIR light to such a significant degree that ANSI allows for high MPE limits. The damage is therefore limited to the lens and cornea in a linear optics system. When dealing with nonlinear phenomena such as harmonic and supercontinuum generation, the visible and near-infrared (NIR) wavelengths become accessible with MIR laser pulses. The lack of absorption in the eye before the retina for wavelengths under 1.2 μm allows the visible and NIR light generated from the original MIR pulse to pass to the retina. The retina has lower MPE limits in the visible and NIR, thus the generated light might be damaging. [2]

A few of the characteristics of electromagnetic radiation that play a significant role in the interaction with a media are the pulse energy, pulse width, and the temporal shape of the pulse, which in turn are related to the peak power of the pulse. When

observing a light pulse, the pulse energy can be found by simply integrating the curve of the optical power of an electromagnetic radiation pulse as a function of time. The peak power of the pulse is found from the place of maximum amplitude on the optical power curve. Imagine that pulse energy remained constant, but the duration of the pulse was decreased. The pulse energy remaining constant requires that the area under the optical power curve remains a constant and thereby forces the maximum amplitude to significantly increase. Higher peak power is obtained simply by changing pulse duration without changing the pulse energy. The relationship is given by:

$$Peak\ Power = \frac{Pulse\ Energy}{Pulse\ Duration} \quad \text{(Eq. 1.1)}$$

The different components of the eye have different thresholds for damage. Damage thresholds are stated as the amount of radiant exposure with units of Joules per square centimeter. The radiant exposure thresholds are typically for wavelengths ranging from the ultraviolet to the far-infrared. The thresholds take the duration of exposure to the radiation in to account as well. The MPE threshold as determined by ANSI is the maximum allowed radiant exposure of electromagnetic radiation for a given wavelength to the cornea of the eye before damage to critical optical components will occur. The peak power relates to the MPE thresholds and the standards ANSI sets for laser eye protection. Decreases in pulse duration also decrease exposure time. The resulting increased peak power results in lower MPE thresholds.

The current ANSI Z136.1 eye safety standards were released in 2014. When compared to the previous 2007 recommendations, a significant increase in MPE limits in the 1200 to 1400 nm region with pulse durations from 100 femtoseconds to 30,000

seconds were allowed. The increase was based on minimum visible lesions collected for pulse durations of 100 fs and greater. Substantial attenuation from absorption in the front of the eye such as the vitreous and aqueous humors suggests acceptable radiant exposure levels can be exceptionally high in the NIR regime [3-12]. Even if the assumption that the attenuation of the radiation is still significant enough for shorter duration pulses, the nonlinear effects that those pulses can generate may generate visible light which have lower exposure thresholds.

1.3 Harmonic and Supercontinuum Generation

The nonlinear optical effects primarily important are harmonic generation and continuum generation. A high intensity laser pulse interacting with a sample media causes harmonic generation. A simple model of harmonic generation considers N photons "mixing" into a single photon [Fig. I.1]. This photon has energy equal to the sum of the original N photons and is the Nth harmonic of the original frequency. In terms of atomic interactions, an atom interacts with the intense laser pulse causing a time-dependent dipole moment that radiates at the allowed multiples of the original pulse frequency [13]. The allowed multiples are dependent on the atom or media the field interacts with. When harmonic generation goes above fifth order, it is considered to be high harmonic generation. A recent study in air saw up to ninth order harmonic generation due to filamentation generation [14]. Lower order harmonics such as second and third are quite easily found. Second harmonic generation has been utilized in applications such as microscopy for simple filtering of the excitation light while providing high spatial resolution without use of pinholes [15, 16].

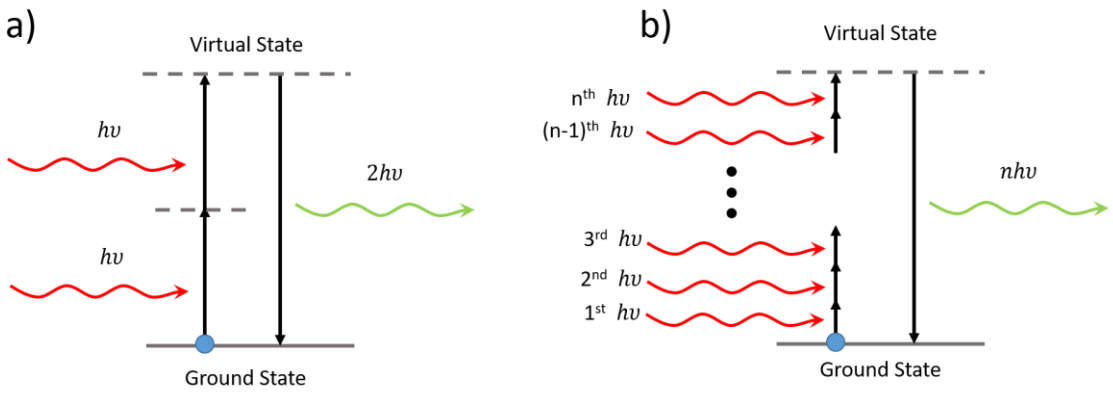

Figure I.1: a) Second harmonic generation and b) Nth harmonic generation. Second harmonic generation occurs when two photons of the same frequency ν collectively excite the molecule into a virtual state. The resulting drop back to the ground state emits a photon with twice the energy and therefore frequency of one of the incident photons. The Nth harmonic is an extrapolation of the second harmonic case.

Supercontinuum generation [17] occurs when the laser pulse interacts with the medium to cause a spectral broadening of the original pulse bandwidth. Spectral broadening [18] is generally the result of self-phase modulation (SPM) which is itself related to the Kerr effect. The Kerr effect describes a nonlinear response of a medium's index of refraction due to an intense laser pulse [19]. The changing or nonlinear refractive index is caused by the nonlinear polarization of the media due to the laser pulse interacting with the medium [20]. The nonlinear change in refractive index is therefore dependent on the time varying intensity of the propagating pulse. A phase shift in the pulse results from the changes in index of refraction over time. The initial pulse has acquired a "chirp" or time varying instantaneous frequency. Studies performed using Raman spectroscopy [21], STED microscopy [22], and optical coherence tomography [23] have all utilized continuum generation.

Harmonic and supercontinuum generation can be understood as a consequence of the optical nonlinearity of a medium. The following treatment on optical nonlinearities and their consequences (harmonic and supercontinuum generation) will follow from Robert Boyd's "Nonlinear Optics" [24]. We begin by considering the dipole moment per unit volume (polarization) $\tilde{P}(t)$ of a material system. The polarization depends on the strength of the applied optical field, $\tilde{E}(t)$. By expressing the polarization as a Taylor series expansion of the field strength, we get:

$$\tilde{P}(t) = \epsilon_0[\chi^{(1)}\tilde{E}^1(t) + \chi^{(2)}\tilde{E}^2(t) + \chi^{(3)}\tilde{E}^3(t) + \cdots] \quad \text{(Eq. 1.2)}$$

The quantity $\chi^{(1)}$ is the linear susceptibility whereas $\chi^{(2)}$, $\chi^{(3)}$, etc. are the second- and third-order nonlinear susceptibilities respectively. The value ϵ_0 is the permittivity of free space. The time-varying polarization acts as a source of new components of the electromagnetic field when the nonlinear regime is reached.

We now apply an electromagnetic field from a laser beam to the polarization equation. The laser beam field is represented as:

$$\tilde{E}(t) = Ee^{-i\omega t} + c.c. \quad \text{(Eq. 1.3)}$$

where ω is the frequency of the optical field, E is the amplitude, and c.c. is the complex conjugate of $Ee^{-i\omega t}$. The beam is incident on a crystal with a nonzero second-order susceptibility. The second-order nonlinear polarization is then given by:

$$\tilde{P}^{(2)}(t) = 2\epsilon_0\chi^{(2)}EE^* + (\epsilon_0\chi^{(2)}E^2e^{-2i\omega t} + c.c) \quad \text{(Eq. 1.4)}$$

The resulting second-order nonlinear polarization provides two terms to consider. The first term is a constant and contributes at the zero frequency. The second term contributes to a polarization at the frequency 2ω. The contribution from the second term

indicates the possibility of generation of radiation at the double of the initial frequency or the second harmonic. Given proper conditions, the second-harmonic generation process can be exceptionally efficient, such that nearly all of the power from the incident radiation is converted to radiation at the second-harmonic frequency. This can be extrapolated to higher order harmonics.

Supercontinuum generation follows from self-phase modulation and the Kerr effect. As described in Boyd [24], self-phase modulation derives from an optical pulse's interaction with a material's nonlinear refractive index causing a change in the phase of the pulse. Boyd begins by adjusting the optical field equation 1.4 by adding a spatial and time varying component to the field amplitude and defining the nonlinear refractive index as:

$$\tilde{E}(z,t) = \tilde{A}(z,t)e^{i(k_0 z - \omega_0 t)} + c.c. \quad \text{(Eq. 1.5)}$$

$$n(t) = n_0 + n_2 I(t) \quad \text{(Eq. 1.6)}$$

where ω_0 is the frequency of the pulse, k_0 is the wavenumber of the pulse, n_0 is the linear refractive index, n_2 is the second-order nonlinear refractive index, and $I(t)$ is the time varying intensity of the field. Two assumptions are made in this theory. First, the medium can respond instantaneously to the pulse intensity. Second, the length of the medium is short enough that no reshaping of the pulse occurs within the medium. The medium alters the transmitted pulse's phase by:

$$\phi_{NL}(t) = -n_2 I(t)\omega_0 \frac{L}{c} \quad \text{(Eq. 1.7)}$$

where L is the length of the medium the pulse propagates through and c is the speed of light in a vacuum. The variance in the phase as a function of time can cause the spectrum

of the transmitted pulse to be broader than the incident pulse. Boyd [24] states that while the spectral content of the transmitted pulse can be determined by calculating its energy spectrum:

$$S(\omega) = \left|\int_{-\infty}^{\infty} \tilde{A}(t) e^{-i\omega_0 t - i\phi_{NL}(t)} e^{i\omega t} dt\right|^2 \quad \text{(Eq. 1.8)}$$

the more intuitive approach is to define the instantaneous frequency $\omega(t)$ of the pulse and derive the broadened spectrum from there.

$$\omega(t) = \omega_0 + \frac{d}{dt}\phi_{NL}(t) \quad \text{(Eq. 1.9)}$$

The instantaneous frequency is centered on the optical frequency ω_0 and varies based on the change in the nonlinear phase. The instantaneous frequency as defined is valid so long as the optical field amplitude, $\tilde{A}(t)$, varies slowly when compared to the optical period. Assuming a Gaussian profile for the incident pulse, the equation for the time dependent intensity can be written as:

$$I(t) = I_0 e^{\frac{-t^2}{\tau^2}} \quad \text{(Eq. 1.10)}$$

where I_0 is the peak intensity and τ is full width half-maximum pulse duration. Figure I.2 represents this pulse.

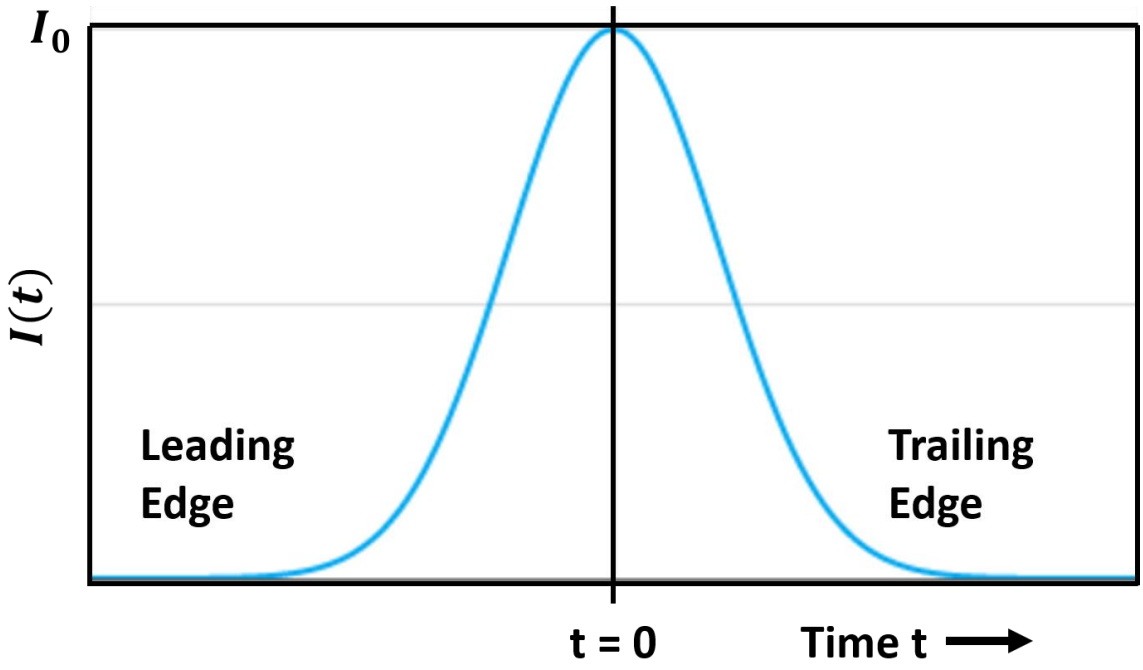

Figure I.2: Time dependent intensity of a Gaussian laser pulse. The pulse has a maximum amplitude of I_0 at time zero. As time increases, the pulse propagates into and through the medium. Therefore, the side of the pulse that first interacts with the medium is at times $t < 0$, also known as the leading edge.

Two terms that will be utilized to describe the pulse are the leading edge and the trailing edge. The term "edge" refers to the transition of the pulse from low to high intensity or high to low intensity as it propagates through the medium. The leading edge is the considered to be the front of the pulse, or the first part of the pulse that interacts with the medium, where the intensity is going from zero to I_0. The pulse intensity described in Equation 1.10 has its leading edge at time $t < 0$. Meaning that the medium first interacts with the pulse intensities on that side of time zero. The pulse's trailing edge is considered the back edge of the pulse. The trailing edge is the portion of the pulse where the intensity is going from high to low intensity or from I_0 to zero. The Gaussian pulse

from Equation 1.10 has its trailing edge at time $t > 0$. The nonlinear phase shift and instantaneous frequency are then determined to be:

$$\phi_{NL}(t) = -n_2\omega_0\frac{L}{c}I_0 e^{\frac{-t^2}{\tau^2}} \quad \text{(Eq. 1.11)}$$

$$\omega(t) = \omega_0 + 2\frac{n_2\omega_0 L I_0}{c\tau^2}te^{\frac{-t^2}{\tau^2}} \quad \text{(Eq. 1.12)}$$

The instantaneous frequency equation now describes how the pulse frequency changes as it passes through the nonlinear medium [Fig. I.3]. Before it arrives, the pulse has a frequency of ω_0. As it begins to pass through the medium, the leading edge of the pulse experiences a frequency shift to lower frequencies. Eventually the center of the pulse, where the intensity is the highest, arrives but experiences no frequency shift. As the pulse continues to travel through the medium, the trailing edge of the pulse instead experiences a shift to higher frequencies. By taking the time derivative of the instantaneous frequency and setting it equal to zero, one can find the maximum and minimum values for the shifts in the frequency. The instantaneous frequency indicates that either increases in the second-order nonlinear refractive index or the maximum intensity of the pulse will lead to increases in the broadening. If the spectral broadening becomes large enough such that a wide range of frequencies are observed with a reasonably smooth spectral continuum, then the pulse is said to be a supercontinuum.

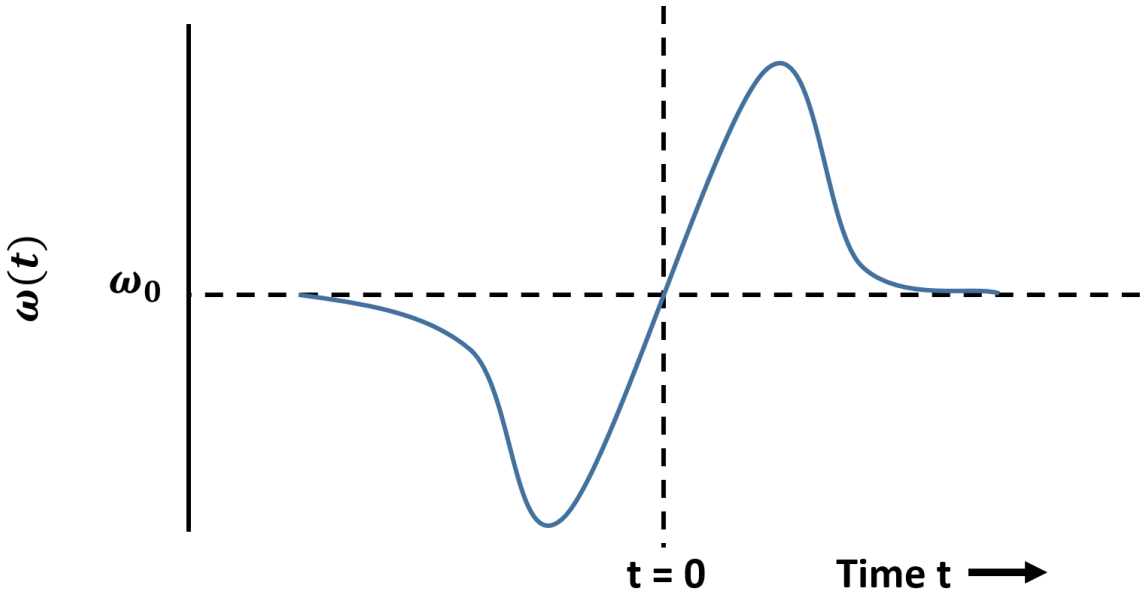

Figure I.3: The instantaneous frequency demonstrates how the pulse is spectrally broadened as it passes through the medium. Before the pulse arrives at the medium, it has a frequency of ω_0. As the leading edge interacts with the medium, the change in the nonlinear phase shift induces a red shift in the frequency. The center of the pulse, with the highest intensity, experiences no shift. The trailing edge has a blue shift in its frequency.

1.4 Filamentation

Harmonic and supercontinuum generation can occur in a myriad of ways and need not just be due to a highly nonlinear material. While the medium that the high intensity light passes through may cause the effect, another method of generation is through laser filamentation. A filament's unique ability to beat the diffraction limit over extended distances makes them of interest and important to many studies such as atmospheric filamentation. Studies utilized atmospheric filamentation to demonstrate applications of femtosecond (fs) LIDAR remote sensing [25], laser-induced breakdown spectroscopy [26], and white light continuum ranging [27].

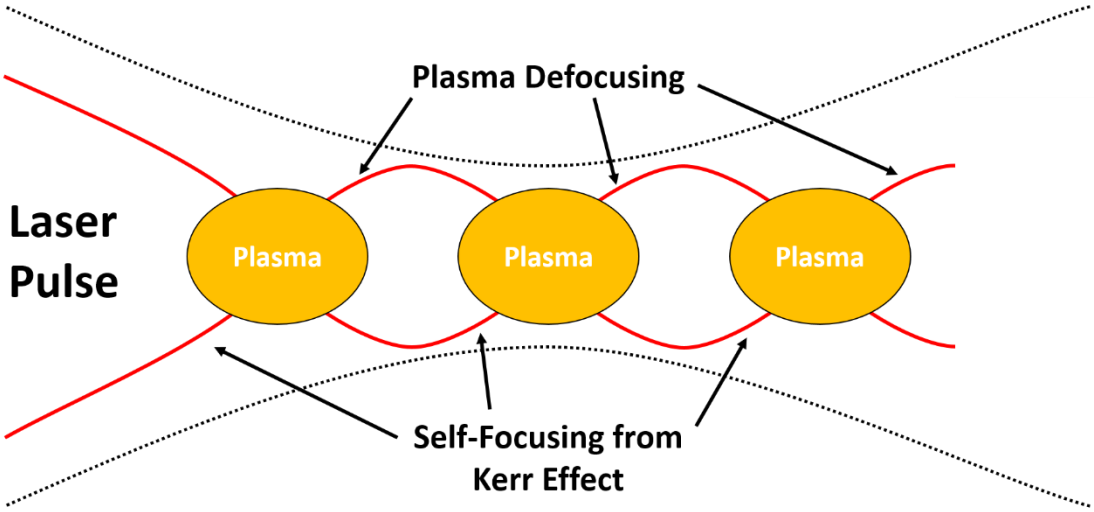

Figure I.4: Filamentation. The black dotted outer lines demonstrates the standard diffraction limit of a focused laser beam. The red inner lines demonstrate a filament beating the diffraction limit while balancing the effects of self-focusing and plasma defocusing. Adapted from Couairon, et al. "Femtosecond filamentation in transparent media" [28].

The nonlinear laser filamentation effect occurs when self-focusing and plasma generation combine to beat the diffraction limit of a beam in a gas, liquid, or solid material well past the Rayleigh length [28]. The filament is generated when Kerr-lens self-focusing is started by interaction of the laser pulse with an intensity dependent refractive index (Eq. 1.6) [Fig. I.4]. Self-focusing only occurs when the incident pulse power (Eq. 1.13) exceeds the required critical power (Eq. 1.14). Passing the power threshold will cause the Kerr lensing to beat the diffraction limit and collapse the beam. The very collapse will generate multiphoton ionization or plasma in the medium. The generated plasma prevents further collapse and acts as a defocusing lens. Self-focusing and plasma defocusing will balance for a short time creating multiple thin filaments

beating the Rayleigh length. The high intensity of the light in the filament can cause SPM leading to continuum generation.

$$P_{pulse} = K\frac{E_{pulse}}{t_{pulse}}, K = 0.94 \text{ for a Gaussian Beam} \quad \text{(Eq. 1.13)}$$

$$P_{crit} = \frac{C\lambda^2}{8\pi n_0 n_2}, 3.72 < C < 6.4 \quad \text{(Eq. 1.14)}$$

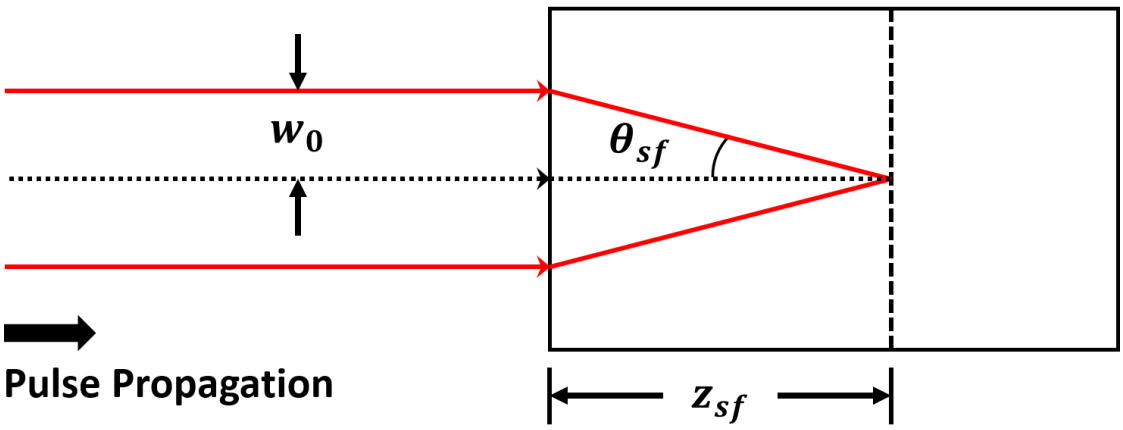

Figure I.5: Self-focusing. A collimated laser beam with a beam waist radius of w_0 is incident upon a nonlinear medium. The intensity profile of the beam is such that the on-axis intensity is larger than that of the edges. The result is a spatially varying refractive index, where the refractive index decreases until it becomes just the linear refractive index as one moves away from the beam axis. The self-focusing distance (z_{sf}) and angle (θ_{sf}), where z_{sf} can be found by application of Fermat's principle. Adapted from Robert Boyd's "Nonlinear Optics" [24].

Boyd [24] models the self-focusing process by at first ignoring diffraction effects, due to an assumption that either the beam intensity or diameter is sufficiently large. A collimated laser beam of radius w_0 and an on-axis intensity of I_0 passes into a nonlinear optical medium where $n_2 > 0$. The interaction of the beam with the medium causes the beam to self-focus. The self-focusing distance is called z_{sf} and is the distance

from the input face of the medium to the focal point. The self-focusing distance is found by application of Fermat's principle. Fermat's principle essentially states that light will follow the path of least time. More explicitly, Fermat's principle states that the optical path length between two points, a and b, of all rays from a wavefront to the self-focus must be equal:

$$Optical\ Path\ Length = \int_a^b n(\boldsymbol{r})dl \qquad \text{(Eq. 1.15)}$$

The three rays shown in Figure I.5 are the central ray (ray at the center of the beam, and the two marginal rays (rays at the radius of the beam). The marginal rays experience a lower nonlinear refractive index (Eq. 1.6), due to the majority of the energy in the beam being located towards the center of the beam. At first approximation, the marginal rays can be said to experience the linear refractive index, n_0 of the medium. The central ray experiences a refractive index of $n_0 + n_2 I_0$. The difference in the refractive index based on the distance from beam axis, where the optical intensity is the largest, is essentially how a material lens operates. A typical converging lens deforms a laser beam's wavefront [Fig. I.6]. The originally flat wavefront from the collimated beam becomes curved after passing through the lens.

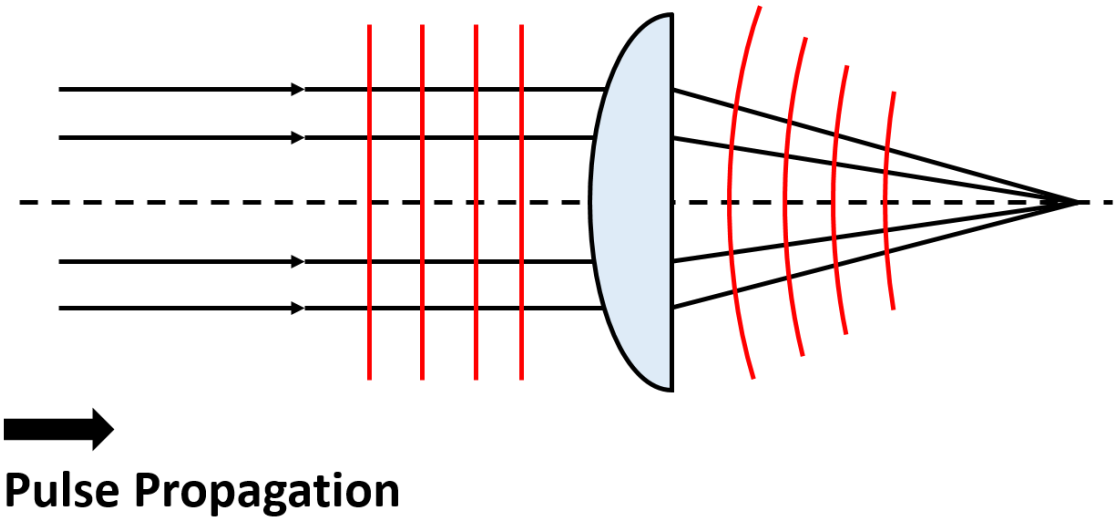

Figure I.6: Optical wavefront deformation by a lens. The collimated laser beam has a flat wavefront before interacting with the positive lens. After passing through the lens, the wavefront becomes curved and converges on the focal point.

The medium induces a phase delay whose magnitude depends on the intensity of the light transmitted and thus the distance from the center of the collimated beam. The self-focusing effect can be said to be caused by a Kerr lens. Applying Fermat's principle to the two ray paths shows:

$$(n_0 + n_2 I_0) z_{sf} = \frac{n_0 z_{sf}}{\cos \theta_{sf}} \qquad \text{(Eq. 1.16)}$$

where θ_{sf} is the angle between the central ray or beam axis and the marginal rays. Assuming that θ_{sf} is very small, $\cos \theta_{sf}$ then can be approximated as $1 - \frac{1}{2}\theta_{sf}^2$. Solving Equation 1.16 for θ_{sf} gives the self-focusing angle and from there find the self-focusing distance, again using the small angle approximation:

$$\theta_{sf} = \sqrt{\frac{2n_2 I_0}{n_0}} \quad \text{(Eq. 1.17)}$$

$$z_{sf} = w_0 \sqrt{\frac{n_0}{2n_2 I_0}} \quad \text{(Eq. 1.18)}$$

Assuming that the beam exhibits a Gaussian profile, the beam intensity can be approximated by:

$$I_0 = \frac{2P}{\pi w_0^2} \quad \text{(Eq. 1.19)}$$

Using Equation 1.19 and the critical power given by Equation 1.14, Equation 1.18 can be modified:

$$z_{sf} = \sqrt{\frac{2\pi^2}{C}} \times \frac{w_0^2 n_0}{\lambda^2} \sqrt{\frac{P_{cr}}{P}}, \text{ for } P \gg P_{cr} \quad \text{(Eq. 1.20)}$$

Thus giving a calculation that can be done with measurable parameters and doesn't require prior knowledge of the nonlinear refractive index. The self-focus distance assumes that the laser power is greater than the critical power.

The result of the self-focusing of the pulse is the large increase in the intensity of the electromagnetic radiation in the focal region. The intense field in the focal region can ionize the electrons in the medium creating a plasma [28]. The increased electron density from the plasma lowers the susceptibility of the medium. The reduction in susceptibility leads to a decrease in the index of refraction. In an optically isotropic medium, the second-order nonlinear refractive index, n_2, is related to the third-order susceptibility, $\chi^{(3)}$, by [28]:

$$\chi^{(3)} = \frac{4\epsilon_0 c n_2 n_0^2}{3} \quad \text{(Eq. 1.21)}$$

The decrease in the index of refraction due to the plasma is given by [17]:

$$n \simeq n_0 - \frac{\rho(r,t)}{2\rho_{cr}} \quad \text{(Eq. 1.22)}$$

where $\rho(r,t)$ is the density of the free electrons and ρ_{cr} is the critical plasma density. Should the density of the free electrons become higher than the critical density, the plasma becomes opaque to the pulse. The plasma acts as a defocusing or divergent lens due to this reduction in the refractive index. This prevents the beam from completely collapsing on itself.

The pulse not only undergoes changes in spatial profile, but also in its temporal profile, due to the plasma. The plasma defocusing acts locally in time. The leading edge of the pulse generates the plasma causing the trailing edge to experience the defocusing effect. When the plasma defocusing balances with the self-focusing effect, the diffraction limit can be beaten over a significant distance, thereby generating a filament [28].

The plasma also contributes to the spectral broadening the filament along with the effects of self-phase modulation and self-steepening [28]. Self-phase modulation plays a role in the spectral broadening of the pulse, due to the time dependent laser intensity interacting with an intensity dependent refractive index (Eqs. 1.5 and 1.6). The photo-ionization and plasma generation can modify the instantaneous frequency given by Equation 1.12 by contributing an additional frequency shift:

$$\delta\omega_{plasma} \sim \frac{\omega_0 L}{2cn_0\rho_{cr}} \frac{\partial\rho(r,t)}{\partial t} \quad \text{(Eq. 1.23)}$$

The frequency shift contributes to an increase in the frequency in the leading edge of the pulse [28].

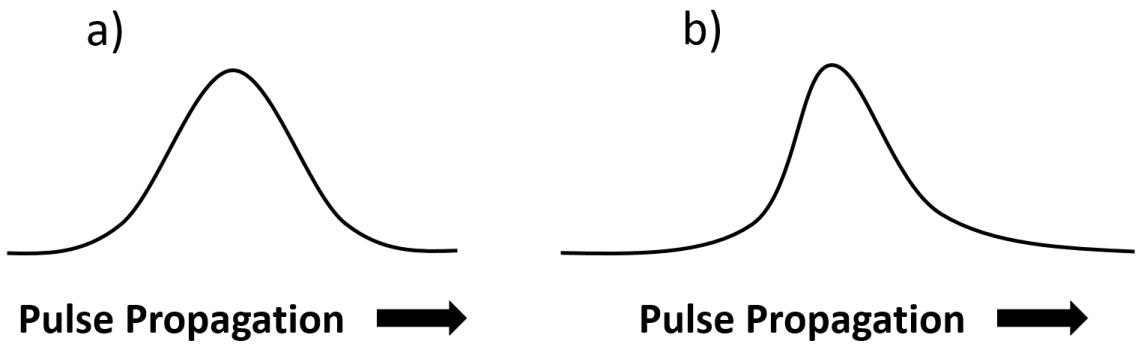

Figure I.7: Self-steepening. a) A Gaussian laser pulse begins propagating through a nonlinear medium. b) As the pulse interacts with the medium, the more intense portions of the pulse are slowed by interaction with a higher refractive index. The trailing edge of the pulse then begins to accrue a steeper slope as the peak of the pulse is slowed and the trailing edge catches up, which is known as self-steepening. Adapted from Robert Boyd's "Nonlinear Optics" [24].

Self-steepening describes how the group velocity of the electromagnetic radiation of the pulse is altered by the medium [24,28]. Given a positive second-order nonlinear refractive index, the group velocity is slowed depending on its intensity. The more intense the radiation, the slower the propagation through the medium. Assuming a Gaussian pulse profile, the leading edge of the pulse is generally not significantly affected. As pulse propagates through the medium, the peak is slowed down relative to the rest of the pulse, such that the trailing edge catches up to the peak [Fig I.7]. The temporal spectral profile then forms a steep edge in the trailing portion of the pulse. A side effect of self-steepening is the trailing portion of the pulse undergoes faster self-focusing than the leading edge, as well as undergoing the generation of higher frequency light.

1.5 Raman Spectroscopy

Raman spectroscopy is a useful tool for chemical identification and quantification. A significant benefit of the Raman process to biological organisms is the ability to investigate sensitive cells without the need for chemically tagging the molecules of interest or destroying the cell [29-31]. Raman spectra are generated by the inelastic scattering of light off of a molecule, whereas Rayleigh scattering is an elastic collision.

Raman and Rayleigh scattering are dependent upon the polarizability of the molecule in the interaction. The excitation of the incident light upon the molecule causes an excitation in the vibrational or rotational levels of the molecule. The excitation causes the molecule to enter an excited virtual state. If the molecule returns to its initial state, the scattered photon will retain its energy and have the same frequency. Raman scattering occurs when the molecule couples to a different vibrational state than the one it began in. By conservation of energy, the molecule ending in a different vibrational state means that the scattered photon must either gain or lose energy and therefore increase or decrease in frequency.

Stokes Raman scattering occurs when the scattered light has a lower frequency than the incident light and the molecule moves from the ground state to an excited vibrational state [Fig. I.8]. Anti-Stokes occurs when the light gains energy from the molecule and the molecule moves from an excited vibrational state to the ground state. The Raman scattering effect is significantly weaker than the Rayleigh scattering effect. The Raman scattering effect is so weak that only about 1 in every 10^{10} photons

experience it. The ratio of Stokes to Anti-Stokes photons depends upon the initial vibrational states of the population of molecules in the material observed, which is dependent upon the temperature. Therefore, Stokes scattering will occur more often than Anti-Stokes when dealing with a population of molecules at room temperature. More molecules will be in the ground state at room temperature than in an excited vibrational state.

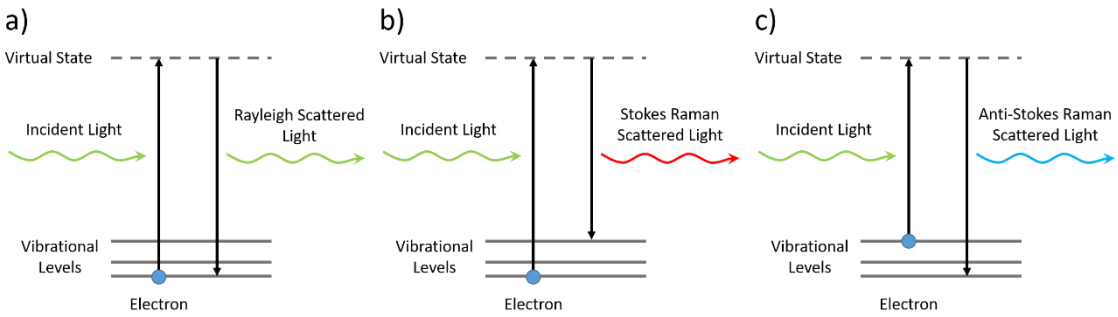

Figure I.8: a) Rayleigh Scattering, b) Stokes Raman Scattering, and c) Anti-Stokes Raman Scattering. Note about "vibrational levels": figures' vibrational states are just to represent the multiple states of a molecule, distance of separation in figure is not representative of real vibrational states.

Raman spectroscopy occurs when Raman scattering is applied using a monochromatic intense light source. The Stokes and Anti-stokes photons of the Raman spectrum form a symmetric array of peaks around the fundamental, or incident, laser excitation source. The symmetry of peaks arises due to the difference in energy between any two vibrational states of the molecule in both processes corresponding to only those two states. The wavelength of these peaks is dependent on the wavelength of the laser

exciting the molecule, however the vibrational energy state change is independent of wavelength. This makes it desirable to plot Raman spectra in a manner that demonstrates the independence of the Raman scattered or shifted photons from the incident excitation light. To accomplish this goal, wavelength is converted into wavenumber and the relative shift in wavenumber from the excitation wavelength is computed. Wavenumber has a linear relationship with energy and thus allows for a universal spectra to emerge. The Raman shift is calculated by:

$$\Delta\nu = \left(\frac{1}{\lambda_0} - \frac{1}{\lambda_1}\right)^{-1} \quad \text{(Eq. 1.24)}$$

where λ_0 is the excitation wavelength, λ_1 is the Raman wavelength, and $\Delta\nu$ is the Raman shift. The peaks in the Raman spectrum are correlated to specific vibrational modes of the molecule and the height of the peak tells us about the concentration of the molecule in the observed sample.

CHAPTER II

SUPERCONTINUUM GENERATION IN ZINC SELENIDE FROM MIR LASER PULSES

2.1 Background and Motivation

Zinc selenide (ZnSe) is a particularly interesting semiconducting optical medium to investigate nonlinear phenomena. Its nonlinear properties have caused it to be used for broadband frequency conversion [32] as well as harmonic generation [33]. An intrinsic semiconductor with a 2.71 eV band gap [34], ZnSe is a member of the zinc-blende crystal group, thereby making them optically isotropic without having a center of inversion. They can therefore provide even number harmonics when optically pumped [35]. Perhaps most critically, ZnSe has a high optical damage threshold of 0.53 J/cm^2 for 500 fs pulses at 1030 nm [36]. Finally, its nonlinear index of refraction is 6×10^{-15} cm^2/W [37]. The crystal grains of polycrystalline ZnSe exhibit a quasi-phase matching condition. Enhancements in difference frequency generation (DFG) [38], sum frequency generation [39], and second harmonic generation [32,39] have been observed due to the quasi-phase matching in ZnSe crystal grains. Even extended phase matching conditions for broadband frequency conversion have been reported due to the quasi-phase matching conditions of its crystal grains [39,40].

The same properties that make ZnSe useful as a medium for investigating nonlinear phenomena, also make it widely used in the design of optical elements in the MIR. The material is used frequently in infrared laser systems and experiments as lenses, windows, beamsplitters, and prisms due to a high optical transmission from 0.5 to 20

μm. The ubiquity of ZnSe in optical components indicates a possibility of strong generation of unintended wavelengths of electromagnetic radiation due to its strong nonlinear refractive index. When dealing with mid-infrared wavelengths, laser operators may be unintentionally exposed to harmful radiation from supercontinuum or harmonic generation that laser eye protection (LEP) is not designed to protect against. The ANSI laser eye safety standards set the MPE limits by wavelength and pulse duration. The limits for retinal exposure in the visible to near-infrared are lower than the mid-infrared due to the aqueous and vitreous humors of the eye absorbing strongly in the mid-infrared [2]. These concerns are backed up by previous work detailing visible blue filaments generated in ZnSe from high intensity pulses near the front surface of ZnSe windows [41,42]. The generated filament in ZnSe has resulted in supercontinuum generation [40,43].

The generation of supercontinuum light in ZnSe was investigated using MIR pulses ranging from 4 to 20 μm. Preliminary results indicated significant broadband supercontinuum generation reaching into the visible. While visible light energy was not measured for comparison with MPE limits set by ANSI due to time constraints, the breadth of continuum generation is cause for concern regarding eye safety.

2.2 Materials and Methods

A study was performed in polycrystalline zinc-selenide (ZnSe) using mid-infrared (MIR) light. A Spectra Physics® Spitfire Ace regenerative amplifier (model 8PTFA-100F-1K-ACE) was employed in this experiment. It outputs 15 mJ pulses at 1 kHz with ~85 fs pulses at a wavelength of 800 nm. The Spitfire Ace is followed by an

HE TOPAS (model TH8F1), an Optical Parametric Amplifier (OPA), with a tuning range from 1100 to 2900 nm. The system was based in the designs in [44, 45] The OPA produces a signal and an idler beam from interaction with the OPA crystal. The signal beam wavelengths cover the range from 1100 to 1600 nm, whereas the idler beam covers from 1600 to 2900 nm. Typical pulse output energy of the TOPAS signal and idler beams ~3 mJ. The signal and idler outputs of the OPA are sent to a difference frequency generator (DFG). The DFG produces tunable light from 4 to 20 μm. Typical energy output for 4, 6, 8, 10, and 20 μm is 220, 160, 75, 30 and 10 μJ respectively with a linear decrease in energy output from 10 to 20 μm. We simultaneously probed the light generated in the ZnSe plate using an Ocean Optics® NIR-512 infrared spectrometer and an Ocean Optics® USB2000+ visible spectrometer.

As shown in Figure II.1, the MIR light from the DFG is passed through an iris which is used to block the unconverted signal and idler beams. The interaction with the DFG crystal between signal and idler also caused sum frequency generation to occur, producing the 800 nm fundamental. A germanium filter was added to block the 800 nm fundamental from further propagation in the setup. An uncoated germanium window typically has a low wavelength cutoff of approximately 2000 nm. A positive 10 cm focal length ZnSe lens (labeled L1 in Fig. II.1) focuses the beam into our ZnSe plate. The supercontinuum generated light is then collimated using a 75 mm, calcium-fluoride (CaF2) lens (labeled L2 in Fig. II.1). A ZnSe lens is necessary for the focusing of the MIR light due to its transmission window from 0.5 to 20 μm. CaF2 can transmit light into the ultraviolet, lower than ZnSe, but its higher wavelength cutoff is approximately 9

μm. The NIR spectrometer can only detect wavelengths of light up to 1750 nm. Our spectral detection is therefore not limited due to collection optics. A positive 250 mm CaF2 lens (labeled L3 in Fig. II.1) is used to focus the collected continuum generated light onto the slits of the infrared (labeled S1 in Fig. II.1) and visible (labeled S2 in Fig. II.1). A cold mirror from Edmund Optics (stock #64-447, labeled M3 in Fig II.1) with an angle of incidence of 45° separated the infrared and visible wavelengths of light to allow for simultaneous detection of supercontinuum light.

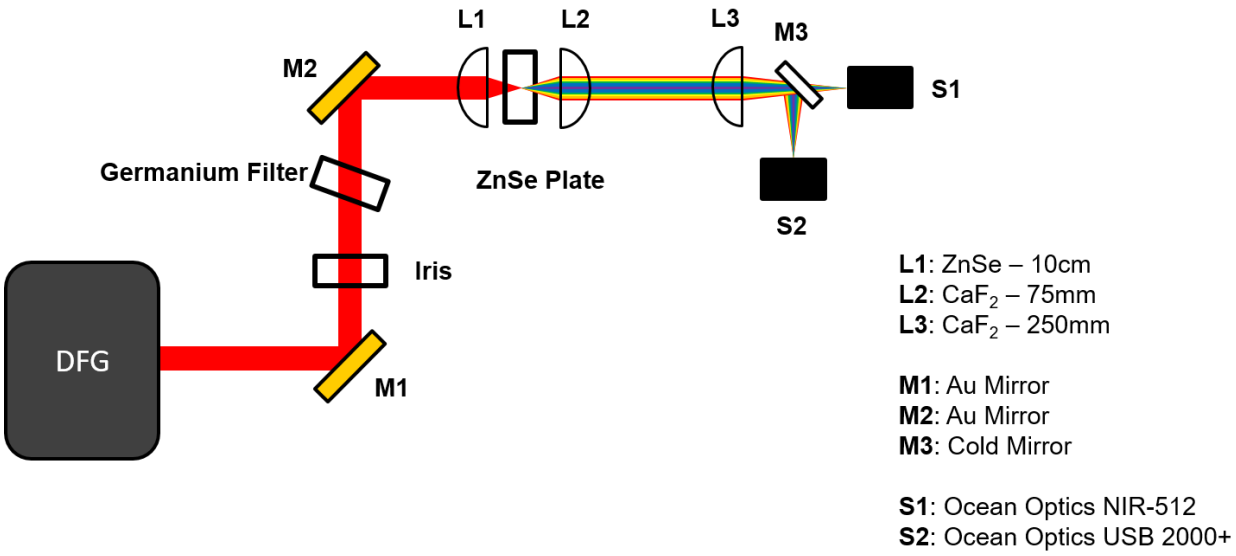

Figure II.1: Experimental setup to observe supercontinuum generation in ZnSe

2.3 Results and Discussion

The MIR wavelengths that interacted with the ZnSe produced an extremely strong supercontinuum as evidenced by Figure II.2. The wavelength range of the NIR-512 spectrometer is roughly from 880 to 1750 nm. The rapid decay of the spectra at the

cutoff region of the NIR spectrometer appears to indicate that the spectral broadening causing the continuum generation goes well on into the MIR. Unfortunately without a detection system that can observe those MIR wavelengths, we cannot confirm that the spectral broadening is a single continuum from the original pulse wavelength.

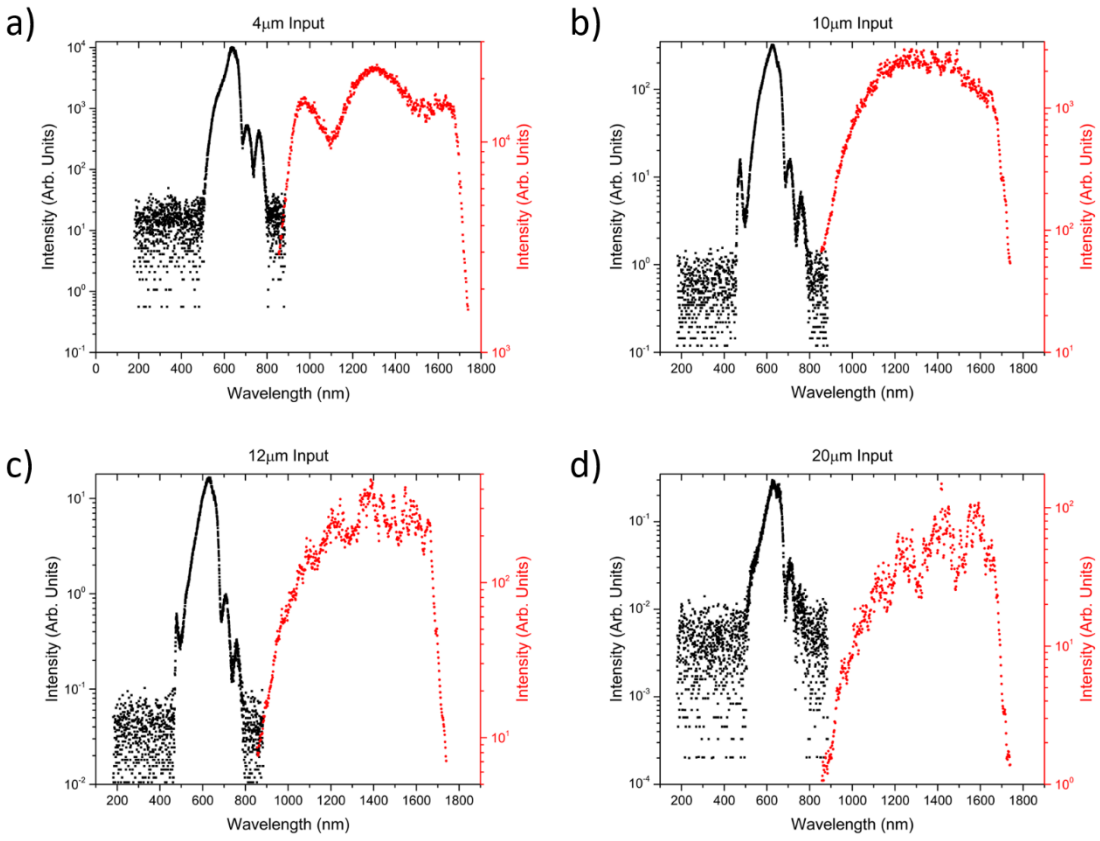

Figure II.2: Supercontinuum generation in ZnSe from an input beam wavelength of a) 4 μm, b) 10 μm, c) 12 μm, and d) 20 μm. The black spectra were collected from an Ocean Optics visible spectrometer and the red from an Ocean Optics NIR spectrometer. The spectra all have a common feature of a dip in the continuum from ~600 to 1000 nm which are due to the transmittance/reflectance of the cold mirror. The small "peaks" in this region are due to the variations in the reflectance curve of the cold mirror. Of note are the harmonic peaks generated by the 10 and 12 μm beams at 475 and 478 nm respectively. Those correspond to the 21st and 25th harmonic, respectively, of the incident 10 and 12 μm beams.

Self-phase modulation theory would imply that the observed spectra are part of a single continuum. The pulse's interaction with the medium would lead to self-phase modulation thereby causing spectral broadening. The collected spectra have a few features that need to be addressed if a single continuum is to be claimed. The spectra collected in the visible spectrometer shows a decrease in intensity from ~600 nm to the end of the spectrometer's range around 800 nm. The other issue is that the two peaks we see between 600 and 800 nm, do not correspond to actual harmonics of the MIR beam. The false peaks we observe in the visible spectra are caused by the cold mirror from Edmund Optics (stock #64-447). The cold mirror utilized reflects around 95% of light from 400 to 690 nm. At roughly 700 nm, the cold mirror reflects approximately half of the light. The cold mirror transmits approximately 90% of light from 750 to 1200 nm. The transmittance curve from the Edmund Optics catalog demonstrates the ideal performance of the cold mirror. A slight deformity or damage of the coating could cause slight changes in the wavelength dependent transmittance and reflectance curves of the cold mirror. The peaks in the 600 to 800 nm area are likely caused by slight changes in the reflectance and transmittance.

The 10 and 12 μm supercontinuum spectra have one significant difference in that they have a small peak just below the low wavelength end of the visible continuum. These peaks are far enough away from the concerning 600 to 800 nm region to be caused by it. When compared to predicted harmonics, we find that the 10 μm beam has produced a 21st harmonic at 475 nm and the 12 μm beam produced a 25th harmonic at 478 nm. The evidence of harmonic generation seems to indicate we have reached a

saturation limit where supercontinuum generation has drown out the harmonic generation signal. Table II.1 shows the results for each MIR wavelength used.

Table II.1: Summary of Supercontinuum and Harmonic Spectral Data for MIR Pump Laser in ZnSe

Wavelength (μm)	Supercontinuum Range 1 (nm)	Supercontinuum Range 2 (nm)	Predicted Harmonic (nm)	Observed Harmonic (nm)
4	510-795	880-1720	NO	NO
6	510-795	880-1720	NO	NO
8	500-790	880-1720	NO	NO
10	460-775	880-1720	476 (21^{st})	475 (21^{st})
12	470-780	880-1720	480 (25^{th})	478 (25^{th})
14	480-780	880-1720	NO	NO
16	500-780	880-1720	NO	NO
18	500-800	880-1720	NO	NO
20	510-730	880-1720	NO	NO

Acronyms: Not Observed (NO), Not Measured (NM)

2.4 Conclusions

A study on the interaction between high intensity MIR pulses and ZnSe was performed. The DFG produced wavelengths from 4 to 20 μm that were used to generate a supercontinuum and gave evidence of high harmonic generation. Work remains to be done however. The pulses both before and after interacting with the ZnSe need to be characterized in a systematic way detailing their energy and beam width. Only through accomplishing that will we be able to come to conclusions on whether the ANSI standards would be appropriate in our setup. ZnSe is a commonly used optic material for lasers in the MIR. As higher energy MIR lasers become available, it will be important for operators to know how the material will respond to increasing intensities.

CHAPTER III

FILAMENTATION IN ATMOSPHERIC AIR FROM TUNABLE NIR PULSES

3.1 Background and Motivation

Filamentation in atmospheric air has been until recently limited to generation from lasers in the visible and NIR, due to restraints imposed by the required high pulse energies and short pulse durations only available in this spectral range [46-56]. Filamentation has been explored for a myriad of cases including high harmonic generation (HHG), supercontinuum generation, and attosecond laser pulses [28,57,58]. In particular, filamentation when applied to atmospheric air is of interest for remote sensing when utilized with laser-induced breakdown spectroscopy [26,59] and white light continuum ranging [27]. Furthermore, filaments can be applied to solve problems with long-range signal transmission or delivery of high-power beams over significant distances [25,60].

The introduction of laser sources with tunable wavelengths from the near to mid-infrared opens new avenues of exploration of laser filamentation. These avenues for exploration also lead to areas of concern for safety. The ANSI standards MPE limits for eye safety are determined by wavelength and pulse duration [2]. Nonlinear effects can change the exposed wavelength however, and as a result, may render laser eye protection (LEP) used by laser operators ineffective. If a generated filament produces supercontinuum or harmonic light with sufficient intensity outside of the protective range of LEP, injury to the retina may occur. The lower exposure limits in the visible are particularly threatening to the retina [2].

To investigate the potential eye hazards from nonlinear effects, filaments were generated in atmospheric air from tunable NIR laser. The wavelengths used for filament generation ranged from 1100 to 2400 nm. The spectra of the generated supercontinuum and harmonic light was captured from a projection of the light on a sheet of paper by use of optical fibers. The spectra from the center and the fringe of the projected light were observed using visible and NIR spectrometers. After collection of the spectra, the experiment was modified to measure the energy of the visible light generated from the filament and compare it with established MPE limits. Visible light generated by the filament was determined to have exceed MPE limits in several cases.

3.2 Materials and Methods

A Spectra Physics® Spitfire Ace regenerative amplifier (model 8PTFA-100F-1K-ACE) was employed in this experiment. It outputs 15 mJ pulses at 1 kHz with ~85 fs pulses at a wavelength of 800 nm. The Spitfire Ace is followed by an HE TOPAS (model TH8F1), an Optical Parametric Amplifier (OPA), with a tuning range from 1100 to 2900 nm. The system was based in the designs in [44, 45] It produces a signal and an idler beam from interaction with the OPA crystal. The signal beam wavelengths cover the range from 1100 to 1600 nm, whereas the idler beam covers from 1600 to 2900 nm. Typical pulse output energy of the TOPAS signal and idler beams ~3 mJ.

As shown in Figure III.1(a), the HE TOPAS output beams are sent through the same path by use of a gold flip mirror (Au-FM). A 1000 nm long-pass filter (Thorlabs® FGL-1000, labeled L in Fig. III.1(a)) eliminated visible light output from the OPA along with any residual fundamental light. Neutral density filters (labeled F in Fig. III.1(a))

acted as a coarse power control for the beams. A CaF2, positive 75 mm focal length lens (labeled L1 in Fig. III.1(a)) focused the light creating the filament. The resulting supercontinuum and harmonics were projected onto a blank sheet of paper. The spectra of the continuum and harmonics were collected using three spectrometers at each selected wavelength for three pulse energies. An Ocean Optics® USB 2000+ (labeled V1 in Fig. III.1(a)) and an Ocean Optics® NIR-512 (labeled IR1 in Fig. III.1(a)) were pointed at the center of the supercontinuum to collect the visible and infrared spectrums respectively. A second Ocean Optics® USB 2000+ spectrometer (labeled V2 in Fig. III.1(a)) recorded the spectra of the visible fringe. We accounted for the light absorption in the spectrometer fibers as well as spectrometer efficiency by utilizing an Ocean Optics® LS-1 Tungsten Halogen lamp. The lamp light was coupled into the spectrometer fibers and the resulting spectra were recorded. A correction was then applied to the measured LS-1 spectra by comparing it to the expected spectra of a 3100 K blackbody. The resulting correction curves were utilized in correcting the harmonic and supercontinuum spectra.

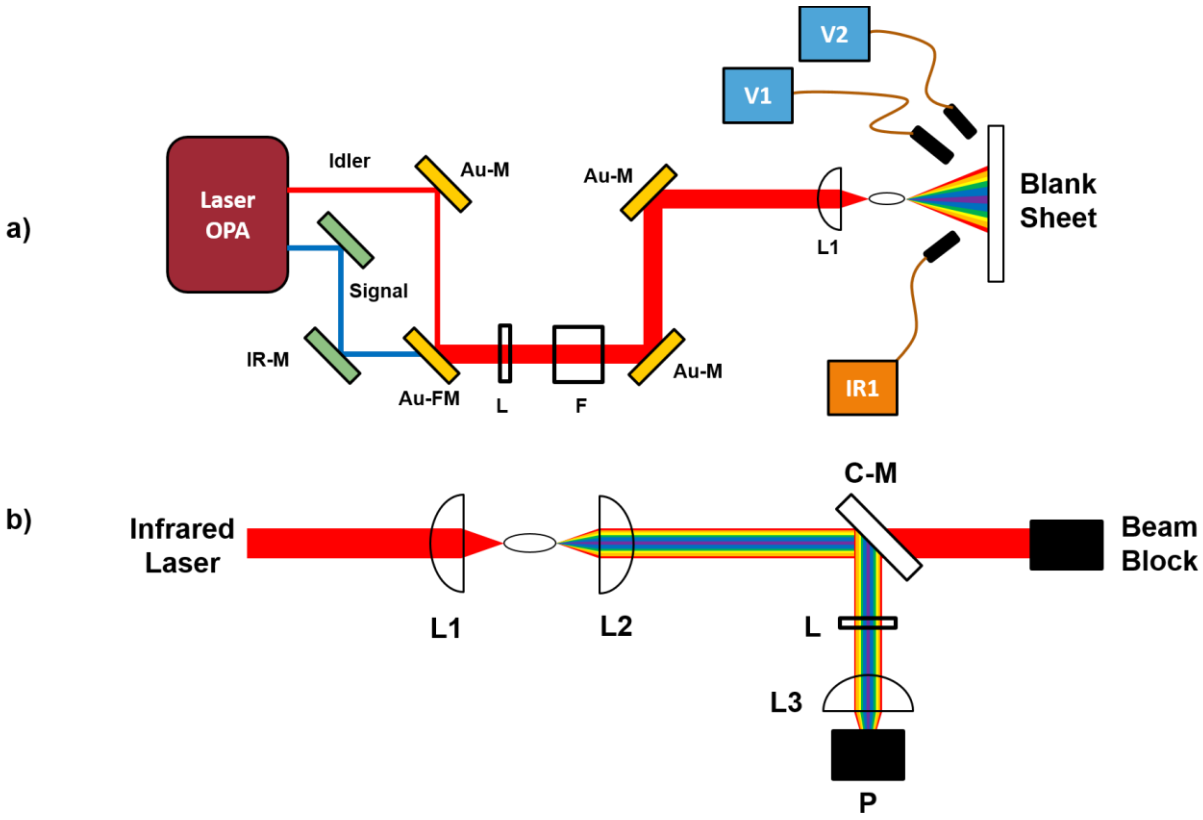

Figure III.1: a) Experimental setup to observe harmonic and supercontinuum generation. b) Setup for visible light collection and power measurement after supercontinuum generation.

The experiment was modified to collect the resulting visible light from continuum and harmonic generation (Fig. III.1(b)). A positive 200 mm focal length lens (labeled L2 in Fig. III.1(b)) placed after the filament collimated the light. The cold mirror (labeled C-M in Fig. III.1(b)) reflected the visible light while transmitting the leftover infrared. A 1-inch diameter BK7 positive lens (labeled L3 in Fig. III.1(b)) decreased beam width to fit the remaining visual light on the Coherent® PM10 power meter (labeled P in Fig. III.1(b)). The power was measured with and without a 1000 nm long-pass filter (L) in the beam path. Power measurements were taken from 1100 to 1600 nm with 100 nm steps. After completion, the positive 200 mm focal length lens

was replaced with a positive 100 mm focal length lens and measurements were recorded with and without the long-pass filter. An Agilent® Cary 6000i spectrophotometer determined the absorption of the infrared light due to the 1000 nm long-pass filter from 200 to 1600 nm. The conversion efficiency of the filament and the energy of the filament's output pulse were calculated after accounting for absorption of the 1000 nm filter.

3.3 Results and Discussion

The input wavelengths ranging from 1100 to 2400 nm produced filaments and a supercontinuum. Figure III.2 shows images taken of the continuum projected onto paper. Examination the center and fringe of the supercontinuum by spectrometer measurements showed the center containing harmonic generation and a spectrally broadened infrared source wavelength. The fringe consisted only of spectrally broadened supercontinuum light.

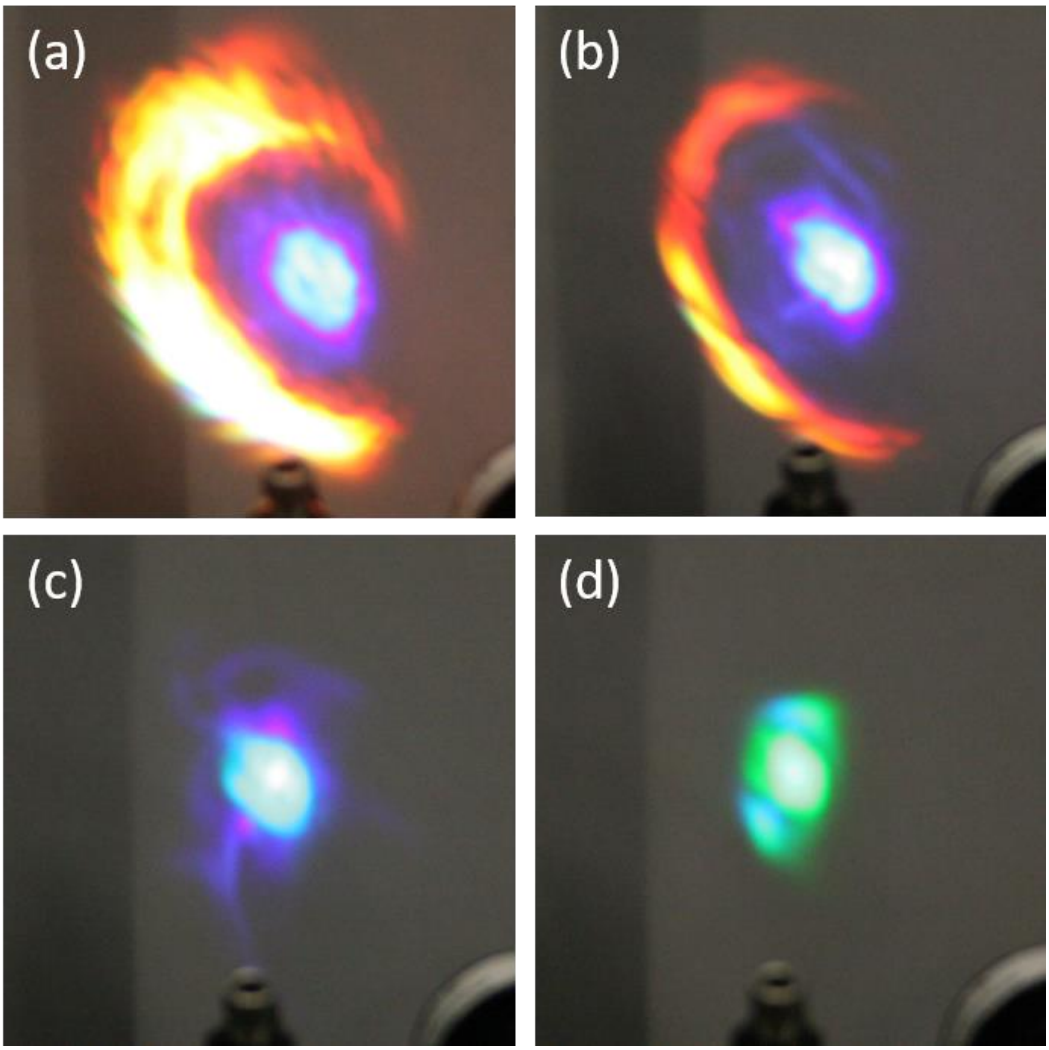

Figure III.2: Images of supercontinuum generation from filamentation imaged on a blank sheet for source wavelength of a) 1300 nm, b) 1400 nm, c) 1500 nm, and d) 1600 nm idler.

Comparing Fig. III.2(a) with III.2(d) we notice that as we move from the signal wavelengths to the idler, the fringe intensity decreases and moves from one side of the center to the other. The cause is imperfect alignment between the beam path and focusing lens, which was only magnified by self-focusing. Sample spectral data are presented in Figure III.3. Supercontinuum generation was observed in the visible and

infrared. Harmonic generation was largely confined to the center region. No harmonic generation higher than 3rd order was observed.

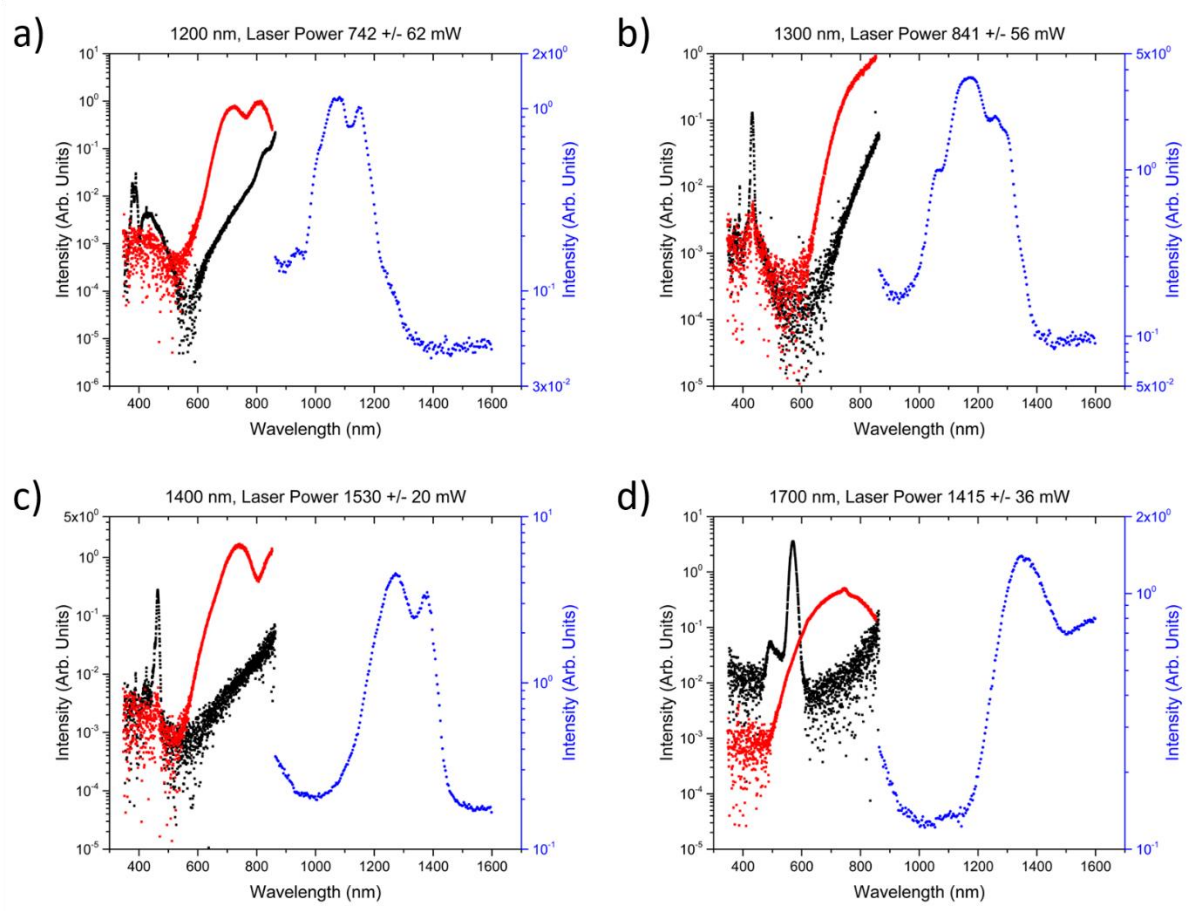

Figure III.3: Four representative spectra at a) 1200 nm, b) 1300 nm, c) 1400 nm, and d) 1700 nm. The visual spectra are shown in black and red while the IR is in blue. The left axis (black) corresponds to visual spectra and the right axis (blue) to NIR spectra. Black and blue data represents spectra take from the center and red from the fringe. The visual fringe and IR center demonstrate spectral broadening and continuum generation. The visual center showcases both continuum generation and harmonic generation.

Table III.1: Summary of Supercontinuum and Harmonic Spectral Data for NIR Pump Laser in Atmospheric Air

Wavelength (nm)	Max Pulse Energy (μJ)	Beam Diameter (mm)	Supercontinuum Range 1 (nm)	Supercontinuum Range 2 (nm)	Predicted 3rd Harmonic (nm)	Observed 3rd Harmonic (nm)
1100	210 ± 30	NM	1030-1130	NO	367	352
1200	740 ± 60	7.5	980-1230	615-850	400	389
1300	840 ± 60	7.6	1015-1355	660-870	433	431
1400	1530 ± 20	6.9	1145-1430	595-860	467	464
1500	1360 ± 60	7.0	1285-1575	NO	500	498
1600	1180 ± 20	6.5	1475-1675	NO	533	530
1600-I	1220 ± 20	7.3	1200-1685	670-870	533	529
1700-I	1420 ± 40	8.7	1220-1720	545-840	567	559
1800-I	1025 ± 6	8.4	1445-1705	655-870	600	604
1900-I	1185 ± 8	9.8	1520-1720	NO	633	635
2000-I	970 ± 7	9.1	1565-1715	NO	667	681
2150-I	885 ± 4	8.3	NO	NO	717	757
2200-I	980 ± 20	8.5	NO	NO	733	734
2300-I	684 ± 8	7.8	NO	NO	767	784
2400-I	47 ± 4	NM	NO	NO	800	813

Wavelengths followed by "-I" were from the Idler beam. Acronyms: Not Measurable (NM), Not Observed (NO)

Table III.1 summarizes the results of our spectral data collection for the maximum pulse energy used at each wavelength. We compare and report the pulse

energy, beam diameter, supercontinuum ranges, as well as predicted and observed 3rd harmonic generation. Our predicted values for the 3rd harmonic were within 6% of the measured values. We did not record the incident beam diameters for the radiation at wavelengths of 1100 and 2400 nm. The pulse energy at those wavelengths were not high enough for proper measurement with the camera.

After completing spectral data collection, we measured pulse energies using the setup in Fig. III.1(b) with and without the 1000 nm long-pass filter. The two long-pass filter power measurements were combined with the spectrophotometer absorption measurement of the filter to act as a calibration tool for the final power data. The final result of this calibration for both the positive 200 and 100 mm focal length lenses is shown in Figure III.4. The data show that for both lens configurations at 1300 and 1400 nm, energy measured in the visible is greater than a micro-Joule. At 1500 nm, the filament generated significant visible light when collected with the positive 100 mm focal length lens, whereas at 1600 nm the positive 200 mm focal length lens gave significant visible generation. Current MPE standards would list those wavelengths as having generated an eye hazard given pulse energy and beam radius. An issue for both lenses was that they were unable to capture the entire filament generated supercontinuum light. The positive 200 mm focal length lens was more limited than the positive 100 mm focal length lens. It could only capture the center region, thus biasing the results and reporting lower visible pulse energies.

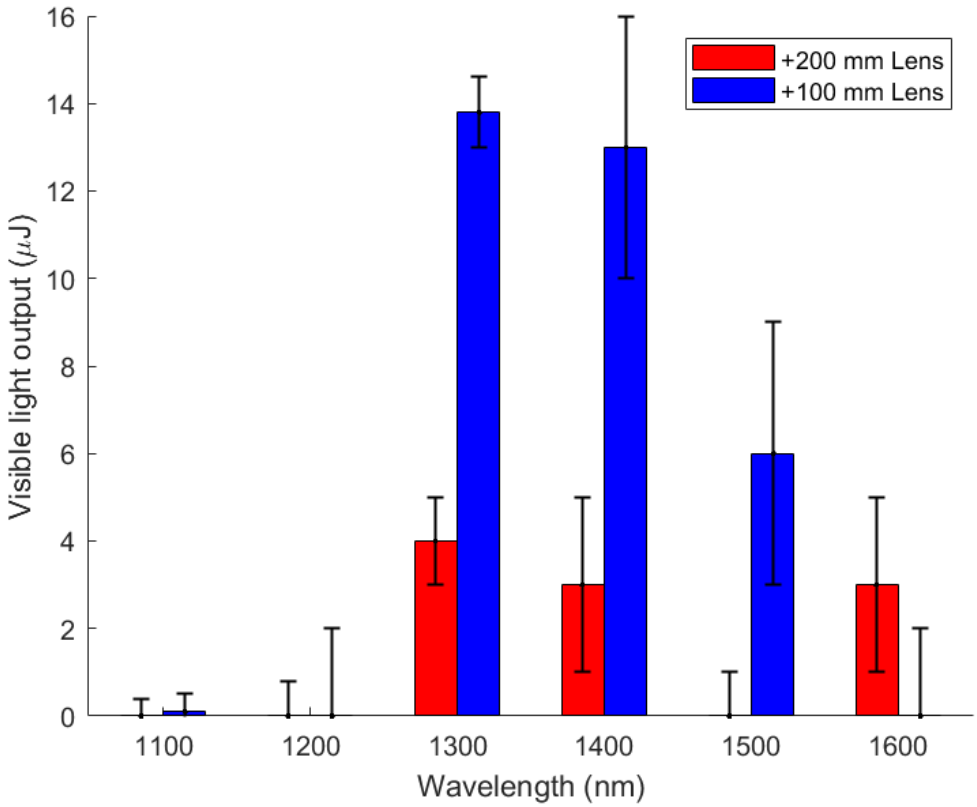

Figure III.4: Pulse energies of visible light (sub 1000 nm) from filament after filtering out infrared as collected by a power meter. The energies measured are collected using the maximum input pulse energies recorded in Table 3.1. The MPE exposure thresholds for visible light on the retina were surpassed by both lenses for 1300 and 1400 nm light. For 1500 and 1600 nm light, the MPE threshold was surpassed for one lens but not both.

3.4 Conclusions and Further Work

We demonstrated that supercontinuum and 3rd harmonic generated light from laser filamentation using wavelengths from 1100 to 2400 nm. The generation of continuum and harmonic light in the visible light spectrum were cause for concern when comparing results of pulse energy to ANSI standards. The NIR supercontinuum and harmonics we generated when using laser wavelengths above 2000 nm, could potentially be a problem itself for eye safety. Improvements could be made in the collection of the light spectra. A significant amount of supercontinuum light was not collected in either the spectral or power measurements and may have demonstrated other wavelengths to pass MPE levels set by ANSI.

CHAPTER IV

NSR RAMAN SPECTROSCOPY

4.1 Background and Motivation

Raman spectroscopy is widely used for chemical imaging and sensing. Ultimately, the ability to provide quantitative information depends on the best attainable signal-to-noise ratio. In this brief report, a method to assess the quality of a Raman spectrometer, which utilizes the concept of Allan variance, is proposed and experimentally implemented to compare two different optical setups. Using the same material, mineral oil, as a study sample, the signal-to-noise ratio was evaluated as a function of the acquisition time leading to essential information on the downsides of a particular system performance. The proposed routine for characterizing Raman spectrometers provides an unbiased methodology to evaluate and to improve system performance.

Over the past decades, Raman spectroscopy has emerged as a powerful and indispensable tool for scientific and industrial applications [61]. As a result, the number of Raman spectroscopy instruments increased dramatically making it often hard to evaluate those and to choose one for a specific influential application, such as bacteria identification [62], forensic studies [63] and/or remote sensing [64]. A growing number of emerging spectroscopic techniques [61], such as nonlinear Raman spectroscopy based on coherent anti-Stokes Raman scattering, also often make it difficult to directly compare different spectroscopic methods [65-69]. In the same time, chemometrics

methods to retrieve structural and chemical information became more sophisticated; however, their accuracy is always limited by instrument performance [70].

This motivated us to search for an unbiased method to evaluate Raman spectroscopy instruments in order to understand their limits and design better instruments for specific applications. In the field of precision measurements, the Allan variance is an established method to characterize the instrument. It has been widely used since its first introduction in 1993 to infrared absorption spectroscopy [71]. Allan variance has been utilized in tunable diode-laser absorption spectroscopy (TDLAS) for the detection of atmospheric gases. Werle, et al [71] calculate the Allan variance for their TDLAS system to determine the detection limit of NO2 by locking the laser to an absorption line. The minimum of Allan plot corresponds to the optimal amount of averaging for the system. Simultaneously showing the length of time the system will remain stable. Similarly Skrinsky, et al [72] performed Allan variance stability experiments looking at various stable and unstable trace gas molecules. Specifically, an infrared diode-laser and CO2 laser were employed for infrared absorption and photo-acoustic spectroscopy.

Bowling, et al [73] found the ratio of atmospheric carbon dioxide isotopes with a TDL. The calculated Allan variance defined the parameters for optimal system operation that would return the minimum error in measured molar isotope amounts. Joly, et al [74] calculated the Allan variance to determine the stability of their near-infrared sensor device for in-situ atmospheric CO2 detection. Tuzson, et al [75] evaluated a quantum cascade laser based spectrometer to find the concentration of carbon dioxide

isotopologues. The use of the Allan variance calculation gave a stability measurement that produced in-situ measurements that when compared with a mass spectrometer agreed within 0.028%. Griffith, et al [76] utilized the Allan variance for their Fourier transform infrared (FTIR) spectrometer, which was designed for simultaneous and continuous detection of atmospheric carbon monoxide, carbon dioxide, methane, and nitrous oxide in-situ. Kasyutich, et al [77] assessed the performance of a continuous wave (cw) external-cavity quantum cascade laser (EC-QCL) for infrared absorption spectroscopy of nitrous oxide (NO). The peak locations and areas were analyzed using the Allan variance to determine stability of the system.

Despite all of this work, no attempt has been made, to the best of our knowledge, to utilize the same approach to Raman spectroscopy. We have taken inspiration from the Allan variance concept to develop a simple method of assessing the performance of Raman spectrometers.

4.1.1 Introduction to the Allan Variance

The Allan variance is a means of analyzing and understanding noise and drift in a system and how it converges as a function of time. In its simplest form, the Allan variance is the variance of a time averaged measurable quantity such as a Raman peak's intensity. It is found by taking data that is measured over time. The data is then sectioned by specific intervals of time and averaged over those intervals or bins. Those bin lengths begin at the smallest possible interval and grow until there are at least two bins or averaged signals. For bins of the same length, the squared difference of sequential averages are found, totaled and then divided by the total number of bins. The resulting

value is known as the Allan variance. Werle, et al [71] derived a rigorous form of the Allan variance.

$$I_{\mathrm{avg},s}(k) = \frac{1}{k}\sum_{l=1}^{k} I_{(s-1)k+l}, \qquad \text{(Eq. 4.1)}$$

$$\langle \sigma^2_{I_{\mathrm{avg}}}(k) \rangle_t = \frac{1}{2(m-1)}\sum_{s=1}^{m-1}\left(I_{\mathrm{avg},s+1}(k) - I_{\mathrm{avg},s}(k)\right)^2. \qquad \text{(Eq. 4.2)}$$

In these equations, I is the signal intensity, I_{avg} is averaged signal intensity, k indicates the total number of elements in a given bin to be averaged with l being the index of each of these elements, m is the total number of bins for the averaged data where s is the index for each bin, and $\sigma^2_{I_{avg}}$ is the Allan variance which is a function of the number of averaged elements. If the total number of signal data points is given by N, the minimum signal acquisition time by τ_0, and the bin time length by τ, then $N = km$ and $\tau = k\tau_0$. The ultimate goal in utilizing the Allan variance is to find its minimum value. This point is where the noise of the system has been minimized and how long before drift becomes an issue. This value corresponds to the optimal bin size, signal averaging time or signal acquisition time. For m bins of k averaged signals, the Allan variance calculates the squared deviation among averaged portions of the observed signal.

In this report, we utilized the above-described concept to evaluate the efficiency of Raman signal collection. We selected a commonly available sample with strong Raman response, mineral oil, to compare two distinct Raman spectrometers. The characteristic Raman peaks of mineral oil were used to calculate the noise-to-signal ratio (NSR) for these peaks and observe the effect of increased averaging time. Raman spectra

signal and noise over long collection times were analyzed using the Allan variance calculation. Allan variance results determined optimal averaging times for each Raman spectrometer. The limitations of each system were determined by examining both Allan variance and NSR results.

4.2 Materials and Methods

We employed a commercially available Horiba LabRam HR Evolution Raman microscope and a homebuilt Raman microscope for the two systems. The LabRam microscope had an Andor Newton EMCCD whereas the homebuilt system used a cooled CMOS linear array detector (ASEQ Instruments HR1 CCD). The Horiba system used a Ventus model, 100 mW, 532nm laser from Laser Quantum with an Olympus MPlan-N 10x, 0.25 NA objective. The home built system used a 175 mW, 532 nm laser from Lasermate with an Olympus MPlan-N 20x, 0.40 NA objective. In the Horiba microscope the sample was placed on a microscope slide, whereas in the homebuilt system it was placed in a quartz cuvette. For both systems, we used a backscattering geometry in which light was directed to the sample and the scattered light was collected back using the same microscope objective. Both spectrometers were set for about the same spectral resolution (both had resolutions around 0.03 nm or 1 cm^{-1}), and imaging system was optimized to get the maximum signal.

4.3 Results and Discussion

4.3.1 NSR Calculation

The Raman signal was integrated for 10 seconds for both systems. A running average of the spectra was calculated to observe how the signal changed over increasing time intervals. The averaged signal was then used in the calculation of the NSR. The NSR was found by determining the amplitude of the noise for every acquisition time. The root mean square (RMS) of the noise was calculated and utilized with the averaged signal and peak-to-peak noise to find the NSR with the following formula:

$$NSR = \frac{RMS(Noise)}{Signal\text{-}Noise}, \quad \text{(Eq 4.3)}$$

The NSR was calculated for three of the Raman peaks of mineral oil (1303, 1445, and 2873 cm^{-1}, which are CH_2 in-phase twist, CH_3 asymmetric deformation, and CH_3 symmetric stretching vibration respectively; see, for reference [78]). After determining the noise amplitude, the NSR was calculated. The NSR was then plotted against collection time on a log-log scale.

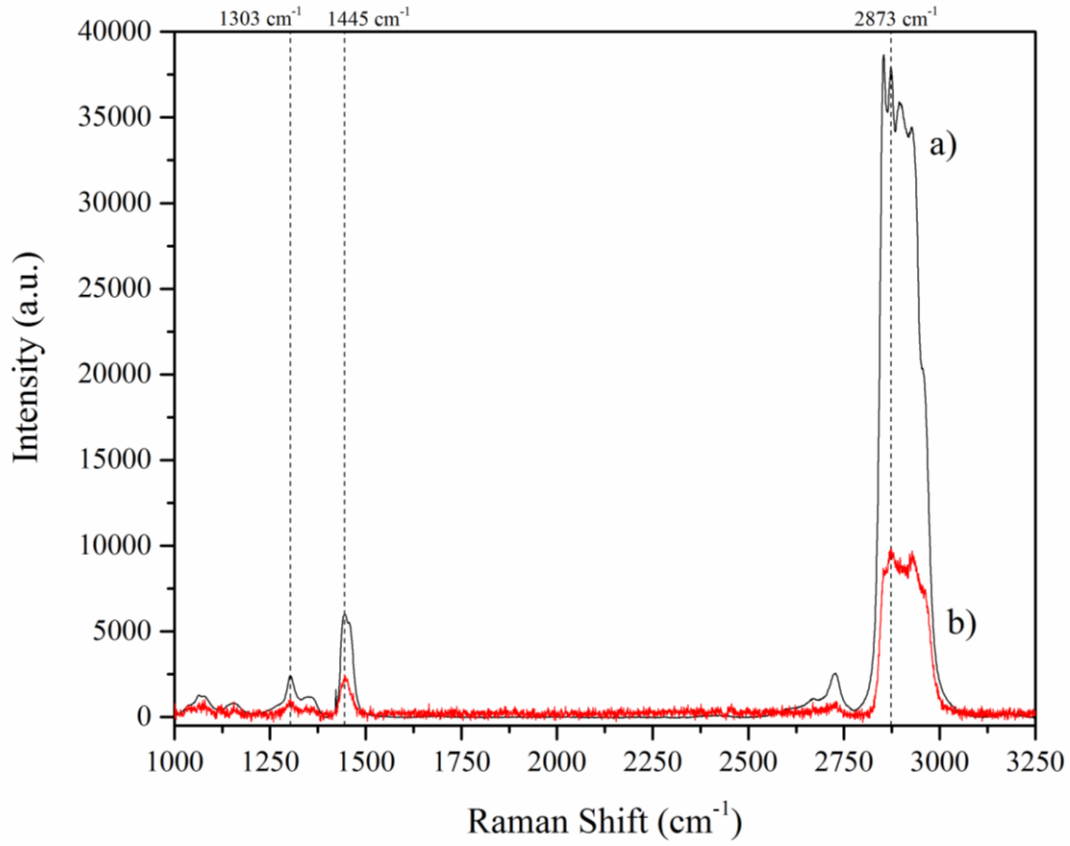

Figure IV.1: a) Raman spectrum of mineral oil collected a) with a Raman microscope (LabRAM, Horiba, Inc.) and b) with ASEQ spectrometer (data scaled by factor of 10 for viewing purposes). Both spectra were collected with 10s integration times.

Figure IV.1 shows Raman spectra from two systems collected over 10 s. Clearly, a home-built spectrometer shows similar Raman features, but many of the smaller peaks are difficult to see above the noise level. This is not surprising considering a high quality grade low-noise CCD in a commercial system. However, is it possible to compensate for the noise using sufficient number of averaging cycles?

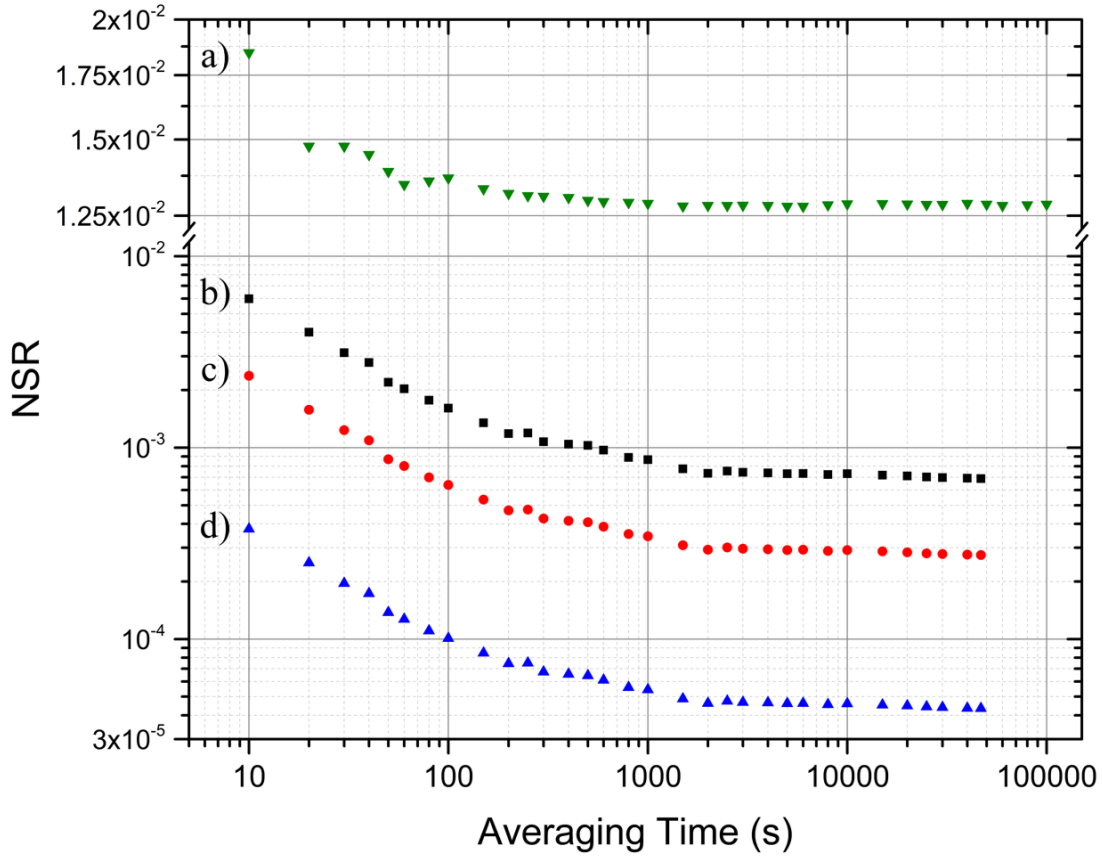

Figure IV.2: Noise-to-Signal Ratios for both the Raman microscope (LabRAM, Horiba, Inc.) and the home-build Raman microscope based on the ASEQ spectrometer. a) The peak intensity of the 2873 cm^{-1} Raman line collected with the home-built Raman spectrometer. b), c), and d) The peak intensities of the 1303, 1445, and 2873 cm^{-1} Raman lines collected with the Raman microscope (Labram, Horiba, Inc.).

The NSR curves for each peak show asymptotic approach to some minimum value as seen in Figure IV.2. The Horiba system approaches a minimum NSR for each peak that is roughly 3 orders of magnitude smaller than that of the ASEQ spectrometer. Another point of note is how rapidly each approaches their asymptote. After 800-s the NSR for the homebuilt system based on the ASEQ spectrometer stabilized and

additional averaging didn't impact the quality of the signal. Similarly, the NSR for the Horiba system also approached its steady value after 2000-s of averaging, and additional averaging became almost unnecessary. The NSR curves for different Raman lines are following the same trend, meaning that those NSR curves represent the properties of the detection system rather than the sample itself.

There are several outcomes of such system analysis. While it is obvious that a higher grade, lower noise CCD detector is beneficial for high SNR (low NSR), a simple increase of the data acquisition time has its own limit. In our particular example, we were not able to improve our SNR above 2.3×10^4 for the strongest line of Raman signal, which would be insufficient, for example, for accurate Raman optical activity measurements [79]. Correcting for an individual pixel response might provide some improvement; however, we were not able to achieve any substantial enhancement of either system performance, when we employed an incandescent white-light source for such calibration. We also observed that different systems take different time to reach their peak value of SNR, and this optimal time should be taken into account when performing high SNR Raman measurements. In the same time, in our prior experiments using true photon-counting detection [78], we witnessed a continuous SNR improvement without any signs of degradation up to the maximum 10,000 s acquisition time. Our NSR analysis let us conclude that when comparing the 2873 cm^{-1} line between the two systems the Horiba system would provide two order of magnitude lower NSR than the ASEQ system. We can still learn far more about our systems by understanding the dominant underlying noise processes, merely by applying the Allan variance method.

4.3.2 Allan Variance Calculation

The analytic Allan variance method is needed to determine the optimal averaging time for each system. To that end, we calculate the Allan variance of the peak value fluctuations and peak-to-peak noise as averaging time increases. The calculation is performed using the method described in equations 4.1 and 4.2 as defined by Werle, et al [71]. Figures IV.3 and IV.4 depict the Allan variance for the Raman peak value and peak-to-peak noise for the ASEQ spectrometer, whereas Figures IV.5 and IV.6 show the same calculation for the Horiba spectrometer. The Allan plots reveal distinct differences between the spectrometers.

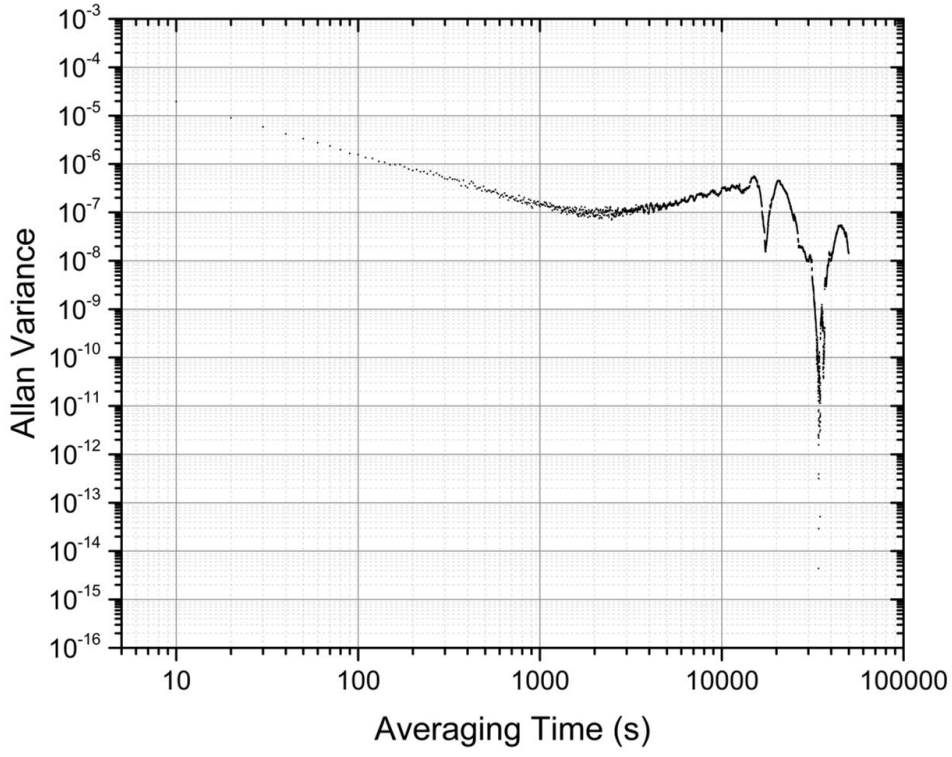

Figure IV.3: Allan variance for the 2873 cm^{-1} Raman peak with the ASEQ spectrometer. An initial minimum in the Allan variance is seen at ~2400-s. The minima observed after 10000-s are found to be caused by fluctuations in the temperature of the spectrometer.

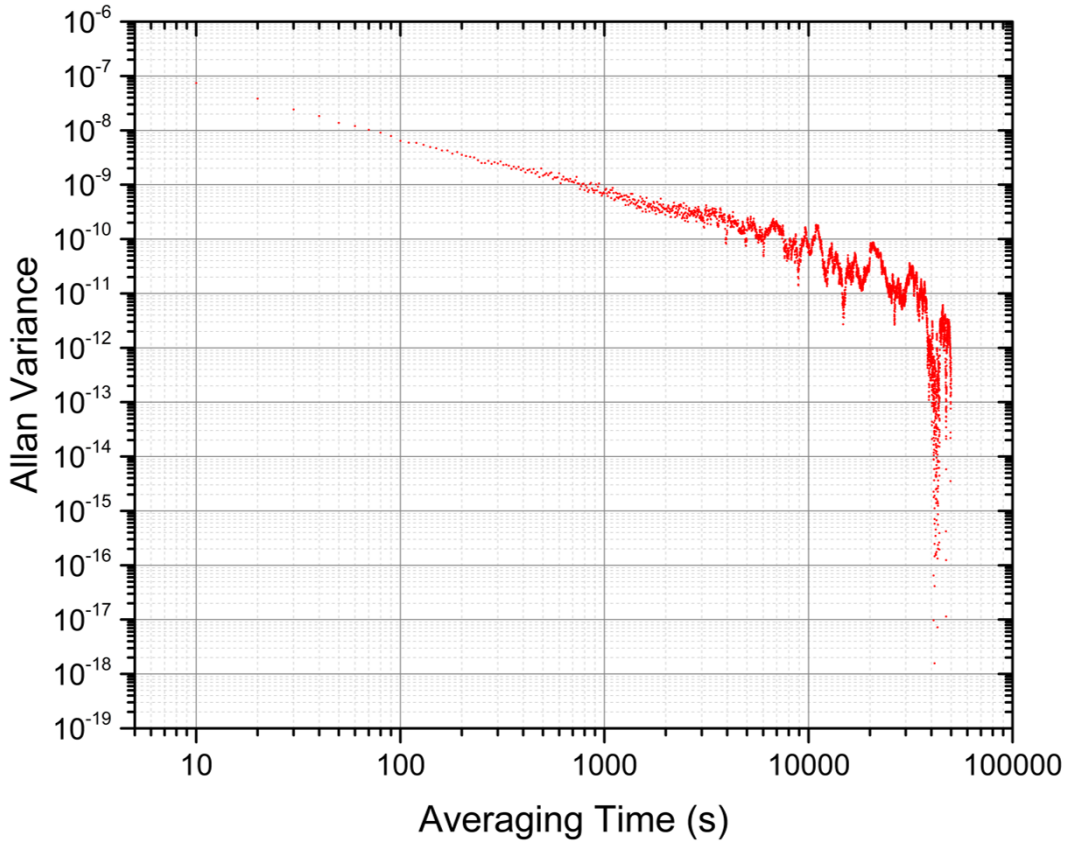

Figure IV.4: Allan variance of peak-to-peak noise for the ASEQ spectrometer. The low frequency fluctuations past 10000-s imply the cause is thermal fluctuations in the spectrometer. The peak-to-peak noise is primarily dependent upon the dark current of the spectrometer and therefore the temperature of the spectrometer.

The ASEQ spectrometer's Allan variance for the 2873 cm^{-1} Raman peak and peak-to-peak noise provides information on the optimal averaging time and sources of noise. Figure IV.3 shows the minimum Allan variance occurring at ~2,400-s indicating our optimal averaging time. Analysis of the trend before and after the minimum using linear fitting methods indicates white noise dominating in the time domain up until 2,400-s and drift noise dominates in the long term up until ~15,000-s. After ~15,000-s,

the system begins to show an oscillation in the variance. This oscillation appears at 17,000-s intervals and causes the Allan variance to drop below the first minima at 2,400-s. Figure IV.4 depicts the noise decreasing steadily with increased averaging until approximately 5,000-s, which indicates a white noise dominant regime. After 5,000-s we start to observe some low frequency oscillations around the overall trend along with a large dip around 40,000-s. The large periodic decreases in the Allan variance in both plots indicates that there is a common factor acting on both the noise and signal of the spectra.

The noise background sections of the spectra do not have Raman shifted photons from the laser acting on them. The noise in these areas of the spectra are determined primarily by the presence of dark currents inherent within all photosensitive devices. Cooling a photosensitive device and keeping it at a constant temperature manages dark current. The more that a CCD can be cooled, the larger reduction in background noise in the resulting spectra. The temperature variation over time in either CCD will cause variations in the spectra, which would be observable in the Allan variance of the peak magnitude. A raised or decreased background (caused by either worse or better cooling respectively) can either decrease or increase the relative magnitude of the signal when compared to background. A reduction in background due to suppressed dark currents would be a factor in causing decreased variation in both signal and noise. We conclude therefore that the periodic decreases seen in the Allan variance in the ASEQ spectrometer is due to long term temperature drift in the CCD.

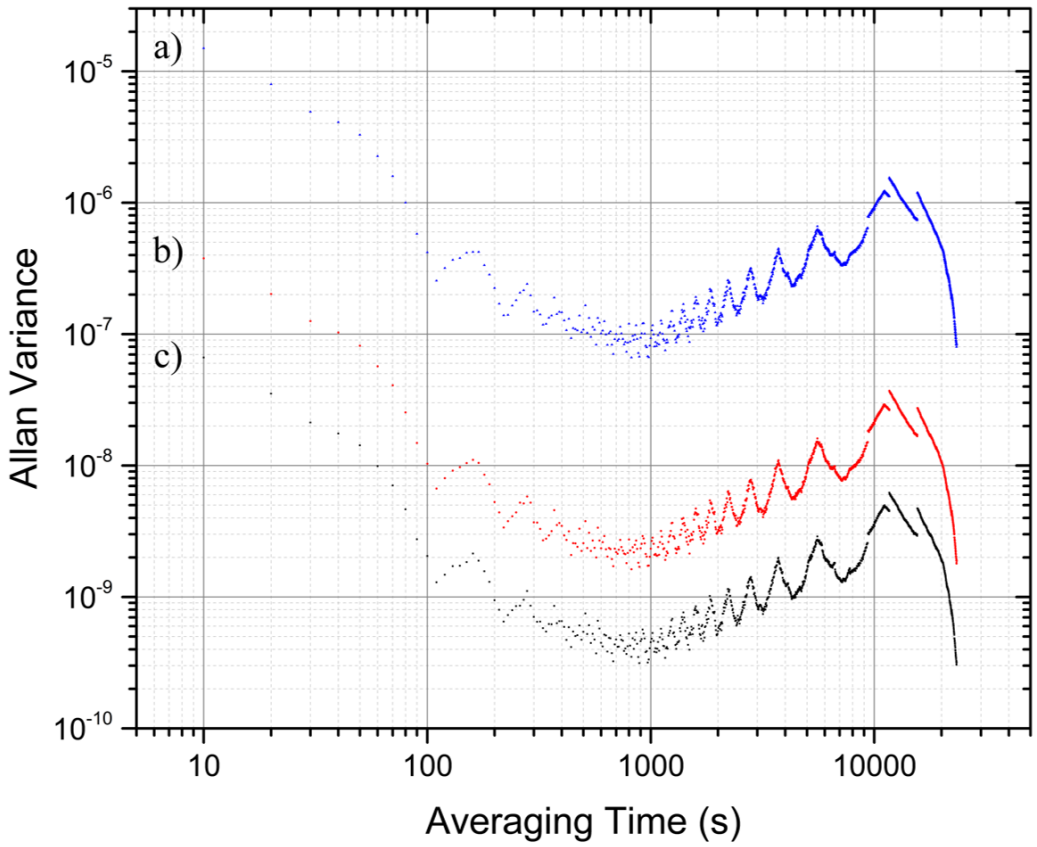

Figure IV.5: Allan Variance for the a) 2873 cm^{-1}, b) 1445 cm^{-1}, and c) 1303 cm^{-1} Raman peaks with the Horiba spectrometer. An Allan variance minimum is seen at ~900-s. A low frequency oscillation occurs throughout the Allan variance curve. Inspection determined the cause to be shifts in the power output of the 532 nm laser. The decrease in the Allan variance past 10000-s is again determined to be caused by temperature shifts in the spectrometer.

The Horiba system shows a very different Allan plot, however. In Figure IV.5, the Allan variance exhibits a low frequency oscillatory behavior from ~100-s to ~10,000-s. This was found to be caused by instability in the Ventus laser power. A minima occurs at ~900-s, but at averaging times above 15,000-s the system is trending towards a lower Allan variance. Before 800-s, the system exhibits dominant white noise,

while after 900-s and before 15,000-s drift noise remains the dominant trend. After 15,000-s the Allan variance of the peak signal decreases rapidly, similarly to the ASEQ spectrometer results in figure IV.3, which we attribute to temperature drift in the CCD. Figure IV.6 displays the Allan variance of the noise for the Horiba system. The Horiba spectrometer's peak-to-peak noise Allan variance plot demonstrates dominant white noise until a minima is reached around 1,600-s. Drift noise begins to dominate after the minima and, as with the ASEQ system, a low frequency oscillation occurs. This oscillation around the overall trend appears to start after 3,000-s of averaging time. As with the ASEQ system, the longer term oscillations are understood to be related to the temperature of the CCD.

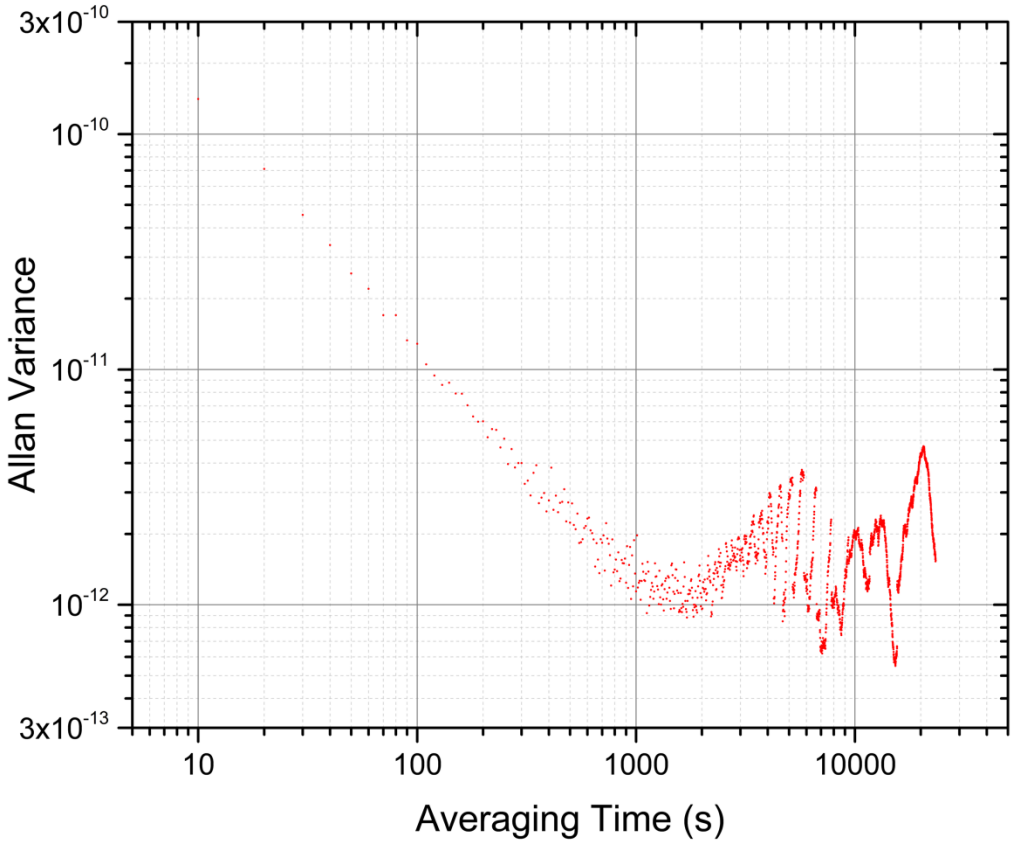

Figure IV.6: Allan variance of peak-to-peak noise for the Horiba spectrometer. An Allan variance minima is reached around 1600-s. The low frequency oscillation is due to temperature changes in the CCD.

Determining the oscillation effect observed in figure IV.5 to be related to laser power instability, which can be seen from 100-s to 10,000-s, required investigating the Raman peak amplitude with respect to time, figure IV.7. The fluctuations of the normalized peak height indicate that the laser power output was hopping around over time. The other possible options don't have enough evidence to be responsible. The sample is fixed in location by a motorized stage so it can't move out of the focal region. While temperature drift occurs in the Andor EMCCD, the frequent fluctuations that

occur throughout data collection would require the temperature to be vastly changing shot to shot. This would necessarily impact the Allan variance of the peak-to-peak noise from beginning to end of averaging time, which does not occur. Evaporation of mineral oil could plausibly cause the sample to move out of the optimal focal region, but that cannot be the case here as we do not see a continuous drop in the signal. A calculation for peak shift over time found no significant drift in the Raman shift, showing that the laser frequency was stable. Therefore, we can only conclude that fluctuating laser power was the source. While we see changing peak amplitudes for the ASEQ spectrometer over time in Figure IV.8, it happens far more infrequently than for the Horiba system and appears to be random. The other difference between the two systems is the peak amplitude variation can be seen as early as the first 100-s in the Horiba system and doesn't appear in the ASEQ system until after 2,400-s have passed. The greater stability of the laser in the ASEQ system would lend itself to having a much longer optimal averaging time.

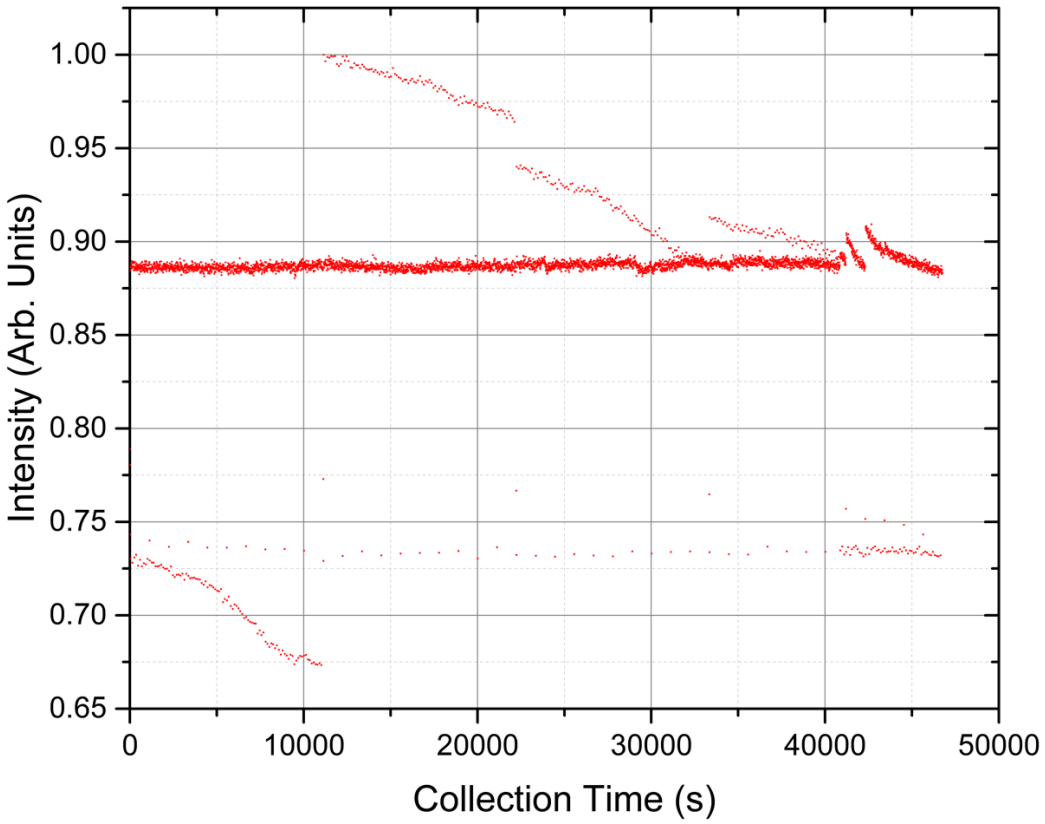

Figure IV.7: 2873 cm^{-1} peak values for Horiba spectrometer. Each data point is an individual 10-s integration time spectra and the time indicates how long after the start of the experiment the data was collected. The data indicates the laser was mode hoping, thereby causing large variations in the power output of the beam. The power output variation caused a variation in the spectral peak intensity.

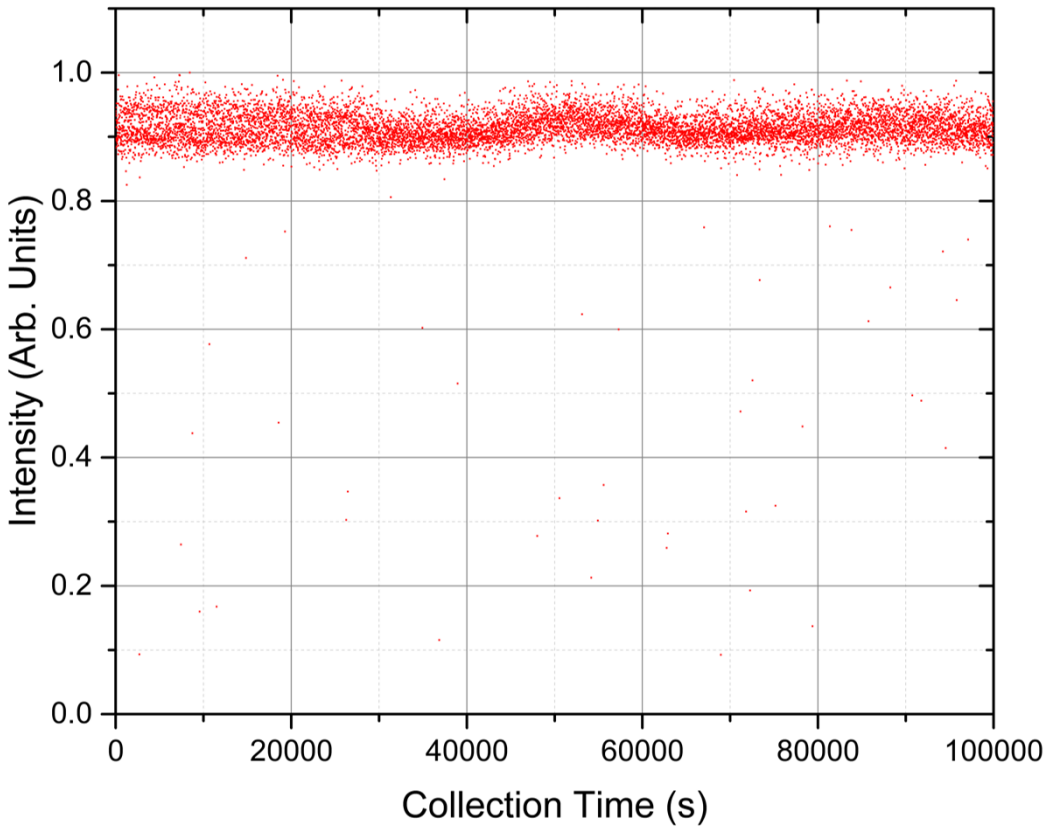

Figure IV.8: 2873 cm^{-1} peak values for ASEQ spectrometer. Each data point is an individual 10-s integration time spectra and the time indicates how long after the start of the experiment the data was collected. When compared to the peak values of the Horiba spectrometer, we find that the laser was far more stable.

The NSR curves earlier show that the Horiba spectrometer approached its minimal value around 2000-s of averaging time, much longer than the optimal averaging time as indicated by the Allan variance of the peak intensity and peak-to-peak noise. Comparing the Allan variance of the 2873 cm^{-1} peak amplitude, Figure IV.5, with that same peak's amplitude over time as shown in Figure IV.7, we can see why the Allan variance gives a shorter optimal averaging time. The fluctuation in laser power means

that longer averaging times will eventually cause a greater variation in Raman peak intensity. The Allan variance calculations for Raman peak intensity and peak-to-peak noise gave us gave us a minimum variance in the peak intensity at ~900-s of averaging time, whereas the peak-to-peak noise minimum variance occurred around 1,600-s of averaging time. Producing the best quality data for the Horiba spectrometer requires compromising between minimizing the noise and peak variance.

The same comparison between the NSR for the ASEQ spectrometer and the Allan variance for the Raman peak intensity shows that while the NSR approached its asymptotic minimum after ~800-s, the Raman peak intensity didn't reach its minimal Allan variance until ~2,400-s. The ASEQ Allan variance for the noise does not reach a similar minimum as does the peak intensity. The running average of the peak-to-peak noise in Figure IV.9 shows that after 2,000-s the background noise has reached an asymptotic value where additional averaging will not be beneficial. Therefore, the ~2,400-s averaging time for the minimal Allan variance of the peak intensity is our optimal averaging time.

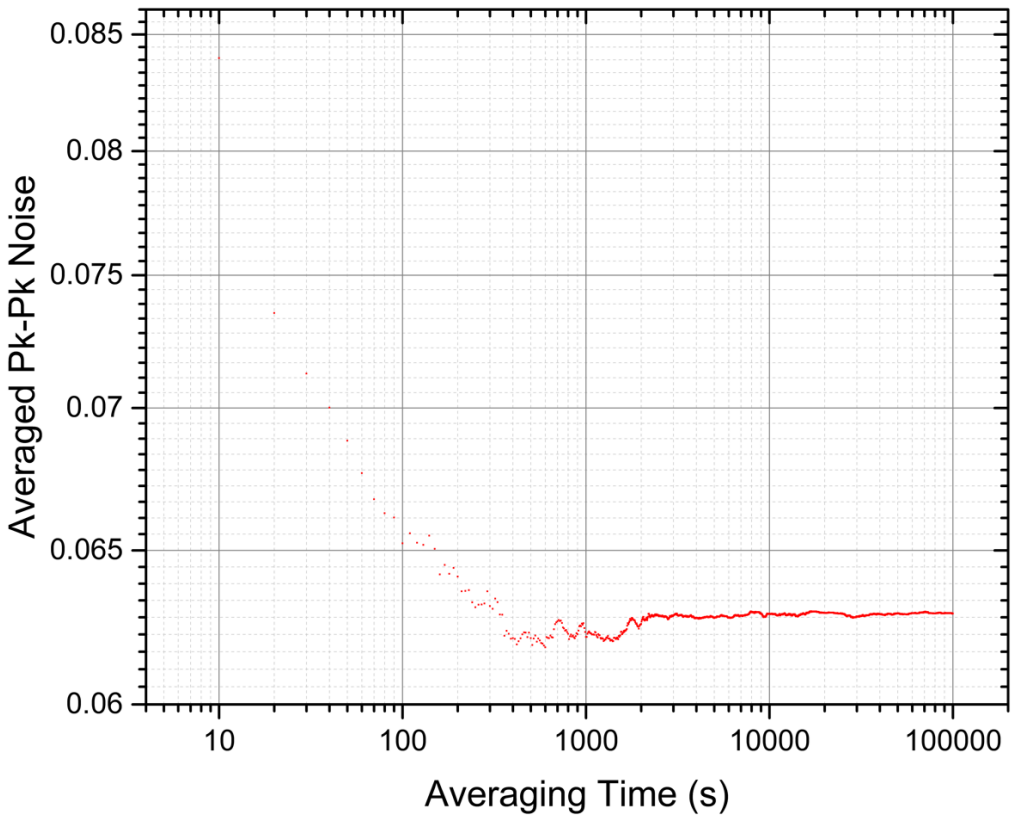

Figure IV.9: Running average of peak-to-peak noise for the ASEQ spectrometer. By inspection, we can determine that after ~2000-s, additional averaging was not decreasing the peak-to-peak noise and therefore not decreasing NSR.

These various noise processes all have an effect on the detection limits of a system. The calculated Allan variance for the noise and by comparison the signal peak give different optimal times for integration. Knowing these optimal times, one can determine a range of averaging amounts that will generate the best quality data. Generally this range should occur where the drift from one noise source doesn't overpower the benefits of reducing white noise in another source. For the two systems we employed, we were able to use the quantitative method of the Allan variance to

evaluate the spectrometers. The Allan variance method showed that the ASEQ system required longer averaging time to reach its optimal NSR when compared to the Horiba spectrometer in a quantitative manner. The work shows that when Allan variance analysis is applied to Raman spectroscopy, we can assess multiple aspects of the system merely by investigating the produced spectra. We were able to conclude, without separate measurement devices or analysis, the stability of the laser and of the CCD. A researcher can apply the Allan variance technique to find the optimal amount of averaging for their systems. Using that they can therefore determine how long it will take their device to reach its minimal NSR.

4.4 Conclusion

SNR optimization is prevalent throughout applied Raman spectroscopy. We believe that the method proposed in this report will allow other research groups to evaluate the performance of their instruments in order to find their limitations and further improve signal collection and data acquisition protocols. Performing analysis for several Raman lines will also help to avoid long-term variations in the sample itself, providing a better reproducibility of Raman measurements.

CHAPTER V

RAMAN SPECTROSCOPY COMPATIBLE PDMS DROPLET MICROFLUIDIC CULTURE AND ANALYSIS PLATFORM TOWARDS ON-CHIP LIPIDOMICS∗

5.1 Background and Motivation

Raman spectroscopy is a useful tool for chemical identification and quantification. A significant benefit of the Raman process to biological organisms is the ability to investigate sensitive cells without the need for chemically tagging the molecules of interest or destroying the cell [29-31]. Biofuels produced by microorganisms, particularly microalgae, have been increasingly studied as a renewable source for dwindling petroleum reserves [80-82]. Understanding how the microalgae produce lipids over time in a variety of conditions would allow for optimal yields helping to push production into commercial production [80,83]. The lipids produced are typically long-chain hydrocarbons and triacylglycerols (TAGs). These lipids provide a strong Raman response and can be uniquely identified due to the unique molecular bonds each one possesses. The correlation between Raman peak intensities and molecules in the focal volume allows for lipid quantification [84-87].

While other methods of lipid analysis exist and can provide similar information, they each have issues which limit their effectiveness when employed. A standard

---

∗ Reproduced by permission of the Royal Society of Chemistry. “Raman spectroscopy compatible PDMS droplet microfluidic culture and analysis platform towards on-chip lipidomics” by Hyun Soo Kim, Sergio Waqued, Dawson T. Nodurft, Timothy P. Devarenne, Vladislav V. Yakovlev, and Arum Han, 2017. Analyst, Vol. 142, p. 1054-1060; doi: 10.1039/c6an02221a. Copyright [2017] The Royal Society of Chemistry.

practice for analyzing lipids in microalgae involves the detection of fluorescent markers with lipophilic fluorescent dyes. Typical dyes are Nile red or BODIPY are convenient and easily applied. The problem these dyes create is that they typically quickly photobleach cells over time and cause cytotoxicity due to chemicals such as dimethyl sulfoxide (DMSO) [88]. Thus only allowing for a single time point measurement of lipid production for an individual cell. Furthermore, these dyes stain all lipids regardless of type and can only provide information about total lipid amount [88].

Traditional methods of culturing and observing microalgae such as open raceway ponds, closed photobioreactors, lab-scale flasks, and multi-well culture plates lack the high-throughput necessary for single-cell resolution and cannot be utilized for large repeated tests. Microfluidic droplet methods address these problems by creating nano- or pico-liter scale water-in-oil droplets, which act as miniature isolated bioreactor or culture vessels [89-92]. These isolated droplets allow for varied culture conditions in parallel all on a single device. Microfluidic devices section small amounts of culture media containing individual or multiple cells with carrier oil into individual droplets. Thorough examination at single-cell resolution is obtained by the ability to individually transport, mix, merge, and split the droplets with extremely high-throughput [89-92]. As a result, microfluidic devices have begun employment in microalgae biofuel production [92-94].

Microfluidic devices encounter their own problems with lipid measurement techniques. While techniques such as NMR [95], mass spectrometry [29], or solvent extraction and chromatography (HPLC or GC) [96] provide excellent detail in quantification and identification of lipids, they cannot be utilized with droplet

microfluidics. These methods require large sample amounts for analysis. Droplet microfluidics by their nature as micro-scale devices handle only extremely small volumes. NMR, mass spectrometry, and HPLC or GC cause the destruction of the cells, preventing multi-time analysis of the same cells.

The benefits of Raman spectroscopy for quantification and identification without cell damage become even more pronounced when combined with microfluidic devices. A major factor in lipid production of microalgae cells is stress induced by the environment it is cultured in. Typical stress occurs during nitrogen deprivation or photo-oxidation [81]. Determining what stress level optimizes lipid production over time requires tracking the same cells over the course of testing. Furthermore, knowledge of each cell strain's lipid production over time could reveal benefits in developing new cell strains from distinct ones [82,97,98]. Tracking lipid production over time in a microfluidic device with Raman spectroscopy allows for *in vivo* rapid quantification and identification at single-cell resolution needed for accurate optimization of culture methods and settings.

There are two intrinsic problems that must be solved for microfluidic Raman spectroscopy to be successful. The first problem involves the material most microfluidic devices are made from. Polydimethylsiloxane (PDMS) has several factors that make it an excellent choice for microfluidic fabrication. PDMS provides the necessary gas permeability for microalgae culturing over the course of days. Optically transparent, PDMS permits photosynthesis and optical monitoring of cells [99]. For those reasons, PDMS is a great choice for microfluidic design and fabrication and cell culturing. The

issue arises from PDMS's strong Raman response [100]. The strong Raman signal from PDMS wouldn't be a problem, were it not for the fact that several of its Raman peaks overlap with Raman peaks important in the identification of lipids. The second problem involves the carrier oil needed for droplet microfluidics. When placed in carrier oil, the Raman signal from lipids can be concealed [101].

A Raman spectroscopy compatible PDMS microfluidic device was fabricated for use in analyzing microalgae lipids. The microfluidic device allowed for on-chip, droplet-based *in vivo* lipid analysis with single-cell resolution. Two strains of microalgae, *Chlamydromonas reinhardtii* (*C. reinhardtii*) and *Botryococcus braunii* (*B. braunii*), were used to analyze the performance of the PDMS device. *C. reinhardtii* cells were placed in 8 different nitrogen concentration culture conditions to analyze lipid accumulation over time.

5.2 Materials and Methods

5.2.1 Raman Spectroscopy

A Horiba LabRam HR Evolution Raman confocal microscope was utilized in the collection of Raman spectra. The LabRam microscope had an Andor Newton EMCCD and we collected all spectra using an Olympus MPlan-N 50x, 0.75 NA objective. The Horiba system used a Ventus model, 100 mW, 532nm laser from Laser Quantum with a spot size of approximately 1.5 µm when focused using the 50x objective. The light was focused onto single cells to collect the Raman spectra. A holographic grating of 1800 lines per millimeter dispersed the collected light onto the Andor EMCCD. While the system offered other wavelengths, 785 and 660 nm, the 532 nm laser was selected for its

higher SNR Raman spectra. The 532 nm laser also provided faster photobleaching of background chlorophyll autofluorescence. The acquisition time was set to 20 seconds and two spectra were collected to average out background noise. The confocal hole was set at two different diameters, 200 µm and 25 µm or 4.6 and 0.58 Airy units respectively, to investigate PDMS background reduction. An Airy unit is a measure of how optimally the diameter of a pinhole is set to match the diameter of the Airy disk. The Airy disk is the inner most circle of light from the diffraction pattern of a point light source. The Airy disk depends on the wavelength of the light, size of the pinhole, and the numerical aperture of the microscope objective. Light was focused on an individual cell and Raman spectra were only recorded if the cell remained in its starting location after all spectra were recorded.

5.2.2 Microfluidic Device

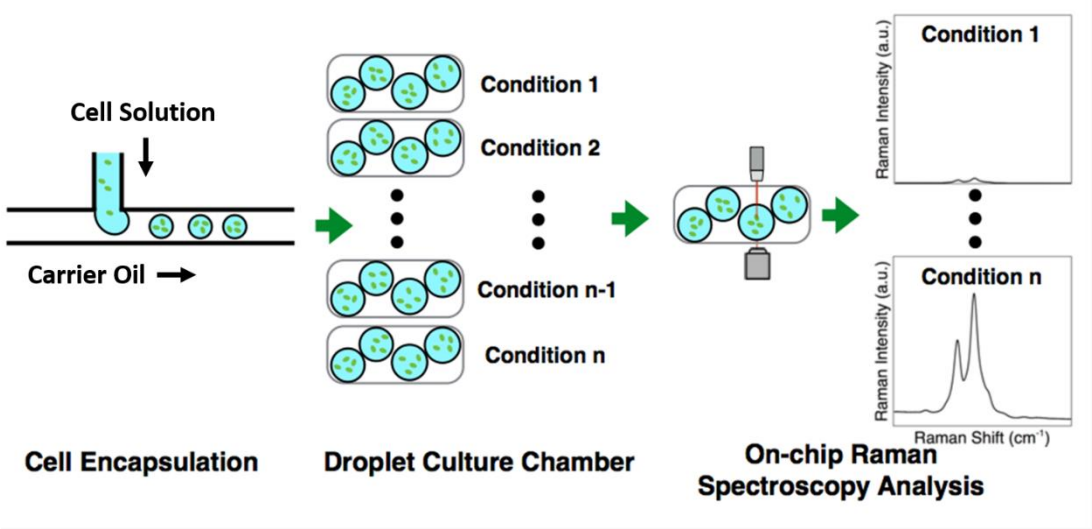

Figure V.1: PDMS microfluidic droplet device. The cell solution enters a T-junction with the carrier oil that sections the cell solution into individual droplets. The droplets are stored in different cell chambers. Each chamber's environmental conditions can be uniquely set to observe changes in lipid production as a result. The cell cultures in the device are then inspected by a confocal Raman microscope.

The microfluidic device was manufactured using PDMS (Sylgard® 184 Dow Corning, Inc., Midland, MI) using the soft-lithography method [91,92]. A T-junction droplet generator with a height of 100 µm was chosen for cell encapsulation [91,92]. The droplet generator involved two crossing channels. The first channel was 200 µm wide and delivered the carrier oil. The second was 160 µm wide and delivered the cell solution. At the T-junction, the cell solution channel came to an end. A droplet was formed by carrier oil encapsulating the cell solution. The droplets proceeded to split into 8 identical droplet culture chambers, each with a volume of 10 µL. An individual chamber can store approximately 1000 droplets. Eight different culture conditions can therefore be set on a single device and tested in parallel. The culture chamber and

droplet generator were bonded to a 24 mm × 60 mm glass cover slide (VWR, West Chester, PA). The cover slide was chosen as the device substrate to reduce PDMS background by allowing the objective to image through the cover slide rather than through the 4mm thick PDMS material [Fig. V.1].

The completed device was treated to increase the hydrophobicity of the channel surface with Aquapel (Pittsburg Glass Works, LLC). The treatment with Aquapel provided consistent droplet generation and minimized device-to-droplet wetting interactions [102]. The Aquapel coating in each channel was dried using nitrogen gas. The channels were then filled with Fluorinert Electronic Fluid FC-40 (3M), which was the carrier oil.

The droplets generated at the T-junction were approximately 250 μm in diameter and contained about 10-15 cells each. The FC-40 carrier oil had a 1% 008-FluoroSurfactant (RAN Biotechnologies) that flowed through the 200 μm channel with a flow rate of 500 μL/h. The cell solution, which flowed through the 160 μm channel, had a flow rate of 300 μL/h. The combination of the flow rates and channel sizes generated the individual droplets. After each culture chamber was completely filled with droplets, the inlet and outlet tubes were clamped to seal the droplets in each chamber. The microfluidic device was maintained in a humidified environment, post droplet encapsulation. The humidity prevented droplet evaporation caused by the gas permeability of the PDMS layer during completion of the experiment.

5.2.3 Microalgae Preparation

The types of microalgae utilized were the *Chlamydomonas* reinhardtii, CC-4333 (cw15 arg707 sta6-1) strain, and the *Botryococcus braunii* race B, Showa (Berkley) strain [103]. *C. reinhardtii* is a unicellular microalgae with a typical cell size of 5-10 µm, whereas *B. braunii* is a colony forming microalgae with a typical cell size of 13 µm × 7-9 µm. *C. reinhardtii* was cultured in a tris-acetate-phosphate (TAP) medium with a 100% nitrogen concentration [104]. The *B. braunii* algae were cultured in Chu-13 [105]. A fluorescent light operating at 13 W illuminated both algae strains. The light provided an irradiance of $80\ \ (\mu\text{mol photons})/(m^2 s)$. The cultures were placed on a 12-hour light-dark cycle for 7 days. After completing this initial period, the cells were placed into the microfluidic devices for Raman analysis of lipid production. The *C. reinhardtii* cells were diluted to a concentration of 1.65×10^6 cells per mL for time-course lipid analysis. The diluted cells were then placed in 8 TAP mediums with different concentrations of nitrogen (0%, 15%, 30%, 45%, 60%, 75%, 90%, and 100%). After the different culture conditions were set, the cells were then added to the microfluidic device.

5.2.4 Tracking Lipid Production

The tracking of lipid production in *C. reinhardtii cells* required selecting a Raman band to act as a reference for comparison across all 8 culture conditions. The 1657 cm^{-1} Raman peak is a C=C stretching mode in microalgae lipids and this peak is known to be specific for fatty acid *cis* C=C bonds [106-109]. In each of the 8 nitrogen culture conditions, the peak intensity was collected from 10 different droplets and subsequently averaged. The process was repeated every 24 hours.

A separate microfluidic device utilized the same culture conditions, but utilized fluorescent tagging of lipids to compare results with the Raman analysis. The fluorescent dye Nile red stained each of the 8 different culture channels with the varying nitrogen culturing conditions. Nile red is a lipophilic fluorescent dye which has seen significant use in staining microalgae lipids [89,92,110-112]. As with the Raman analysis, data was taken every 24 hours. A Zeiss Axio Observer Z1 microscope took images of the chlorophyll autofluorescence and Nile red fluorescence. A Hamamatsu ORCA-Flash2.8 CMOS camera was used with the microscope. The fluorescence was excited by 450 to 490 nm light. Chlorophyll emitted fluorescence above 610 nm, while Nile red emitted from 560 to 600 nm light. Lipid production per unit cell volume was quantified by dividing the Nile red spectra by the chlorophyll autofluorescence. The process was repeated for 5 cells to average the results in each cell culture condition. The results of the Raman spectroscopy and fluorescence dye technique were compared at each time point and culture condition.

5.3 Results and Discussion

5.3.1 Background Reduction of Raman Spectra

The strong PDMS background was the first issue that needed to be addressed before lipid production could be tracked over time. The first step in reducing the background came by comparing Raman spectra collected from *B. braunii* microalgae inside the PDMS microfluidic device in both a standard upright and inverted orientation. In the upright orientation the microscope objective focuses through the PDMS onto the cell. The inverted orientation has the objective focus through the cover slide substrate

onto the cell. The inverted orientation produced significant reduction in PDMS Raman scattered light, as has been shown in previous studies [113,114]. The inverted orientation allowed for accurate *in vivo* detection and recording of lipid spectra [Fig V.2].

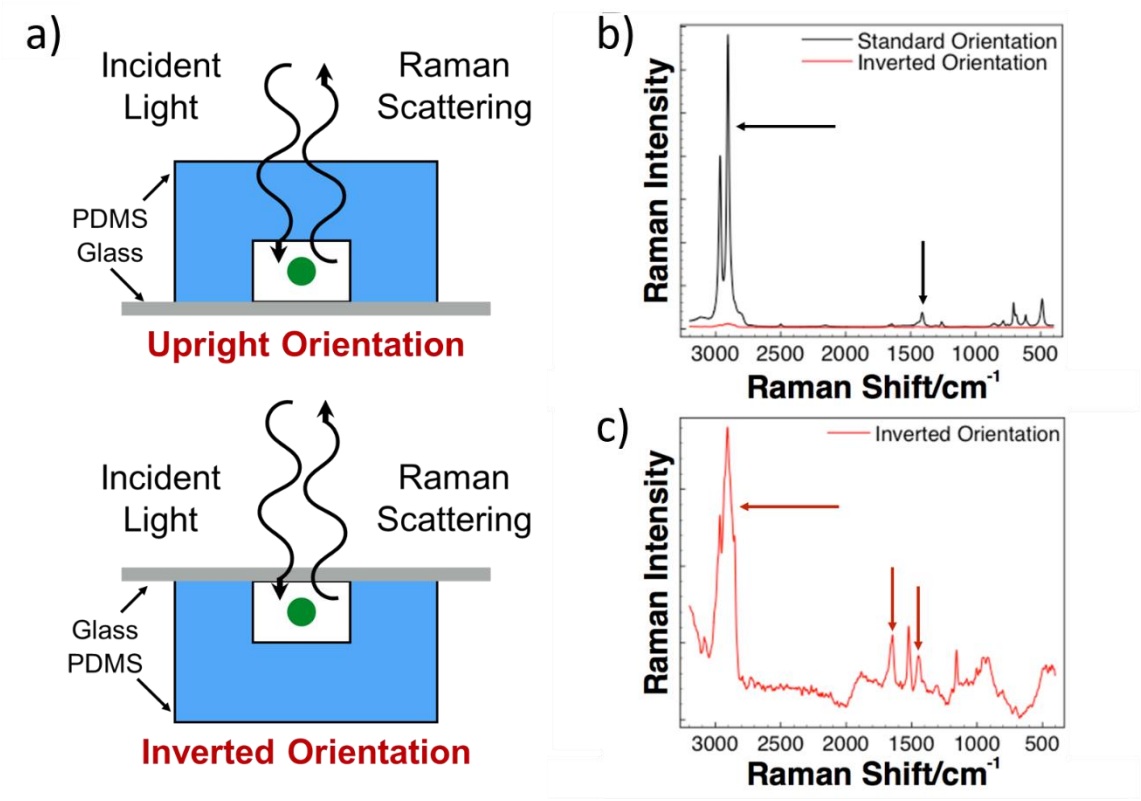

Figure V.2: PDMS background reduction by device orientation. a) Comparison of device in upright and inverted orientations. b) Comparison of Raman shift of *B. braunii* from upright (black) and inverted (red) orientation. c) Rescaled view of Raman shift in inverted orientation in b) showing significant reduction in PDMS Raman peak (black arrows) background while showing lipid peaks (red arrows).

The effects of the confocal hole diameter on PDMS background was investigated using the inverted device containing *B. braunii*. Reduction in the size of the confocal hole removes unwanted background signal from materials that are not in the focal region. Confocal hole sizes of 200 and 25 µm (4.6 and 0.58 Airy units respectively) were chosen. While the Raman peaks of 1440 cm^{-1} and 1657 cm^{-1} (CH_2 bending and C=C stretching, respectively) were visible, the 200 µm confocal hole contained significant PDMS Raman spectral background [107]. Reduction of the confocal hole to 25 µm caused a dramatic reduction in PDMS background [Fig V.3]

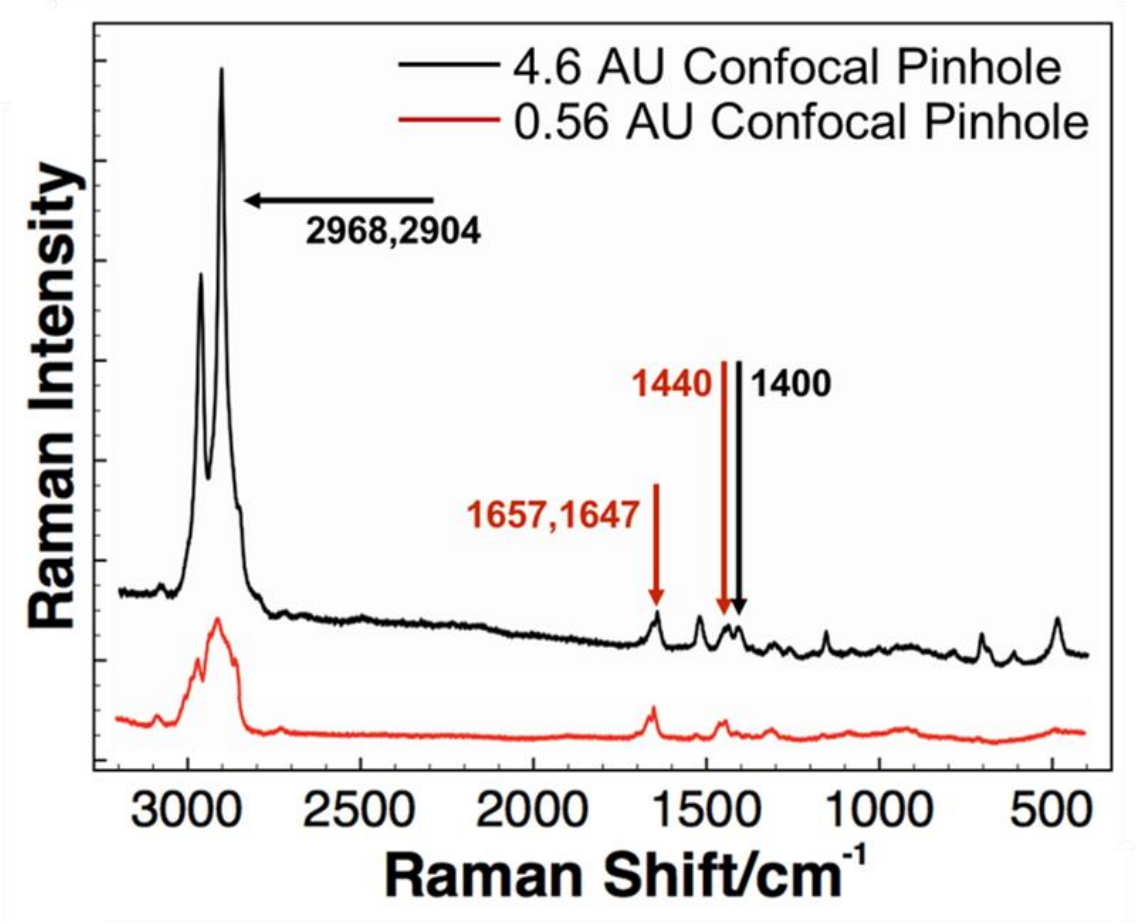

Figure V.3: Comparison PDMS background in Raman spectra of *B. braunii* lipids with 4.6 AU confocal pinhole to 0.56 AU confocal pinhole. Lipid peaks are indicated with red arrows, and PDMS peaks with black arrows.

To demonstrate the effective nature of the PDMS microfluidic device, the Raman spectra of a *B. braunii* cell was taken on a fused silica slide without any microfluidic structure. The microfluidic device can only be successful if it can limit the PDMS background and provide a Raman spectra with similar quality to that of a free floating cell. The droplet encapsulating the cells of *B. braunii* that were placed on the fused silica slide was covered by a cover slip. The result was that the *B. braunii* algae colony was

squeezed between the cover slip and fused silica slide, thus forcing the colony into a planar-like structure.

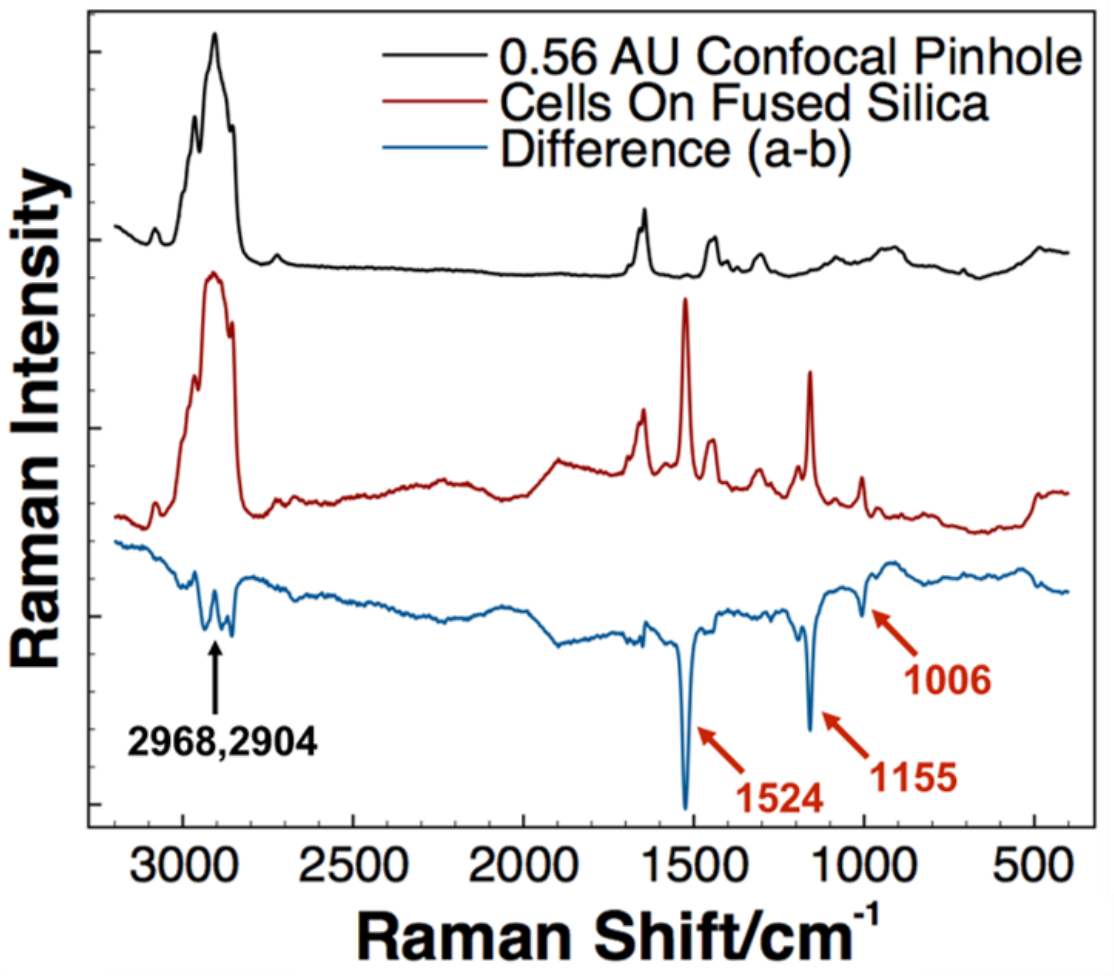

Figure V.4: Raman spectra of *B. braunii* lipids from 0.56 AU confocal pinhole (black), on a fused silica substrate (red), and difference between the two (blue).

The comparison of the two spectra is shown in figure V.4. The spectrum of the inverted microfluidic device was subtracted by the spectrum of the fused silica slide with the difference shown. A couple of major differences become apparent in the subtracted spectrum. The first difference comes from a weak PDMS signal at 2968 cm^{-1} and 2904 cm^{-1}, which is not unexpected given PDMS only resides in the microfluidic device. The second major difference comes from the Raman peaks at 1524 cm^{-1}, 1155 cm^{-1}, and 1006 cm^{-1}. These three peaks correspond to the carotenoids in *B. braunii* [107,109]. These peaks are pronounced in the fused silica slide and not the microfluidic device, because the cover slip and glass slide squeezed the microalgae colony into a planar-like structure. Thus causing the carotenoids to undergo more extensive inspection via the Raman spectroscopy technique [92]. Comparing the two spectra makes it clear that lipid spectra for the on-chip cells can be obtained with negligible impact from background Raman signal from the PDMS device itself and gives similar results to a traditional detection setup.

5.3.2 Droplet Microfluidics vs. Free-Floating Microfluidics

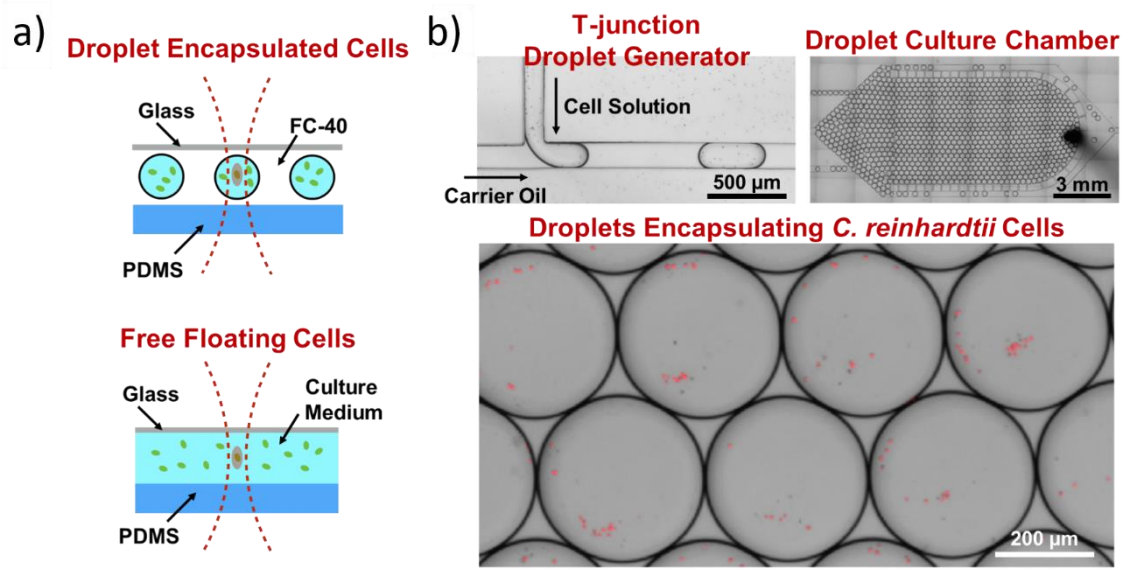

Figure V.5: a) Diagram comparing droplet encapsulated cells vs. free-floating *C. reinhardtii* cells. b) Microscopic images of droplet generation, culture chamber filled with droplets, and enlarged view of cells within droplets.

The microfluidic device was tested using both droplet encapsulated and free-floating non-motile *C. reinhardtii* cells [Fig. V.5]. The subject of concern was whether Raman spectroscopy was compatible with on-chip lipid analysis of droplet encapsulated microalgae cells. Additionally the droplet and free-floating conditions each had two different nitrogen concentrations (0% and 100%) to determine whether the carrier oil FC-40 introduced any background peaks that would interfere with lipid Raman spectra. The Raman spectra of the carrier oil with and without FluoroSurfactant were collected and compared to the Raman spectra of microalgae cells [Fig V.6]. After collection, no additional peaks were observed due to the carrier oil in the spectra of the lipids.

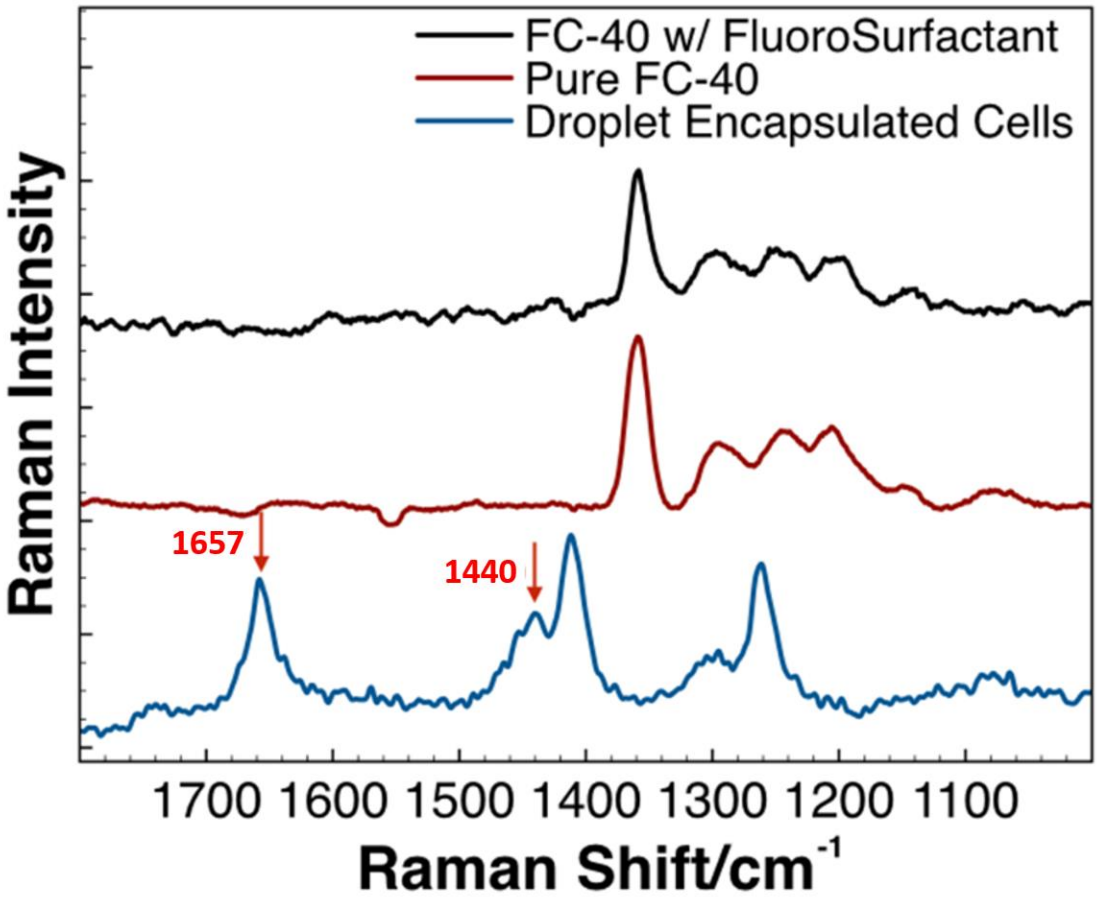

Figure V.6: Spectra of FC-40 carrier oil with (black) and without FluoroSurfactant (red). Two are compared to Raman spectra of *C. reinhardtii* cell. No peaks were observed in the carrier oil Raman spectra that would interfere with the critical lipid peaks.

Comparison of spectra for cells accumulating lipids in a nitrogen deprived environment (0%) and cells not accumulating lipids in a nitrogen rich environment (100%) tells two important details [Fig. V.7]. First, the spectra for both droplet and free-floating cells in a nitrogen rich concentration (100%) were identical. The lack of differences in the spectra of droplet encapsulated and free-floating microalgae cells indicates that droplet based microfluidics are feasible. Second, while differences in the

spectra peak intensities exist in the nitrogen deprived concentration (0%), the spectral structure is the same. Thus indicating that the difference is caused by different intracellular lipid concentrations.

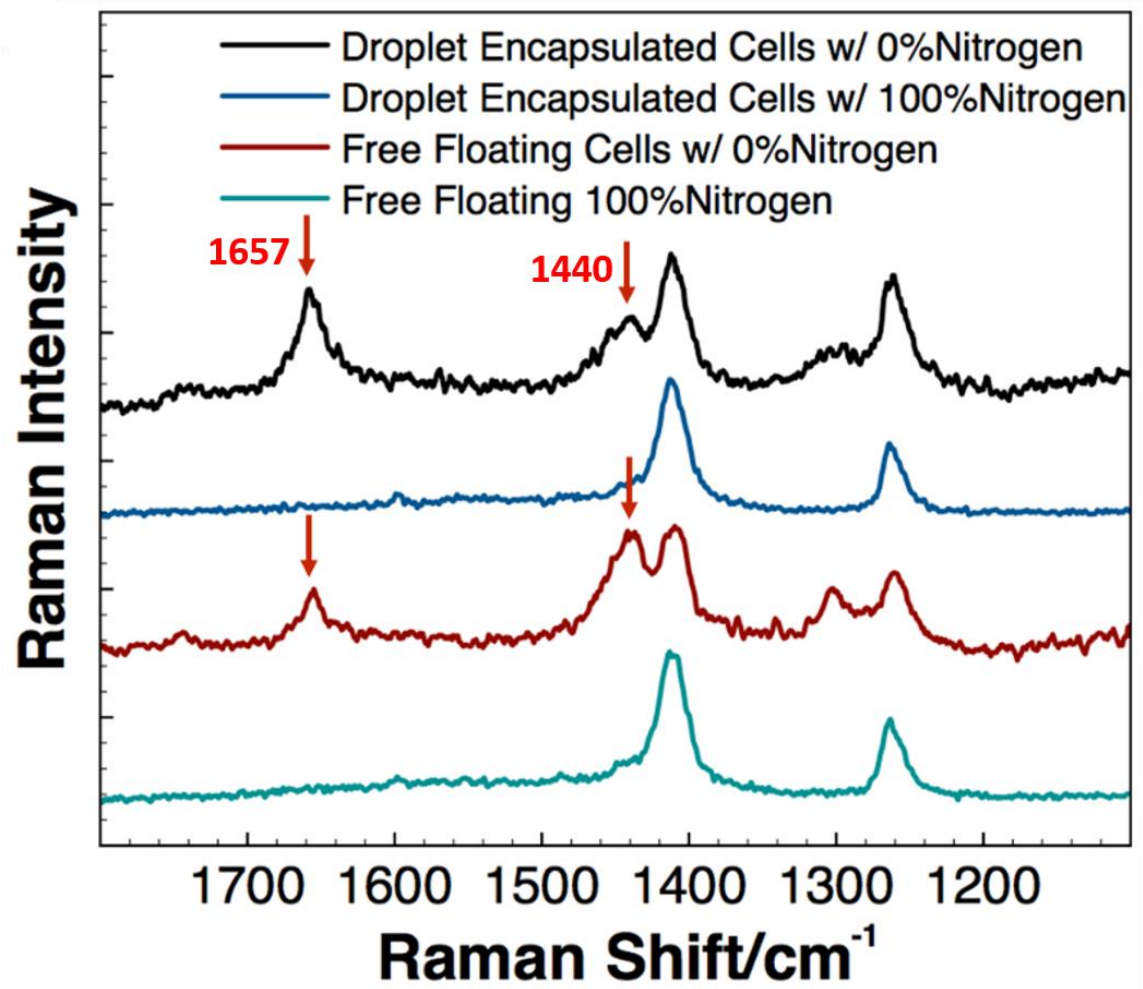

Figure V.7: Comparison of spectra of *C. reinhardtii* cells in droplet and free-floating culture media, both with and without nitrogen deprivation. The nitrogen rich concentrations in both free-floating and encapsulated cells were found to have no lipid production. The similarities for both droplet encapsulated cells and free-floating cells in a nitrogen depleted environment indicates that the use of microfluidic devices will not hinder its use for the application of Raman spectroscopy.

5.3.3 Lipid Production Over Time In 8 Different Culture Conditions

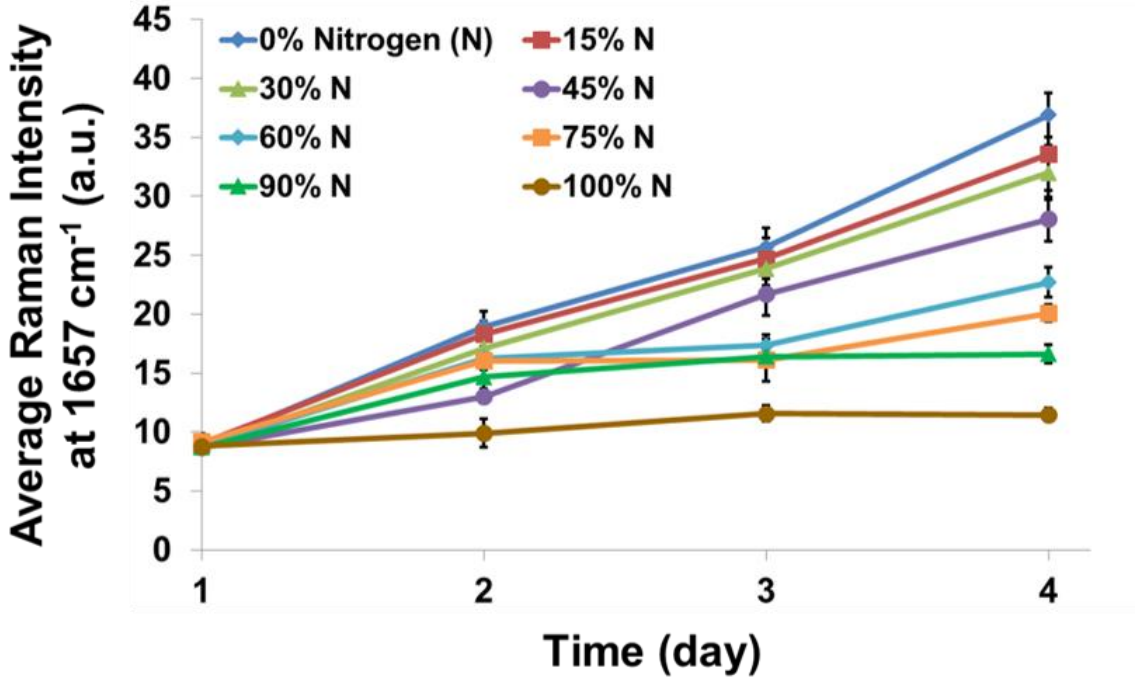

Figure V.8: Time-course Raman spectral analysis of lipid production of *C. reinhardtii* cells in 8 different nitrogen concentrations. As expected, those cells that were cultured in nitrogen depleted chambers produced more lipids than those in a nitrogen rich environment.

Time-course analysis of lipid production was performed using *C. reinhardtii* cells. When *C. reinhardtii* cells are stressed from environmental conditions, they produce lipids and in particular TAGs. One factor that produces stress is nitrogen deprivation and the total lipid produced is dependent on the amount of applied stress [92]. The microfluidic device was prepared with *C. reinhardtii* droplets under 8 different nitrogen concentrations in a TAP medium. The nitrogen concentrations were: 0%, 15%, 30%, 45%, 60%, 75%, 90%, and 100%. The Raman peak correlating to the C=C stretch mode at 1657 cm^{-1} was chosen as the indicator of total lipid production. The 1657 cm^{-1}

Raman peak was used to track the production of lipids over a 4 day period. During the entire 4 day period, the droplets remained stable. No droplets were observed to have evaporated or merged. As a result, Raman spectra were successfully recorded daily over the 4 day period and the same cells were measured each day. As expected from previous work, increased stress from nitrogen deprivation correlated with increased lipid production [Fig V.8].

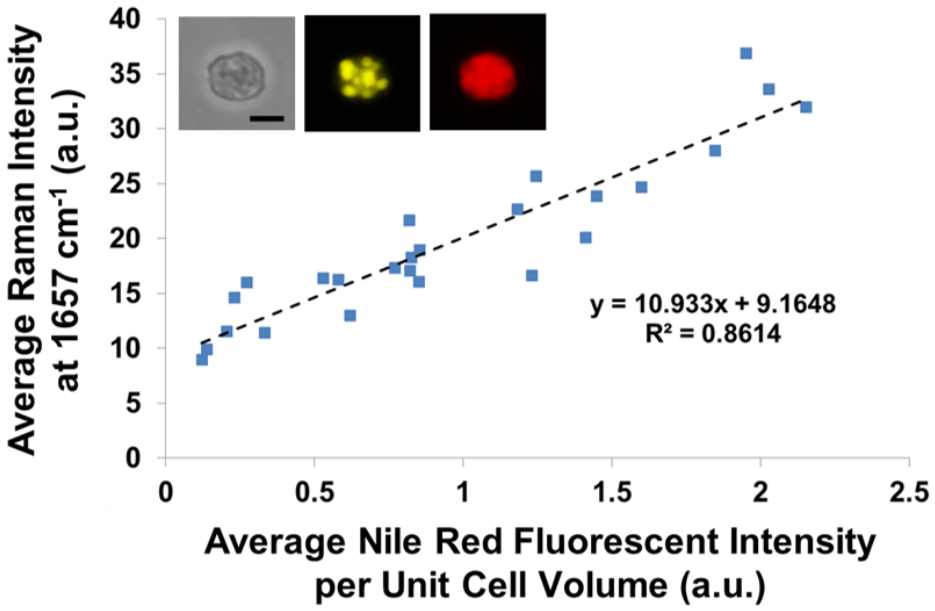

Figure V.9: Correlation between average Raman peak intensity at 1657 cm^{-1} and average Nile red fluorescent intensity per unit cell volume. The high correlation indicates that Raman spectroscopy is a valid alternative to traditional methods like fluorescence staining. The Raman method is not a single time measurement like fluorescence staining can be, allowing for time-course tracking of the same cell's lipid production.

Finally, the results of the time-course Raman spectra of *C. reinhardtii* lipid production were compared with a traditional fluorescent dye measurement method. The lipids from the microalgae were stained using Nile red and fluorescence intensity was quantified. Using the average Raman peak intensity from the 1657 cm^{-1} band and the average Nile red fluorescence intensity per unit cell volume, a strong correlation (R^2 = 0.8614) between the total lipid production during same-time measurements was found [Fig. V.9]. The correlation between lipid quantification methods reinforces the Raman spectral method as a tool to quantify lipid production without need of invasive fluorescent staining.

5.4 Conclusion

The use of Raman spectroscopy as a tool for quantifying and identifying lipid production with PDMS fabricated microfluidic devices has been demonstrated. PDMS background was successfully minimized utilizing microfluidic device orientation inversion and confocal pinhole reduction. FC-40 was demonstrated to be compatible with droplet microfluidic devices that utilize oil as the carrier fluid for emulsion droplets. Both colony and unicellular microalgae underwent successful *in vivo* lipid analysis inside the droplet microfluidic apparatus. The effect of nitrogen depletion on both droplet encapsulated and free-floating microalgae was observed. Time course measurements of lipid production in 8 different nitrogen concentration conditions were performed using Raman spectroscopy. Raman spectroscopy quantified total lipid production on the microfluidic droplet device and was shown to have a strong correlation with results from a conventional fluorescence quantification measurements.

Thus real-time, non-destructive, label-free, single-cell resolution lipid analysis from the combination of Raman spectroscopy and microfluidics is a viable option for improvement upon current large scale lipid production methods.

CHAPTER VI

ENABLING TIME RESOLVED MICROSCOPY WITH RANDOM RAMAN LASING*

6.1 Background and Motivation

Pursuit of novel imaging methods and techniques is ever present in the field of optics. Improvements in imaging typically come from increased spatial resolution by say increased pixel count [115,116] or the ability to record faster moving events with a faster "shutter" speed (an increase in temporal resolution) [117]. When imaging technology advances, scientists can probe farther into unknown processes. A particular problem exists when attempting to record increasingly faster events. As the exposure time decreases, the amount of light the camera sees decreases. Thus requiring extremely intense light sources to illuminate the subject of the recording and provide the high quality image desired.

While a variety of sources can provide this intense flash, laser pulses are uniquely qualified to serve the role. A laser pulse removes the need for a mechanical or electronic shutter when imaging evolving events as the pulse duration acts as its own gate. Laser pulses in commercially available systems can have durations on the order of femtoseconds allowing for very brief events to be observed. Pulsed laser systems

---

typically have extremely high peak power and are intensely bright. Generation of a laser be it pulsed or continuous wave generally requires a high degree of spatial coherence. The spatial coherence leads to speckle formation degrading image quality. Speckle patterns arise due to the scattering of the spatially coherent light off of a surface. The scattered light interferes with itself creating dark and light spots, or speckle. Removing speckle from the image requires an incoherent laser source.

Conventional incoherent light sources used in imaging undergo spontaneous emission to generate light. Applied to microscopy, these sources can illuminate the entire field of view, which is known as wide-field microscopy. Typical sources of light sources used are halogen, arc lamps, or light emitting diodes (LED). Unlike laser sources, these incoherent sources of light cannot be pulsed at rapid speeds. Capturing extremely rapid motion at high resolution then becomes difficult. The thermal nature of these spontaneous sources limits the overall output of light used to illuminate the subject.

A multi-mode laser or random laser solves the speckle problem by lacking spatial coherence [118-121]. Random lasing occurs when multiple scattering events occur within a gain medium. The traditional optical cavity limits the accessible modes of a laser by use of say two mirrors. Random lasers lack an optical cavity and instead utilize a highly disordered gain medium and multiple scattering to exceed lasing thresholds. Multiple scattering acts as a random walk through a medium removing wave interference and thereby removing spatial coherence. Random lasing's main limitation preventing implementation is a lack of light of sufficient intensity. The generated laser

light propagating through the gain medium tends to be reabsorbed. The strong absorption of the pump laser tends to damage the gain medium.

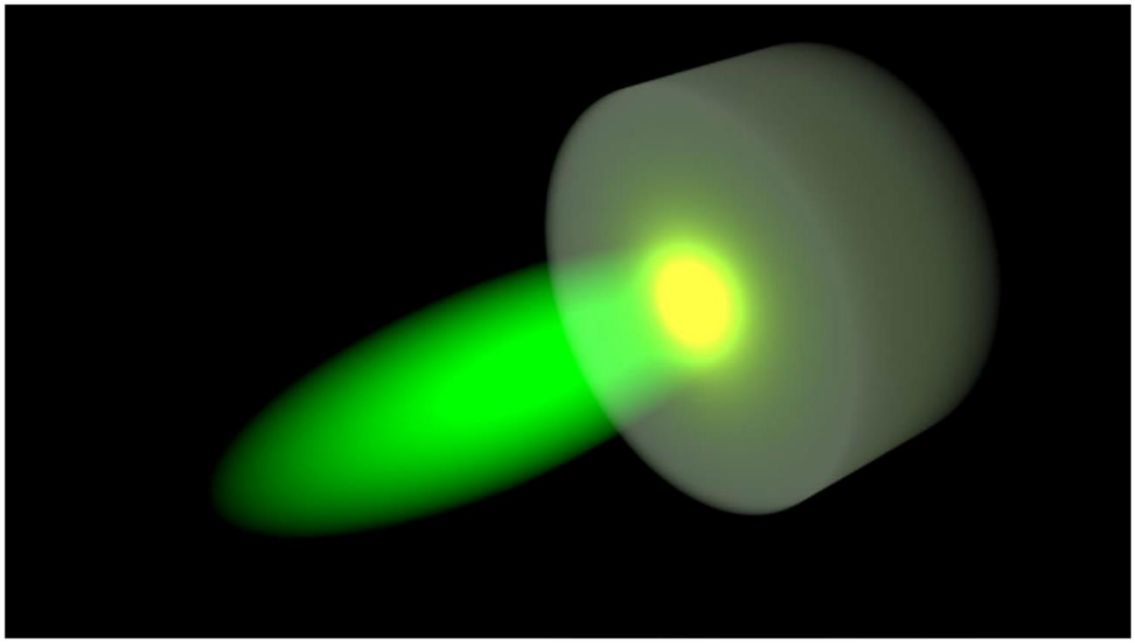

Figure VI.1: Conceptual drawing of random Raman lasing emission (yellow) being stimulated by incident pump laser (green).

Random Raman lasing is the solution to imaging by generating a very bright light source without loss of quality due to speckle. As discussed in Chapter 1, Raman scattering does not require absorption of excitation radiation to generate signal. The spectra generated can have many Raman peaks, corresponding to the different vibrational modes of the molecule. Stimulated Raman scattering (SRS) resonantly enhances the emission of a particular Raman peak by utilizing a two photon process, meaning two photons are incident upon the molecule to generate the signal [Fig. VI.1]. A pump photon excites the molecule and a second photon, the Stokes photon, selects the

scattering mode by creating a resonant coupling between the ground state and a specific vibrational state. The resonance prevents any signal from any other molecular vibrational state other than the one selected from the incident photon sources.

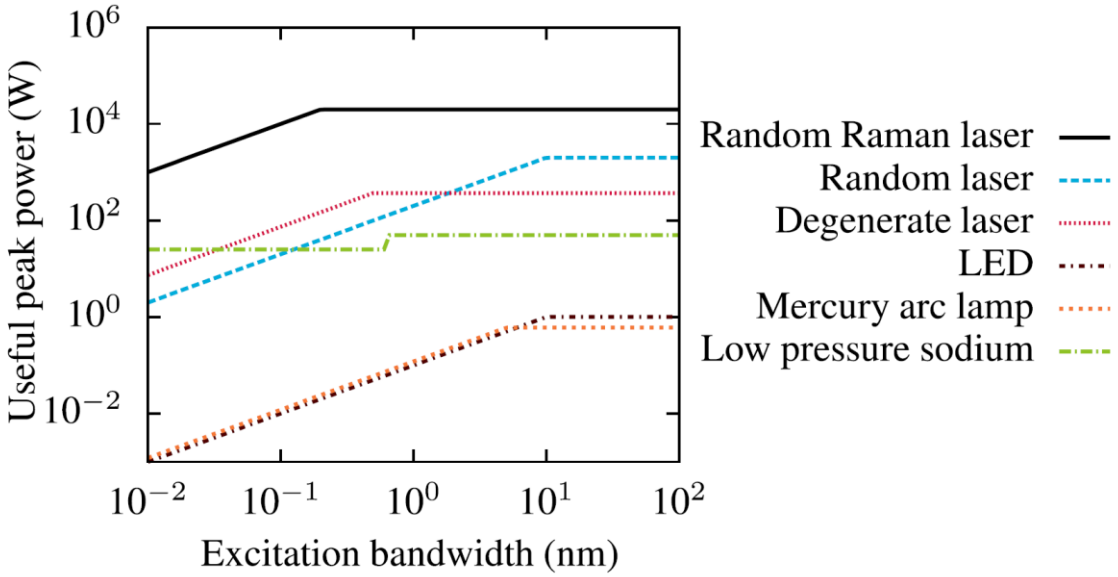

Figure VI.2: Comparison of brightness of different light sources for imaging. Useful peak power is the peak power achieved in a specified bandwidth at the optimum wavelength for that light source. It is the measure of how much light is absorbed by the sample. This is then multiplied by quantum efficiency of the process to obtain the peak power observed by the camera.

Applying SRS as the gain mechanism for random lasing creates a laser imaging tool with several advantages over other imaging methods [122]. The pump laser wavelength doesn't need to be set at an absorption band for the gain medium, allowing more powerful pump sources to be used increasing the Raman response and subsequent emission [Fig VI.2] [123]. The emitted Raman light is not resonant with the energy

levels of the molecule and can be extremely narrowband (approximately 8 cm^{-1}) [Fig VI.3].

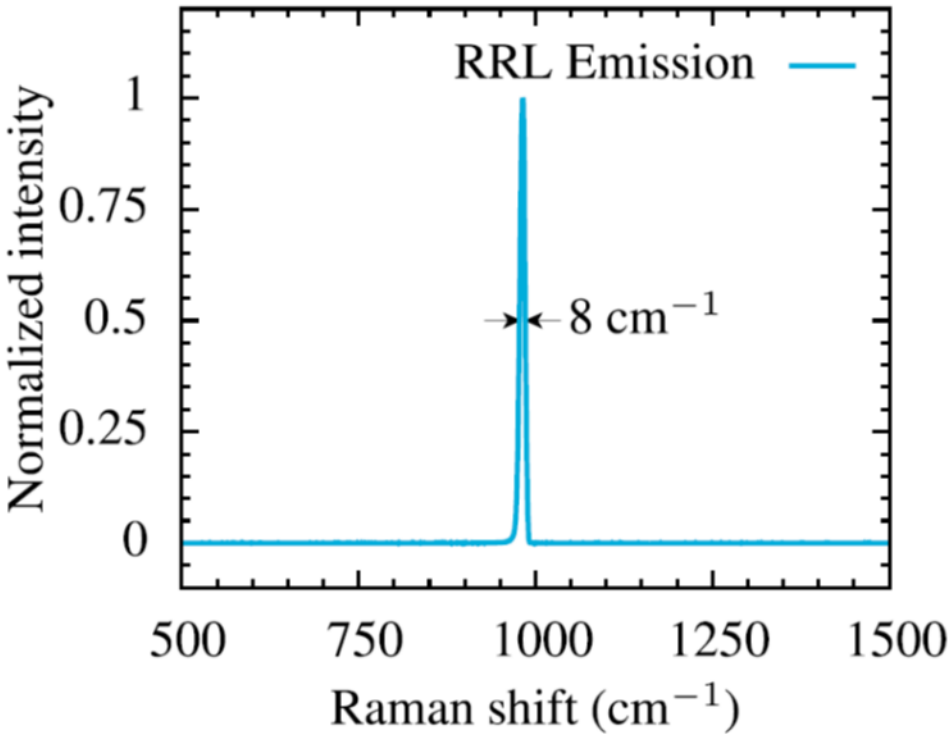

Figure VI.3: Raman emission spectrum of random Raman laser for $BaSO_4$. The 985 cm^{-1} shift from 532 nm pump placing the wavelength of the emission at 562 nm with a 0.25 nm spectral width.

Light emitted from a random Raman laser was used as the strobe source to image the nanosecond timescale dynamics of laser induced breakdown in water.

6.2 Materials and Methods

6.2.1 Characterization of Speckle

The speckle patterns of 3 different light sources were compared to demonstrate the reduction of speckle and viability of a random Raman laser as an imaging strobe. A Hamamatsu Orca-ER, 16-bit CCD captured the speckle images formed by a low spatial

coherence halogen lamp, a highly coherent helium neon (He-NE) laser, and the random Raman laser. Each source passed through a 2 m long 600 μm fiber, exited the fiber uncollimated, and overfilled the CCD array ensuring each pixel was covered. To ensure speckle would be properly imaged, the CCD was placed far enough from the fiber so a speckle grain was significantly larger than the size of a pixel. A 400 by 400 pixel region of the CCD was chosen for analysis as it lacked debris that would interfere with imaging results. The region was subdivided into 25, 80 by 80 pixel, sub-regions. The speckle contrast of each sub-region was computed independently. A background measurement of the CCD dark current noise was taken and subtracted from data. After dark current background subtraction, each sub-region's speckle contrast was averaged over multiple images and the standard deviation was calculated [124,125]. The images chosen for use in the calculations for the halogen and random Raman sources were selected by rejecting any with saturated pixels and required the average counts per pixel to be above 20,000. Thereby ensuring the effect of CCD noise was limited and saturation wasn't occurring. Images taken from the He-Ne laser did not utilize an average pixel count threshold. Instead maximization of the dynamic range of the CCD without saturation was achieved by adjusting the laser power. Calculation of each source's speckle contrast used the following total images: 101 from the halogen, 21 from the He-Ne, and 28 from the random Raman laser. The final value averaged each sub-regions speckle contrast value.

6.2.2 Imaging of Laser Induced Breakdown of Water

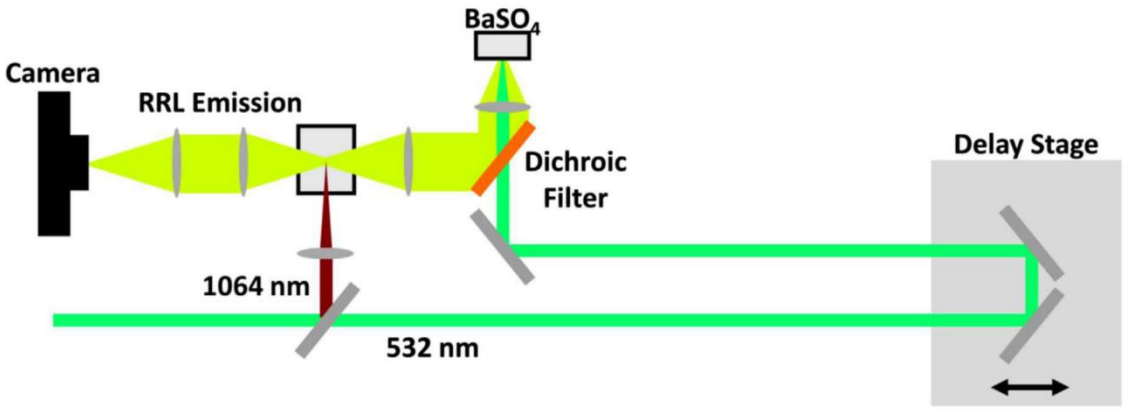

Figure VI.4: Experimental setup for random Raman laser imaging.

Laser induced breakdown of water was imaged using a Spectra Physics Quanta-Ray GCR-3RA [Fig VI.4]. The laser system outputs 50 ps pulses at a rate of 10 Hz. The fundamental wavelength is 1064 nm from a Nd:YAG regenerative amplifier which is frequency doubled to 532 nm light. The residual 1064 nm light was utilized in creating the breakdown of the water filled cuvette by focusing through a Mitutoyo 10x long working distance microscope objective. Neutral density filters adjusted the energy of the 1064 nm beam until nominal pulse energies of 70 µJ were obtained. The 532 nm beam was used as the pump for the random Raman laser. To pump the gain material to generate random Raman lasing, the 532 nm beam passed through a delay stage and reflected off of a Semrock Di02-R532 longpass filter at which point it was measured to have 1.7 mJ of pulse energy. The 532 nm laser was focused onto barium sulfate ($BaSO_4$)

powder (ReagentPlus from Sigma-Aldrich) that was packed into a cylinder 1 cm in diameter and 1 cm in depth and placed in front of the focal plane creating a 1 mm diameter spot on the powder. The random Raman emission was reflected off of the dichroic filter and residual 532 nm light was attenuated by a ThorLabs NF533-17 6 OD notch filter. The Raman emission imaged the water breakdown onto a Hamamatsu Orca-100 CCD. A 10x long working distance objective (Mitutoyo) was used to collect the light along with a 500 mm lens to achieve a magnification of 25x. Plasma light emissions from laser induced breakdown or higher order random Raman emission lines were prevented from reaching the camera by use of a 560 nm bandpass filter [126].

6.3 Results and Discussion

6.3.1 Analysis of Speckle Contrast

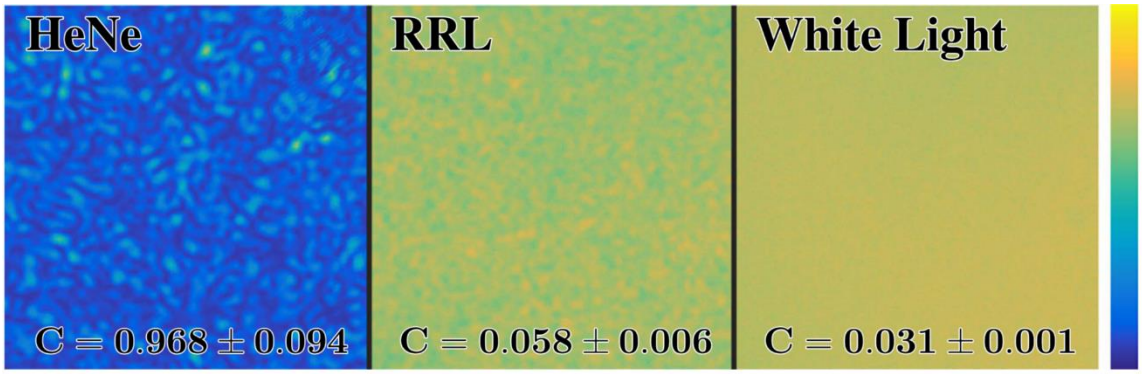

Figure VI.5: Comparison of speckle contrast images from HeNe laser, random Raman laser, and halogen light sources. The calculated speckle contrast C indicates that while the random Raman laser has some spatial coherence, it is very low, especially when compared to that of a coherent HeNe laser.

After imaging the He-Ne laser, halogen, and random Raman laser sources of light onto the CCD, the speckle contrast was calculated by:

$$C = \frac{\sigma}{\langle I \rangle} \quad \text{(Eq. 6.1)}$$

where C is the speckle contrast, σ is the standard deviation, and $\langle I \rangle$ is the average value of the intensity. Thus giving a quantitative value for the spatial coherence of the light source. The speckle contrast values for the He-Ne, random Raman laser, and the halogen bulb are 0.968 ± 0.094, 0.058 ± 0.006, and 0.031 ± 0.001 respectively [Fig VI.5]. The calculation indicates that a small amount of spatial coherence exists in the random Raman laser, but when small by comparison to other common sources, such as superluminescent diodes [127]. Speckle patterns from the random Raman laser have been observed to be unique to each pulse. This indicates that the effect of spatial coherence in random Raman lasing can be further reduced by averaging over multiple pulses.

6.3.2 Analysis and Comparison of Imaging of Laser Induced Breakdown of Water

Using the setup, laser induced breakdown was imaged in three different manners to compare random Raman lasing to other conventional imaging methods. The experimental setup was adjusted minimally to image the shockwave in the water using fluorescence as well as the 532 nm pulse itself to act as the strobe mechanisms. Imaging at specific points in the breakdown was accomplished using the delay stage in the apparatus, with time zero occurring when the strobe and breakdown pulse arrive in the cuvette at the same time. As time goes forward, the images show how the breakdown shockwave expands. Each image was intensity scaled to maximize the contrast in the image, but were not processed any further.

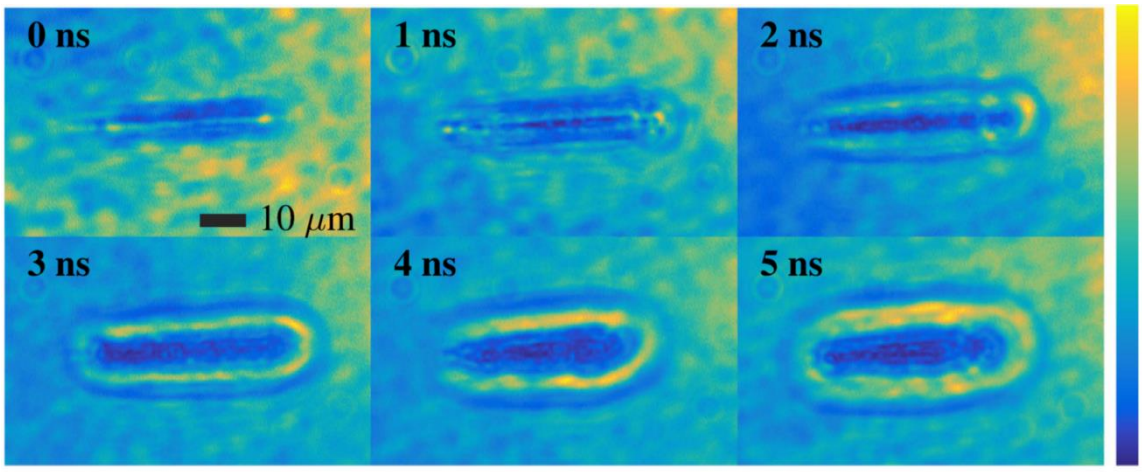

Figure VI.6: Images of laser induced breakdown of water at different delay stage times using random Raman laser. As the time passes, the shockwave is observed to propagate through the water. Very fine details of the breakdown can be observed.

Examining the images taken with the random Raman laser, the shockwave can be easily tracked as it expands from the initial breakdown and smaller details demonstrate the inhomogeneity of the breakdown [Fig VI.6]. The illumination is non-uniform and is brighter on one end of the image than the other. Background subtraction is one method for removing the problem, and another would be to utilize a multi-mode fiber. Passing the random Raman strobe light through the fiber and imaging the exit tip through the system would evenly distribute the strobe light.

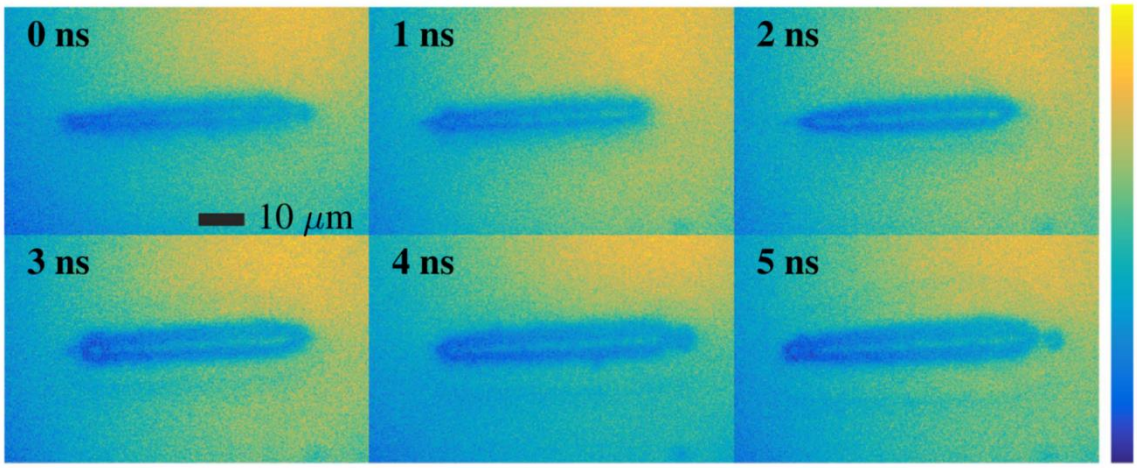

Figure VI.7: Images of laser induced breakdown of water at different delay stage times using fluorescence from a Rhodamine 590 dye. While the fluorescence provides a strong contrast with the breakdown, the lifetime of the fluorescence decay is on the order of the lifetime of the shockwave (ie. nanoseconds). The temporal resolution is degraded and shockwave features cannot be made out.

The fluorescence strobe modified the random Raman laser setup by removing the $BaSO_4$ and introducing a Rhodamine 590 dye that was pumped by the 532 nm laser. Fluorescence emission lifetime from the dye is on the order of nanoseconds [128]. Due to the lifetime of the breakdown also being on the order of several nanoseconds, the images are blurry and lack temporal resolution preventing observation of the smaller details apparent in the random Raman laser images [Fig VI.7].

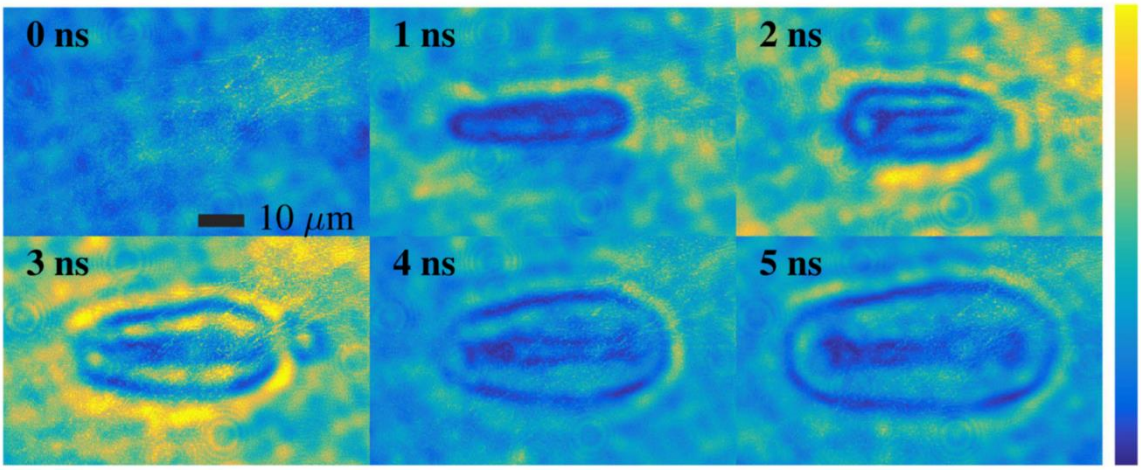

Figure VI.8: Images of laser induced breakdown of water at different delay stage times using the 50 ps 532 nm laser pulse. While providing more detail than the fluorescence strobe, the coherence of the beam leads to a large amount of speckle preventing imaging of the small details within the shockwave.

When the 532 nm laser pulse acts as the strobe for the breakdown, the result is better temporal resolution as the laser pulse doesn't have to interact with a medium to generate another emission to act as the strobe. Observing the images taken with the 532 nm laser pulse strobe, the tiny details observed in the center of the breakdown with random Raman lasing are not distinguishable [Fig VI.8]. The spatial coherence of the laser pulse degrades the quality of the image through speckle as predicted, despite little scattering present in the system. Should any sample with higher scattering be introduced, the image take would be far worse.

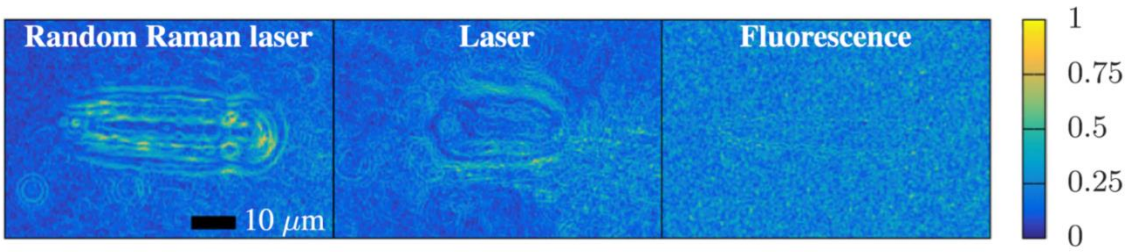

Figure VI.9: Sobel filtered images of random Raman laser, 532 nm laser, and fluorescence images at 2 ns delay stage. The Sobel filter is an image processing tool that detects the edge imaged objects by recognizing where contrast between two parts of an image is high. The Sobel filter enhances the difference between different strobe methods, further proving that random Raman lasing is a strong tool for image capture.

While quantification of the image quality in each case is difficult to assess, there are other means by which one can assess them. The sharpness of the image can be assessed using a Sobel filter. A Sobel filter calculates the directional variation in the intensity of an image, also known as an image gradient. When applied to an image, the Sobel filter creates an image that emphasizes edges in the original picture. When applied to each of the imaging methods discussed, the differences in the sharpness of the image become pronounced [Fig VI.9]. The small details in the center of the breakdown illuminated by the random Raman laser become even more resolved, whereas the image produced by the 532 nm pulse are not. The Sobel filter applied to the fluorescence image the breakdown appears to have been removed entirely.

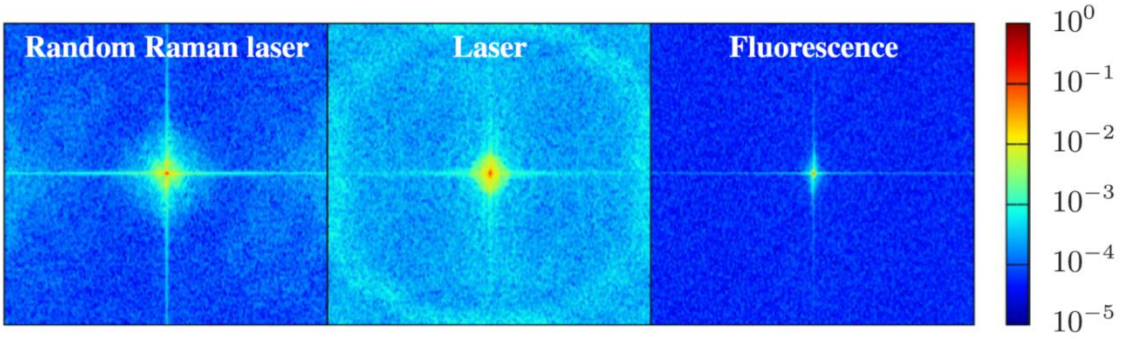

Figure VI.10: Fast Fourier Transform applied to each imaging strobe at 2 ns delay stage. The FFT of the three images gives important information about each strobe method by determining the number of spatial frequencies in each image. The laser image has a bright and broad background spectral frequency due to speckle. The low temporal resolution for the fluorescence strobe leads to low spatial frequencies. The FFT random Raman lasing balances the other two with a large number of spatial frequencies, and better temporal coherence implying less speckle.

The application of a fast Fourier transform (FFT) can provide a measure of the spatial frequencies in the image [Fig VI.10]. Spatial frequencies in an image can be described as the variations in color over the image plane. By taking the FFT of the original image, a measure of the number of spatial frequencies is visualized. The FFT of the image caused by the 532 nm laser pulse indicates a large number of spatial frequencies in the image. The background frequency is exceptionally large which is due to the speckle in the image. The FFT of the fluorescence supports only low spatial frequencies, caused by the low temporal resolution of events, and has a low background frequency, due to lack of speckle. The random Raman laser's FFT shows a balance between the other two. Large number of spatial frequencies available, but with a reduced high frequency background due to speckle.

6.4 Conclusion

Random Raman lasing has been demonstrated to be an effective tool for wide-field microscopy. Specifically, it has the ability to deliver extremely bright, narrowband, and low spatial coherent light pulses that reduce image issues caused by speckle while retaining the ability to image rapidly transpiring events. The application of random Raman lasing to imaging of laser induced breakdown was demonstrated to show features more clearly than illumination from a laser pulse or fluorescence strobe. Specifically, random Raman emission demonstrated wide-field microscopy imaging with nanosecond temporal resolution and reduction of spatial coherent caused image degradation.

The gain mechanism for the random Raman laser being SRS, it is obvious that the emission selection can be tailored to the problem at hand. In the experiment, the 532 nm light underwent a 985 cm^{-1} Raman shift from interacting with $BaSO_4$ causing Raman emission at 562 nm. This emission isn't the only possible one however. If prepared properly, the random Raman laser could excite emissions at 595 nm or 632 nm by causing higher-order effects [126]. Should that occur, one could imagine utilizing optical filtering tools to perform multispectral imaging from a single light source. Alternatively, adjusting the pump wavelength would adjust the emission wavelength for the random Raman laser. Fluorescence microscopy would be uniquely benefited by maximizing the quantum efficiency of the fluorescence molecule transition.

CHAPTER VII

CONCLUSION

Lasers are a tool uniquely suited to solving and investigating numerous problems and questions. Utilization of lasers also carries significant risk to those who operate them. The work presented in this dissertation aims to address some of the novel applications of lasers as well as their dangers. The potential for damage to the eye due to ultrafast laser pulses and the nonlinear phenomena generated was investigated. The critical thresholds nonlinear phenomena were explored to understand maximum permissible exposures in the new regimes that were previously unexplored due to lack of laser sources. A Raman microscope was characterized using the Allan variance to understand optimal averaging times. The optimal averaging time is useful to researchers in maximizing their signal-to-noise ratio. Raman microscopy was investigated as a tool for improving commercial production methods, due to the unique chemical and molecular quantification information it can provide. Finally, a random Raman laser strobe was shown to have significant advantages in imaging when compared to fluorescence and laser strobe sources. While none of these areas of study are complete, the progress detailed within should provide future researchers a guide for future avenues of study.

REFERENCES

[1] J. P. Gordon, H. J. Zeiger, and C. H. Townes, "The maser-new type of microwave amplifier, frequency standard, and spectrometer," Phys. Rev. **99**, 1264-1274 (1995).

[2] ANSI Z136.1-2014 Laser Safety Standard for the Safe Use of Lasers, Laser Institute of America, Orlando, Florida (2014).

[3] J. A. Zuclich, D. J. Lund, B. E. Stuck, and P. R. Edsall, "Wavelength dependence of ocular damage thresholds in the near-IR to far-IR transition region (Proposed revisions to MPEs)," Proceedings ILSC 2005 (2005).

[4] J. A. Zuclich, D. A Gagliano, F. Cheney, B. E. Stuck, H. Zwick, P. R. Edsall, and D. J. Lund, "Ocular Effects of Penetrating IR Laser Wavelengths," Proc. SPIE 2391, pp. 112–125 (1995).

[5] J. A. Zuclich, D. J. Lund, and B. E. Stuck, "Wavelength Dependence of Ocular Damage Thresholds in the Near-IR to Far-IR Transition Region: Proposed Revisions to MPEs," Health Physics 92 (1), pp. 15-23 (2006).

[6] J. A. Zuclich, S. Schuschereba, H. Zwick, F. E. Cheney, and B. E. Stuck, "Comparing Laser Induced Retinal Damage from IR Wavelengths to that from Visible Wavelengths," Proc. SPIE 2674, pp. 66-79 (1996).

[7] J. A. Zuclich, S. T. Schuschereba, H. Zwick, S. A. Boppart, J. G. Fujimoto, F. E. Cheney, and B. E. Stuck, "A Comparison of Laser-Induced Retinal Damage from Infrared Wavelengths to that from Visible Wavelengths," Lasers Light Ophthalmol **8**, pp. 15–29 (1997).

[8] J. A. Zuclich, H. Zwick, S. T. Schuschereba, B. E. Stuck, and F. E. Cheney, "Ophthalmoscopic and Pathologic Description of Ocular Damage Induced by Infrared Laser Radiation," J Laser Applications **10**, pp. 114 –120 (1998).

[9] J. A. Zuclich, D. J. Lund, P. R. Edsall, B. E. Stuck, and G. T. Hengst, "High-Power Lasers in the 1.3 to 1.4 μm Wavelength Range: Ocular Effects and Safety Standards Implications," Proc. SPIE 4246, pp. 78–88 (2001).

[10] J. A. Zuclich, D. J. Lund, B. E. Stuck, and P. R. Edsall, "Ocular Effects and Safety Standards Implications for High-Power Lasers in the 1.3–1.4 μm Wavelength Range," Brooks City-Base, TX: Air Force Research Laboratory, Optical Radiation Branch; AFRL-HE-BR-TR-2004-0187 (2004).

[11] J. A. Zuclich, D. J. Lund, and B. E. Stuck, “Wavelength Dependence of Ocular Damage Thresholds in the Near-IR to Far-IR Transition Region (Proposed Revision to MPEs),” Proc. International Laser Safety Conference, Marina del Rey. Orlando, FL. Laser Institute of America, pp. 58–66 (2005).

[12] R. Vincelette, B. A. Rockwell, J. W. Oliver, S. S. Kumru, R. J. Thomas, K. J. Schuster, G. D. Noojin, A. D. Shingledecker, D. J. Stolarski, and A. J. Welch, “Trends in Retinal Damage Thresholds from 100-Millisecond Near-Infrared Laser Radiation Exposures: A Study at 1,110, 1,130, 1,150, and 1,319 nm,” Las. Surg. Med. **41**, pp. 382–390 (2009).

[13] J. L. Krause, K. J. Schafer, and K. C. Kulander, “High-order harmonic generation from atoms and ions in the high intensity regime,” Phys. Rev. Lett., **68**, p. 3535 (1992).

[14] A. V. Mitrofanov, A. A. Voronin, D. A. Sidorov-Biryukov, A. Pugzlys, E. A. Stepanov, G. Andriukaitis, T. Flory, S. Alisauskas, A. B. Fedotov, A. Baltuska, and A. M. Zheltikov, “Mid-Infrared Laser Filaments in the Atmosphere,” Scientific Reports **5**, (2015).

[15] M. Han, G. Giese, and J. F. Bille, “Second harmonic generation imaging of collagen fibrils in corena and sclera,” Opt. Express **13**, pp. 5791-5797 (2005).

[16] D. J. Brown, N. Morishige, A. Neekhra, D. S. Minckler, and J. V. Jester, “Application of second harmonic imaging microscopy to assess structural changes in optic nerve head structure ex vivo,” Journal of Biomedical Optics **12**, pp. 024029 (2007).

[17] R. R. Alfano, and S. L. Shapiro, “Emission in the Region 4000 to 7000 Å Via Four-Photon Coupling in Glass,” Phys. Rev. Lett. **24**, pp. 584–587 (1970).

[18] F. Shimizu, “Frequency broadening in liquids by a short light pulse,” Phys. Rev. Lett. **19**, p. 1097 (1967)

[19] R. H. Stolen, and A. Ashkin, “Optical Kerr effect in glass waveguide,” Appl. Phys. Lett. **22**, pp. 294 (1973)

[20] G. New, “Introduction to Nonlinear Optics,” Cambridge University Press. ISBN 978-1-139-50076-0 (2011).

[21] G. I. Petrov, and V. V. Yakovlev, “Enhancing red-shifted white-light continuum generation in optical fibers for applications in nonlinear Raman microscopy,” Opt. Express **13**, p. 1299 (2005).

[22] D. Wildanger, E. Rittweger, L. Kastrup, and S. W. Hell, “STED microscopy with a supercontinuum laser source,” Opt. Express **16**, p. 9614 (2008).

[23] I. Hartl, X. D. Li, C. Chudoba, R. K. Ghanta, T. H. Ko, J. G. Fujimoto, J. K. Ranka, and R. S. Windeler, "Ultrahigh-resolution optical coherence tomography using continuum generation in an air–silica microstructure optical fiber," Opt. Lett. **26**, p. 608 (2001).

[24] R. W. Boyd, "Nonlinear Optics," Academic press, (2003).

[25] J. Kasparian, M. Rodriguez, G. Mejean, J. Yu, E. Salmon, H. Wille, R. Bourayou, S. Frey, Y.-B. Andre, A. Mysyrowicz, R. Sauerbrey, J.-P. Wolf, and L. Woste, "White-light filaments for atmospheric analysis," Science **301**, pp. 61–64 (2003).

[26] K. Stelmaszczyk, P. Rohwetter, G. Méjean, J. Yu, E. Salmon, J. Kasparian, R. Ackermann, J.-P. Wolf, and L. Wöste, "Long-distance remote laser-induced breakdown spectroscopy using filamentation in air," Appl. Phys. Lett. **85**, p. 3977 (2004).

[27] P. Rairoux, H. Schillinger, S. Niedermeier, M. Rodriguez, F. Ronneberger, R. Sauerbrey, B. Stein, D. Waite, C. Wedekind, H. Wille, L. Wöste and C. Ziener, "Remote sensing of the atmosphere using ultrashort laser pulses," App. Phys. B **71**, pp. 573-580 (2000).

[28] A. Couairon and A. Mysyrowicz, "Femtosecond filamentation in transparent media," Phys. Rep. **441**, pp. 47–189 (2007).

[29] T. L. Weiss, H. J. Chun, S. Okada, S. Vitha, A. Holzenburg, J. Laane and T. P. Devarenne, "Raman Spectroscopy Analysis of Botryococcene Hydrocarbons from the Green Microalga *Botryococcus braunii*," J. Biol. Chem. **285**, pp. 32458-32466 (2010).

[30] O. Samek, P. Zemanek, A. Jonas, and H. H. Telle, "Characterization of oil-producing microalgae using Raman spectroscopy," Laser Phys. Lett. **8**, pp. 701-709 (2011).

[31] S. R. Fagerer, T. Schmid, A. J. Ibanez, M. Pabst, R. Steinhoff, K. Jefimovs, P. L. Urban, and R. Zenobi, "Analysis of single algal cells by combining mass spectrometry with Raman and fluorescence mapping," Analyst **138**, pp. 6732-6736 (2013).

[32] A. Saha, and S. Deb, "Broadband second-harmonic generation in the near-infrared region in a tapered zinc selenide slab using total internal reflection quasi-phase matching," Japanese J. of Appl. Phys. **50**, pp. 102201 (2011).

[33] A. H. Chin, O. G. Calderón, and J. Kono, "Extreme midinfrared nonlinear optics in semiconductors," Phys. Rev. Lett. **86**, pp. 3292-3295 (2001).

[34] M. Weber, "Handbook of Optical Materials," Boca Raton: CRC Press. (2002).

[35] C. K. N. Patel, "Optical harmonic generation in the infrared using a CO2 laser," Phys. Rev. Lett. **16**, pp. 613-616 (1966).

[36] L. Gallais, and M. Commandre, "Laser-induced damage thresholds of bulk and coating optical materials at 1030 nm, 500 fs," Appl. Opt. **53**, pp. A186-A196 (2014).

[37] T. D. Krauss and F. W. Wise, "Femtosecond measurement of nonlinear absorption and refraction in CdS, ZnSe, and ZnS," Appl. Phys. Lett. **65**, p. 1739 (1994).

[38] M. Baudrier-Raybaut, R. Haïdar, Ph. Kupecek, Ph. Lemasson and E. Rosencher, "Random quasi-phase-matching in bulk polycrystalline isotropic nonlinear materials," Nature **432**, pp. 374-376 (2004).

[39] T. D. Chinh, W. Seibt, and K. Siegbahna, "Dot patterns from second-harmonic and sum-frequency generation in polycrystalline ZnSe," J. of Appl. Phys. **90**, pp. 2612-2614 (2001).

[40] R. Šuminas, G. Tamošauskas, G. Valiulis, V. Jukna, A. Couairon, and A. Dubietis, "Multi-octave spanning nonlinear interactions induced by femtosecond filamentation in polycrystalline ZnSe," Appl. Phys. Lett. **110**, p. 241106 (2017).

[41] A. Dubietis, G. Tamošauskas, R. Šuminas, V. Jukna, and A. Couairon, "Ultrafast supercontinuum generation in bulk condensed media," Lithuanian Journal of Physics, **57**, pp. 113-157 (2017).

[42] M. Durand, A. Houard, K. Lim, A. Durécu, O. Vasseur, and M. Richardson, "Study of filamentation threshold in zinc selenide," Opt. Express **22**, p. 5852 (2014).

[43] O. Mouawad, P. Béjot, F. Billard, P. Mathey, B. Kibler, F. Désévédavy, G. Gadret, J.-C. Jules, O. Faucher, and F. Smektala, "Filament-induced visible-to-mid-IR supercontinuum in a ZnSe crystal: Towards multi-octave supercontinuum absorption spectroscopy," Optical Materials **60**, pp. 355-358 (2016).

[44] V. V. Yakovlev, B. Kohler, and K. R. Wilson, "Broadly tunable 30-fs pulses produced by optical parametric amplification," Opt. Lett. **19**, pp. 2000-2002 (1994).

[45] K. R. Wilson, and V. V. Yakovlev, "Ultrafast rainbow: tunable ulltrashort pulses from a solid-state kilohertz system" JOSA B **14**, pp. 444-448 (1997).

[46] A. Braun, G. Korn, X. Liu, D. Du, J. Squier, and G. Mourou, "Self-channeling of high-peak-power femtosecond laser pulses in air," Opt. Lett. **20**, pp. 73–75 (1995).

[47] L. Berge´, S. Skupin, R. Nuter, J. Kasparian, and J. P. Wolf, “Ultrashort filaments of light in weakly ionized, optically transparent media” Rep. Prog. Phys. **70**, p. 1633 (2007).

[48] S. Tzortzakis, B. Lamouroux, A. Chiron, S. D. Moustaizis, D. Anglos, M. Franco, B. Prade, and A. Mysyrowicz, “Femtosecond and picosecond ultraviolet laser filaments in air: experiments and simulations,” Opt. Commun. **197**, pp. 131–143 (2001).

[49] B. Prade, M. Franco, A. Mysyrowicz, A. Couairon, H. Buersing, B. Eberle, M. Krenz, D. Seiffer, and O. Vasseur, "Spatial mode cleaning by femtosecond filamentation in air," Opt. Lett. **31**, pp. 2601-2603 (2006).

[50] J. F. Daigle, A. Jaron-Becker, S. Hosseini, T.-J. Wang, Y. Kamali, G. Roy, A. Becker, and S. L. Chin, “Intensity clamping measurement of laser filaments in air at 400 and 800 nm,” Phys. Rev. A **82**, p. 023405 (2010).

[51] D. Mikalauskas, A. Dubietis, and R. Danielius, “Observation of light filaments induced in air by visible picosecond laser pulses,” Appl. Phys. B **75**, p. 899–902 (2002).

[52] A. V. Mitrofanov, A. A. Voronin, D. A. Sidorov-Biryukov, G. Andriukaitis, T. Flöry, A. Pugžlys, A. B. Fedotov, J. M. Mikhailova, V. Ya. Panchenko, A. Baltuška, and A. M. Zheltikov, "Post-filament self-trapping of ultrashort laser pulses," Opt. Lett. **39**, pp. 4659-4662 (2014).

[53] L. Haizer, I. Bugar, E. Serebryannikov, D. Lorenc, F. Uherek, E. Goulielmakis, and A. Zheltikov, "Intense Cr:forsterite-laser-based supercontinuum source," Opt. Lett. **39**, pp. 5562-5565 (2014).

[54] A. A. Voronin, S. Alisauskas, O. D. Mucke, A. Pugzlys, A. Baltuska, and A. M. Zheltikov, “High-energy-throughput pulse compression by off-axis group-delay compensation in a laser-induced filament,” Phys. Rev. A. **84**, p. 023832 (2011).

[55] S. Driever, D. Bigourd, N. Fedorov, M. Cornet, M. Arnold, F. Burgy, S. Montant, S. Petit, D. Descamps, E. Cormier, E. Constant, and A. Zair, “Tunable 1.6–2 μm near infrared few-cycle pulse generation by filamentation,” Appl. Phys. Lett. **102**, p. 191119 (2013).

[56] C. P. Hauri, R. B. Lopez-Martens, C. I. Blaga, K. D. Schultz, J. Cryan, R. Chirla, P. Colosimo, G. Doumy, A. M. March, C. Roedig, E. Sistrunk, J. Tate, J. Wheeler, L. F. DiMauro, and E. P. Power, "Intense self-compressed, self-phase-stabilized few-cycle pulses at 2 μm from an optical filament," Opt. Lett. **32**, pp. 868-870 (2007).

[57] R. R. Alfano and S. L. Shapiro, "Emission in the Region 4000 to 7000 Å Via Four-Photon Coupling in Glass," Phys. Rev. Lett. **24**, pp. 584–587 (1970).

[58] C. P. Hauri, W. Kornelis, F. W. Helbing, A. Heinrich, A. Couairon, A. Mysyrowicz, J. Biegert, and U. Keller, "Generation of intense, carrier-envelope phase-locked few-cycle laser pulses through filamentation," Appl. Phys. B **79**, pp. 673–677 (2004).

[59] B. D. Strycker, K. Wang, M. Springer, and A.V. Sokolov, "Chemical-specific imaging of shallowly buried objects using femtosecond laser pulses," Appl. Opt. **52**, pp. 4792-4796 (2013).

[60] K. Wang, B. D. Strycker, D. V. Voronine, P. K. Jha, M. O. Scully, R. E. Meyers, P. Hemmer, and A. V. Sokolov, "Remote sub-diffraction imaging with femtosecond laser filaments," Opt. Lett. **37**, pp. 1343-1345 (2012).

[61] L. A. Nafie, "Recent advances in linear and non-linear Raman Spectroscopy. Part IX," J. Raman Spectr. **46**, p. 1173 (2015).

[62] S. Stockel, J. Kirchhoff, U. Neugebauer, P. Rosch, and J. Popp, "The application of Raman spectroscopy for the detection and identification of microorganisms," J. Raman Spectr. **47**, p. 89 (2016).

[63] K. C. Doty, C. K. Muro, J. Bueno, L. Halamkova, and I. K. Lednev, "What can Raman spectroscopy do for criminalistics?" J. Raman Spectr. **47**, p. 39 (2016).

[64] K. L. Gares, K. T. Hufziger, S. V. Bykov, and S. A. Asher, "Review of explosive detection methodologies and the emergence of standoff deep UV resonance Raman," J. Raman Spectr. **47**, p. 124 (2016).

[65] M. O. Scully, G. W. Kattawar, R. P. Lucht, T. Opatrny, H. Pilloff, A. Rebane, A. V. Sokolov, and M. Zubairy, "FAST CARS: Engineering a laser spectroscopic technique for rapid identification of bacterial spores," Proc. Natl. Acad. Sci. USA **99**, p. 10994 (2002).

[66] D. Pestov, G. O. Ariunbold, R. K. Murawski, V. A. Sautenkov, A. V. Sokolov, and M. O. Scully, "Coherent versus incoherent Raman scattering: molecular coherence excitation and measurement", Opt. Lett. **32**, pp. 1725-1727 (2007).

[67] D. Pestov, X. Wang, G. O. Ariunbold, R. K. Murawski, V. A. Sautenkov, A. Dogariu, A. V. Sokolov, and M. O. Scully, "Single-shot Detection of Bacterial Endospores via Coherent Raman Spectroscopy," Proc. Natl. Acad. Sci. USA **105**, 422 (2008).

[68] G. I. Petrov, R. Arora, V. V. Yakovlev, X. Wang, A. V. Sokolov, and M. O. Scully, "Comparison of coherent and spontaneous Raman microspectroscopies for noninvasive detection of single bacterial endospores," Proc. Natnl. Acad. Sci. USA. **104**, p. 7776 (2007).

[69] R. Arora, G. I. Petrov, and V. V. Yakovlev, “Analytical capabilities of coherent anti-Stokes Raman scattering microspectroscopy,” J. Mod. Opt. **55**, p. 3237 (2008).

[70] L. Dupochel, W. Elmi-Rayaleh, C. Ruckebusch, and J. P. Huvenne, “Multivariate curve resolution methods in imaging spectroscopy: Influence of extraction methods and instrumental perturbations,” J. Chem. Inform. Comp. Sci. **43**, p. 2057 (2003).

[71] P. Werle, R. Mücke, and F. Slemr, “The limits of signal averaging in atmospheric trace-gas monitoring by tunable diode-laser absorption spectroscopy (TDLAS),” Appl. Phys. B. **57**, p. 131 (1993).

[72] J. Skřínský, R. Janečková, E. Grigorová, M. Střižík, P. Kubát, L. Herecová, V. Nevrlý, Z. Zelinger, and S. Civiš, “Allan variance for optimal signal averaging—monitoring by diode-laser and CO2 laser photo-acoustic spectroscopy,” Journal of Molecular Spectroscopy **256**, p. 99 (2009).

[73] D. R. Bowling, S. D. Sargent, B. D. Tanner, and J. R. Ehleringer, “Tunable diode laser absorption spectroscopy for stable isotope studies of ecosystem-atmosphere CO2 exchange,” Agricultural and Forest Meteorology **118**, p. 1 (2003).

[74] L. Joly, B. Parvitte, V. Zeninari, and G. Durry, “Development of a compact CO2 sensor open to the atmosphere and based on near-infrared laser technology at 2.68 μm,” App. Phys. B: Lasers & Optics **86**, p. 743 (2007).

[75] B. Tuzson, M. J. Zeeman, M. S. Zahniser, and L. Emmenegger, “Quantum cascade laser based spectrometer for in situ stable carbon dioxide isotope measurements,” Infrared Physics & Technology **51**, p. 198 (2008).

[76] D. W. T. Griffith, N. M. Deutscher, C. Caldow, G. Kettlewell, M. Riggenbach, and S. Hammer, “A Fourier transform infrared trace gas and isotope analyser for atmospheric applications,” Atmospheric Measurement Techniques **5**, p. 2481 (2012).

[77] V. L. Kasyutich, R. K. Raja Ibrahim, and P. A. Martin, “Stability of widely tuneable, continuous wave external-cavity quantum cascade laser for absorption spectroscopy,” Infrared Physics & Technology **53**, p. 381 (2010).

[78] Z. K. Meng, G. I. Petrov, S. N. Cheng, J. A. Jo, K. K. Lehmann, V. V. Yakovlev, and M. O. Scully, “Lightweight Raman spectroscope using time-correlated photon-counting detection,” Proc. Natnl. Acad. Sci. USA. **112**, p. 12315 (2015).

[79] Y. He, W. Bo, R. K. Dukor, and L. A. Nafie, "Determination of Absolute Configuration of Chiral Molecules Using Vibrational Optical Activity: A Review," Appl. Spectrosc. **65**, pp. 699-723 (2011).

[80] Q. Hu, M. Sommerfeld, E. Jarvis, M. Ghirardi, M. Posewitz, M. Seibert, and A. Darzins, “Microalgal triacylglycerols as feedstocks for biofuel production: perspectives and advances,” Plant J. **54**, pp. 621-639 (2008).

[81] L. Rodolfi, G. Chini Zittelli, N. Bassi, G. Padovani, N. Biondi, G. Bonini, and M. R. Tredici, “Microalgae for oil: Strain selection, induction of lipid synthesis and outdoor mass cultivation in a low-cost photobioreactor,” Biotechnol. Bioeng. **102**, pp. 100-112 (2009).

[82] A. Han, H. Hou, L. Li, H. S. Kim, and P. de Figueiredo, “Microfabricated devices in microbial bioenergy sciences,” Trends Biotechnol **31**, pp. 225-232 (2013).

[83] Y. Ma, Z. Wang, M. Zhu, C. Yu, Y. Cao, D. Zhang and G. Zhou, “Increased lipid productivity and TAG content in Nannochloropsis by heavy-ion irradiation mutagenesis,” Bioresour. Technol. **136**, pp. 360-367 (2013).

[84] B. L. Milman, “Identification of chemical compounds,” TrAC Trends Anal. Chem. **24**, pp. 493-508 (2005).

[85] J. R. Mourant, J. Dominguez, S. Carpenter, K. W. Short, T. M. Powers, R. Michalczyk, N. Kunapareddy, A. Guerra and J. P. Freyer, “Comparison of vibrational spectroscopy to biochemical and flow cytometry methods for analysis of the basic biochemical composition of mammalian cells,” J. Biomed. Opt. **11**, p. 064024 (2006).

[86] J. P. Day, K. F. Domke, G. Rago, H. Kano, H. O. Hamaguchi, E. M. Vartiainen and M. Bonn, “Quantitative Coherent Anti-Stokes Raman Scattering (CARS) Microscopy,” J. Phys. Chem. B **115**, pp. 7713–7725 (2011).

[87] K. Czamara, K. Majzner, M. Z. Pacia, K. Kochan, A. Kaczor and M. Baranska, “Raman spectroscopy of lipids: a review,” J. Raman Spectrosc. **46**, pp. 4–20 (2015).

[88] J. Rumin, H. Bonnefond, B. Saint-Jean, C. Rouxel, A. Sciandra, O. Bernard, J. P. Cadoret and G. Bougaran, “The use of fluorescent Nile red and BODIPY for lipid measurement in microalgae,” Biotechnol. Biofuels **8**, p. 42 (2015).

[89] A. Rakszewska, J. Tel, V. Chokkalingam and W. T. S. Huck, “One drop at a time: toward droplet microfluidics as a versatile tool for single-cell analysis,” NPG Asia Mater. **6**, e133 (2014).

[90] D. Hummer, F. Kurth, N. Naredi-Rainer and P. S. Dittrich, “Single cells in confined volumes: microchambers and microdroplets,” Lab Chip **16**, pp. 447–458 (2016).

[91] A. R. Guzman, H. S. Kim, P. de Figueiredo and A. Han, “A three-dimensional electrode for highly efficient electrocoalescence-based droplet merging,” Biomed. Microdevices **17**, p. 35 (2015).

[92] H. S. Kim, A. R. Guzman, H. R. Thapa, T. P. Devarenne and A. Han, “A droplet microfluidics platform for rapid microalgal growth and oil production analysis,” Biotechnol. Bioeng. **113**, pp. 1691–1701 (2016).

[93] Y. J. Sung, J. Y. Kim, K. W. Bong and S. J. Sim, “Microdroplet photobioreactor for the photoautotrophic culture of microalgal cells,” Analyst **141**, pp. 989–998 (2016).

[94] A. Dewan, J. Kim, R. H. McLean, S. A. Vanapalli and M. N. Karim, “Growth kinetics of microalgae in microfluidic static droplet arrays,” Biotechnol. Bioeng. **109**, pp. 2987–2996 (2012).

[95] J. S. Craigie, S. L. MacKinnon and J. A. Walter, “Liquid seaweed extracts identified using ^{1}H NMR profiles,” J. Appl. Phycol. **20**, pp. 665–671 (2007).

[96] V. H. Work, R. Radakovits, R. E. Jinkerson, J. E. Meuser, L. G. Elliott, D. J. Vinyard, L. M. Laurens, G. C. Dismukes and M. C. Posewitz, “Increased Lipid Accumulation in the Chlamydomonas reinhardtii sta7-10 Starchless Isoamylase Mutant and Increased Carbohydrate Synthesis in Complemented Strains,” Eukaryotic Cell **9**, pp. 1251– 1261 (2010).

[97] Y. Chisti, “Constraints to commercialization of algal fuels,” J. Biotechnol. **167**, pp. 201–214 (2013).

[98] D. R. Georgianna and S. P. Mayfield, “Exploiting diversity and synthetic biology for the production of algal biofuels,” Nature **488**, pp. 329–335 (2012).

[99] T. Merkel, V. Bondar, K. Nagai, B. Freeman and I. Pinnau, “Gas sorption, diffusion, and permeation in poly(dimethylsiloxane),” J. Polym. Sci. Part B: Polym. Phys. **38**, pp. 415–434 (2000).

[100] F. Sarrazin, J.-B. Salmon, D. Talaga and L. Servant, “Chemical Reaction Imaging within Microfluidic Devices Using Confocal Raman Spectroscopy: The Case of Water and Deuterium Oxide as a Model System,” Anal. Chem. **80**, pp. 1689–1695 (2008).

[101] E. C. Santos, H. S. Martinho, K. Annes, R. F. Leite, and M. P. Milazzotto, "Rapid and noninvasive technique to assess the metabolomics profile of bovine embryos produced in vitro by Raman spectroscopy," Biomed. Opt. Express **6**, pp. 2830-2839 (2015).

[102] L. Mazutis, J. Gilbert, W. L. Ung, D. A. Weitz, A. D. Griffiths and J. A. Heyman, “Single-cell analysis and sorting using droplet-based microfluidics,” Nat. Protoc. **8**, pp. 870–891 (2013).

[103] A. M. Nonomura, “Botryococcus braunii var. showa (Chlorophyceae) from Berkeley, California, United States of America,” Jpn. J. Phycol. **36**, pp. 285–291 (1988).

[104] D. S. Gorman and R. P. Levine, “Cytochrome f and plastocyanin: their sequence in the photosynthetic electron transport chain of Chlamydomonas reinhardi,” Proc. Natl. Acad. Sci. U.S.A. **54**, pp. 1665–1669 (1965).

[105] M. Grung, P. Metzger and S. Liaaen-jensen, “Primary and secondary carotenoids in two races of the green alga Botryococcus braunii,” Biochem. Syst. Ecol. **17**, pp. 263–269 (1989).

[106] G. F. Bailey and R. J. Horvat, “Raman spectroscopic analysis of thecis/trans isomer composition of edible vegetable oils,” J. Am. Oil Chem. Soc. **49**, pp. 494–498 (1972).

[107] H. Wu, J. V. Volponi, A. E. Oliver, A. N. Parikh, B. A. Simmons and S. Singh, “In vivo lipidomics using single-cell Raman spectroscopy,” Proc. Natl. Acad. Sci. U.S.A. **108**, pp. 3809–3814 (2011).

[108] X. N. He, J. Allen, P. N. Black, T. Baldacchini, X. Huang, H. Huang, L. Jiang, and Y. F. Lu, "Coherent anti-Stokes Raman scattering and spontaneous Raman spectroscopy and microscopy of microalgae with nitrogen depletion," Biomed. Opt. Express **3**, pp. 2896-2906 (2012).

[109] O. Samek, A. Jonas, Z. Pilat, P. Zemanek, L. Nedbal, J. Triska, P. Kotas and M. Trtilek, “Raman Microspectroscopy of Individual Algal Cells: Sensing Unsaturation of Storage Lipids in vivo,” Sensors **10**, pp. 8635–8651 (2010).

[110] K. E. Cooksey, J. B. Guckert, S. A. Williams and P. R. Callis, “Fluorometric determination of the neutral lipid content of microalgal cells using Nile Red,” J. Microbiol. Methods **6**, pp. 333–345 (1987).

[111] H. S. Kim, T. P. Devarenne and A. Han, “A high-throughput microfluidic single-cell screening platform capable of selective cell extraction,” Lab Chip **15**, pp. 2467–2475 (2015).

[112] H. S. Kim, T. L. Weiss, H. R. Thapa, T. P. Devarenne and A. Han, “A microfluidic photobioreactor array demonstrating high-throughput screening for microalgal oil production,” Lab Chip **14**, pp. 1415–1425 (2014).

[113] B. M. Liszka, H. S. Rho, Y. Yang, A. T. M. Lenferink, L. W. M. M. Terstappen and C. Otto, “A microfluidic chip for high resolution Raman imaging of biological cells,” RSC Adv. **5**, pp. 49350–49355 (2015).

[114] Y. Geng, L. Chen, G. Chen, W. Bi, S. Xu, H. Cui and W. Xu, “Note: A portable Raman analyzer for microfluidic chips based on a dichroic beam splitter for integration of imaging and signal collection light paths,” Rev. Sci. Instrum. **86**, p. 056109 (2015).

[115] M. Dyba and S. W. Hell, “Focal spots of size λ/23 open up far-field florescence microscopy at 33 nm axial resolution,” Phys. Rev. Lett. **88**, pp. 1639011–1639014 (2002).

[116] E. Betzig, G. H. Patterson, R. Sougrat, O. W. Lindwasser, S. Olenych, J. S. Bonifacino, M. W. Davidson, J. Lippincott-Schwartz, and H. F. Hess, “Imaging intracellular fluorescent proteins at nanometer resolution,” Science **313**, pp. 1642–1645 (2006).

[117] L. Gao, J. Liang, C. Li, and L. V. Wang, “Single-shot compressed ultrafast photography at one hundred billion frames per second,” Nature **516**, pp. 74–77 (2014).

[118] M. Nixon, B. Redding, A. A. Friesem, H. Cao, and N. Davidson, "Efficient method for controlling the spatial coherence of a laser," Opt. Lett. **38**, pp. 3858-3861 (2013).

[119] H. Cao, “Lasing in random media,” Waves in Random Media **13**, pp. R1–R39 (2003).

[120] B. Redding, M. A. Choma, and H. Cao, "Spatial coherence of random laser emission," Opt. Lett. **36**, pp. 3404-3406 (2011).

[121] B. Redding, A. Cerjan, X. Huang, M. L. Lee, A. D. Stone, M. A. Choma, and H. Cao, “Low spatial coherence electrically pumped semiconductor laser for speckle-free full-field imaging,” Proc. Natl. Acad. Sci. **112**, pp. 1304–1309 (2015).

[122] B. H. Hokr, M. S. Schmidt, J. N. Bixler, P. N. Dyer, G. D. Noojin, B. Redding, R. J. Thomas, B. A. Rockwell, H. Cao, V. V. Yakovlev, and M. O. Scully, “A narrow-band speckle-free light source via random Raman lasing,” J. Mod. Opt. **63**, pp. 46–49 (2016).

[123] B. H. Hokr, J. N. Bixler, G. D. Noojin, R. J. Thomas, B. A. Rockwell, V. V. Yakovlev, and M. O. Scully, “Single-shot stand-off chemical identification of powders using random Raman lasing,” Proc. Natl. Acad. Sci. **111**, pp. 12320–12324 (2014).

[124] J. Briers, G. Richards, and X. He, “Capillary blood flow monitoring using laser speckle contrast analysis (LASCA),” J. Biomed. Opt. **4**, pp. 164–175 (1999).

[125] G. Richards, and J. D. Briers, “Capillary-blood-flow monitoring using laser speckle contrast analysis (LASCA): improving the dynamic range,” In Proc. SPIE 2981, Coherence Domain Opt. Methods Biomed. Sci. Clin. Appl. 160–171 (SPIE, San Jose, CA, USA, 1997).

[126] B. H. Hokr, J. N. Bixler, and V. V. Yakovlev, “Higher order processes in random Raman lasing,” Appl. Phys. A **117**, pp. 681–685 (2014).

[127] B. Redding, M. A. Choma, and H. Cao, “Speckle-free laser imaging using random laser illumination,” Nat. Photonics **6**, pp. 355–359 (2012).

[128] A. J. S. Mcgonigle, A. J. Andrews, G. P. Hogan, D. W. Coutts, and C. E. Webb, “A compact frequency-doubled 10-kHz PRF copper-vapour- laser-pumped dye laser,” Appl. Phys. B **76**, pp. 307–311 (2003).